Optimization of Tunable Silicon Compatible Microring Filters

by

Reja Amatya

Submitted to the Department of Electrical Engineering and Computer Science

in Partial Fulfillment of the Requirements for the Degree of

Master of Science in Electrical Engineering and Computer Science
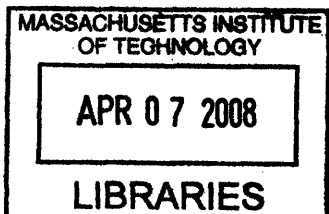
at the Massachusetts Institute of Technology

February 2008

Author_____
Department of Electrical Engineering and Computer Science
Feb 1, 2008

Certified by_____
Rajeev J. Ram
Professor of Electrical Engineering
Thesis Supervisor

Accepted by_____
Terry P. Orlando
Professor of Electrical Engineering
Chairman, Department Committee on Graduate Theses

1

Optimization of Tunable Silicon Compatible Microring Filters

by

Reja Amatya

Submitted to the

Department of Electrical Engineering and Computer Science on

February 1, 2008

in Partial Fulfillment of the Requirements for the Degree of

Master of Science in Electrical Engineering and Computer Science

ABSTRACT

Microring resonators can be used as pass-band filters for wavelength division demultiplexing in electronic-photonic integrated circuits for applications such as analog-to-digital converters (ADCs). For high quality signal transmission, the resonant frequency of the filter has to be held at certain value to allow minimum timing errors in the sampling of the signal. Thermal tuning is used to compensate for any fabrication errors or environmental temperature fluctuations that might lead to shift in the resonant frequency. With the optimized heater design and the proper closed feedback temperature control circuit, the rings have very efficient on-chip thermal control to maintain the resonant frequency within 280 MHz.

Thesis Supervisor: Rajeev J. Ram
Title: Associate Director, Research Laboratory of Electronics (RLE), MIT

ACKNOWLEDGEMENTS

This thesis would not have been possible without the guidance of my research advisor Prof. Rajeev Ram. I would like to thank him for giving me this opportunity to work and be a part of an amazing research group. I was highly inspired by his research style that pushes for understanding the theoretical aspects and limitations of a system while backing it up with good experimental results; the combination of theory and experiment made this research a complete stand-alone work by itself.

I would like to thank all the members of POE that helped me in making a smooth transition to a new life as a graduate student in the new environment at MIT. I thank Peter Mayer for helping me during my early days in the lab and for his patience to answer my questions. I learned a lot from observing his experimental styles. His comments and discussions were always a valuable input to the research, and also thanks for introducing me to the "martini from hell". I would like to take this opportunity to thank Tom Liptay for his helpful insights and suggestions for the research and for being so easily approachable, Harry Lee for being the go-to guy in the lab for all kinds of technical questions and fix-ups. Also, would like to thank Kevin Lee for his helpful advices on experiments, for sharing the equipments and his useful tips on MATLAB. I am thankful to Tauhid Zaman for letting me take over his experimental setup, computer station and showing me how to work my way around the dark in the other lab, and also to Xiaoyun Guo for her helpful advices. Having Jason Orcutt working on the same project of EPIC was very useful for good discussions and bouncing ideas around. I thank him for taking time to explain new technical jargons that came up during such discussions and I am always thankful for his experimental expertise and helpful hints for doing experiments accurately. I would like to thank Parthiban Santhanam for having patience with me during the last month of my thesis work when I was doing the experiments and taking over most of the electrical equipments in the lab. There are some non-POE members at MIT that have helped during this research with their technical advices and I would like to acknowledge them: Prof. Franz Kaertner, Charles Holzwarth, Milos Popvic, Fuwan Gan, Peter Rakich and Anatoly Khilo.

Outside of the MIT community, I would like to thank my friends and family for supporting me, particularly my mom for always being there. I would like to thank my friend and room mate,

Namrata for taking care of me when needed and for being my social connection to the world outside of MIT. There is one special person that I need to thank for being supportive and for encouraging me to do good work all the way through. I am sure I will get many chances to thank him over the course of time that lies ahead.

One man in my family who would have probably read this thesis even though he did not have physics background was my grandfather. With his untimely death, that will not be possible. I dedicate this work to him. I love you Baa.

CONTENTS:

LIST OF FIGURES:

LIST OF TABLES:

SYMBOLS

f_{sample}	Sampling frequency
N	Number of bits
V_{rms}	Root mean square voltage
P_{diss}	Dissipated power
V_{FS}	Full scale voltage
R_{eff}	Thermal noise resistance
f_T	Cut-off frequency of the comparator
τ_a	rms aperture jitter
T	Temperature
k	Boltzmann's constant
I	Current
R	Resistance
n	Refractive index
n_{eff}	Effective refractive index
λ	Wavelength
r	Radius
n_{group}	Group refractive index
t	Transmission coefficient
γ	Absorption coefficient (waveguide loss)
κ	Coupling coefficient
Γ	Transmission factor
φ	Phase shift
c	Speed of light
L	Circumference of the ring
E_g	Bandgap energy
Q	Heat flux
C	Heat capacity
ξ	Thermal conductivity
h	Heat transfer coefficient
A	Area
ρ	Resistivity
d_s	Thickness of the heater
σ	Electrical conductivity
Z_T	Thermal impedance
α	Temperature coefficient
D	Diffusivity
$\mathfrak{R}$	Reflectivity
Ψ	Thermoreflectance coefficient

CHAPTER 1
INTRODUCTION

1.1 Overview:

Since the fabrication and demonstration of the first laser in the late 50's, the field of optics has seen many marvelous inventions such as optical amplifiers, resonators, modulators, low loss waveguides and couplers, photodetectors and optical fibers. In the last 20 years, the merger between electronics and optics has been a field of great interest for researchers all over the world. Many scientists had published their visions and ideas for silicon based optical components for a "photonic circuit" long before the real fabrication ideas were developed [1-3]. Major applications of electrical and optical integrated circuits are for long haul communications. One of the challenges faced today in high speed electronic circuitry is electronic jitter, which limits the performance of the high speed communication tools. The idea behind an optical integrated circuit is to use the optical components to transmit data as light rather than transporting an electrical signal for communication. Limitations due to noise are more severe in electrical signals than optical signals, which are explained in detail below. Two of the systems of interest in this work are an electro-optical circuit for an analog-to-digital converter (ADC) and optical interconnects for a high speed supercomputer. The main focus of the thesis will be on enhancing the performance of an ADC using photonics. The system background describes an electrical ADC and its limitations due to various noise sources. The alternative to an electrical ADC using photonics is presented in Section 1.3.

1.2 System Background:

Long distance communication with pure analog signals is not feasible due to the degradation by noise along the route. Advances in digital signal processing have enabled long haul communications with good signal recovery at the receiver end. The ADC is a critical component for most of today's technologies, namely in communication, instrumentation, signal processing system, medical imaging, and radar system [4]. There are two main functions performed by an ADC on a signal: sample and hold for a specified time, and quantize the held voltage into number

of levels. The sampling rate (f_{sample}) and the resolution (i.e. number of levels or number of bits - N) are the most fundamental parameters of an ADC. Apart from the sampling rate and the number of bits, signal-to-noise ratio (SNR) and the power efficiency figure-of-merit (F) are also important parameters. As the name suggest, SNR gives the quality of the signal with respect to various noises in the system, and is defined as the ratio of the root-mean-square signal amplitude (V_{rms}) to the square root of the integral of the noise power spectrum over the frequency range of interest [4]. In physical ADC devices, the number of bits is always lower than the stated number of bits (N). In an idealized ADC, the only source of the noise is quantization error, which is due to the smallest quantization step size represented by the least significant bit (LSB). The number of bits (N) is related to the signal-to-quantization-noise-ratio (SQNR) by [4].

$$SQNR = 6.02N + 1.763[dB] \tag{1.1}$$

The overall effective resolution includes noises other than quantization noise and is called the effective number of bits (ENOBs). Other types of noises namely thermal, aperture, and comparator ambiguity, degrade the overall performance of the system. In practice, it has been found that the degradation from an idealized resolution to the ENOB is about 1.5 bits for practical ADCs [4]. The ENOB for an ADC is related to the SNR by [4]:

$$ENOB = SNRbit = \frac{(SNR(dB) - 1.763)}{6.02} \tag{1.2}$$

The energy figure-of-merit (F) includes electrical power dissipation (P_{diss}) of the system and represents the total energy required per bit of data conversion.

$$F = \frac{P_{diss}}{2^{SNRbit} f_{sample}} \tag{1.3}$$

For an electronic ADC, the latest record F value is 65 fJ per conversion step with the sampling rate of 50 Mega samples per second (MSPS) and 9 bits [5].

Growth in transistor technology in terms of speed and performance till the last decade had enabled electronic ADCs to function well for various applications. However, a bottleneck is approaching with the electronic ADCs in terms of achieving high sampling rate and relatively high ENOBs. The growth rate has slowed down to 1.9 ENOB/decade with the highest achieved sampling performance of 20 GSPS at 6.5 ENOBs [6]. With power dissipation of 1.1 W, the sampling rate of 10 MSPS and the ENOB of 13 has been achieved [4]. Comparatively higher resolution of 7 ENOBs is only possible with the sampling rate of 5 GSPS or less [4]. 11.8 bits resolution has been shown with the sampling rate of 0.125 GSPS [4]. For low signal frequency, SNR is constant. The noise increases with frequency, thus, the SNR goes down as the signal

frequency increases. Table 1-1 summarizes some of the electronic ADCs with the highest sampling rate, ENOBs and the lowest power dissipation.

	Sampling rate (GSPS)	ENOB	Power dissipation (mW)	FOM * (pJ/conversion)	Ref.	Year
IMEC	0.05	7.75	0.7	0.065	[5]	2007
Agilent	20	4.6	9,000	18	[6]	2003
Maxim	1.5	7.5	5,300	19.5	[7]	2002
†e2V (EV8AQ160)	5	7.1	3,900	5.68	[8]	2007
Texas Instrument	0.125	11.8	420	0.95	[9]	2007
†National Semiconductor	2	7.2	1,900	4.3	[10]	2007
Rockwell	2	7	5,300	20	[11]	1995
Nordic Semiconductor	0.110	10.4	97	0.65	[12]	2005
UCLA	2	6	310	2.4	[13]	2005

Table 1-1: Summary of the best electrical ADC.

(* calculated using equation 1.3, † ADCs with ENOBs >7 and $f_{sample} \geq$ 2GHz)

SNR is the dynamic measure of the ADC performance for high speed applications. The limitation of achieving high resolution and large sampling rate for an ADC is due to the electronic jitter. Aside from quantization noise, other important noise factors in an ADC are thermal, aperture and comparator ambiguity [4]. Figure 1-1 shows the dependences of ENOBs and sampling rate on different kinds of noises. Aperture jitter is due to the uncertainty in the sampling instant, i.e. sample to sample variation in instant of time at which sampling occurs. Within the commercially available electrical ADCs, there is a trend seen according to which, between 2 MSPS to 4 GSPS, the resolution falls off 1 bit for doubling the sampling rate and the main cause is the aperture jitter [4]. Two main causes for the sampling time error are the signal source, which could be the phase noise of the input or clock signal, and the timing uncertainty of the clock buffers. Due to the timing error in the built-in Phase-Locked Loop (PLL) that generates, stabilizes and distributes the digital clock for sampling, ADCs do not sample at precisely equal time-intervals. A state-of-the-art microwave source provides clock signals with timing jitter of about 10 fs; however, the clock buffers degrade the overall jitter performance [14]. At high sampling rates, the speed of electronic components also become one of the limiting factors. This is mainly due to comparator ambiguity which is related to the ability of a comparator to make an unambiguous decision regarding the

relative amplitude of the input voltage. The finite speed with which the transistors in the comparators are able to respond to a small voltage change is the reason for this limitation. In an ADC, all the noise factors ultimately affect the SNR bit value [4].

$$SNRBit_{Thermal} = \log_2\left(\frac{V^2_{FS}}{6kTR_{eff}f_{sample}}\right)^{1/2} - 1$$

$$SNRBit_{Aperture} = \log_2\left(\frac{2}{\sqrt{3}\pi f_{sample}\tau_a}\right)^{1/2} - 1 \tag{1.4}$$

$$SNRBit_{Ambiguity} = \left(\frac{\pi f_T}{6.92 f_{sample}}\right)^{1/2} - 1$$

The variables in the above expressions are: V_{FS} is the full-scale voltage of the analog input signal, R_{eff} is the equivalent thermal noise resistance, τ_a is the rms aperture jitter, and f_T is the cutoff frequency of the comparator frequency response. As shown in the plot below, the aperture jitter limits the SNR bit number at high sampling rates. For the sampling rate as high as 20 MSPS, the resolution is limited by the thermal noise. As the sampling rate goes higher, the resolution goes down. Constants used for the plot generation are: R_{eff} = 2,000 Ω, V_{FS} = 1V, T = 300 K, f_T = 50GHz and τ_a = 0.5ps [4].
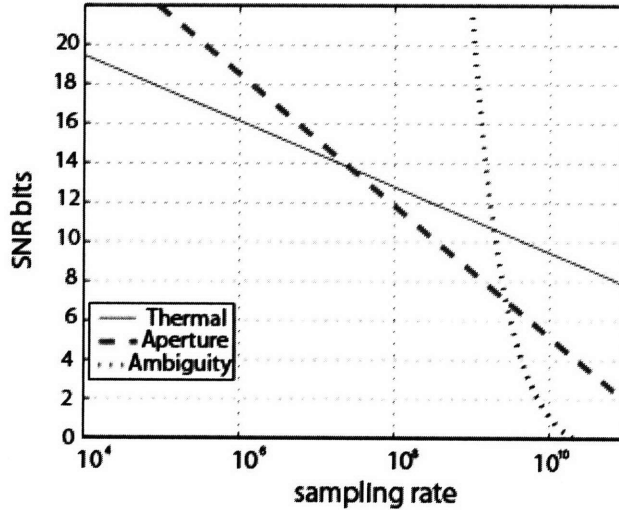
Figure 1-1: Various noise factors limiting the performance of an electronic ADC.

There are various ADC architectures for sampling and hold, and quantizing the signal. Three of the most popular architectures are briefly described below [14-16]:

1. **Flash**: The most common architecture is parallel Flash where 2^N-1 comparators are used for quantization. The sampling rate for the ADC is equal to the Nyquist rate of the analog signal. The comparator bank is connected to a logic circuit that generates codes for the input voltage signal. This is good for high resolution applications. Some of the limitations for the system are the exponential increase in the number of comparators with increased N, large integrated circuits, high power dissipation and difficulty to match components in the parallel comparator channels. Also, increasing the input capacitance reduces the analog input bandwidth.

2. **Pipeline**: Dual step quantization is involved in this architecture. A coarse analog to digital conversion is the first step. In the second step, the difference to the input signal is determined with a digital to analog converter (DAC). The difference is then converted, and the results are combined in a last step. This type of ADC is fast, has a high resolution and only requires a small die size.

3. **$\Delta\Sigma$ modulation**: In this architecture, the signal is over-sampled (i.e. f_{sample} > Nyquist frequency) and the desired signal band is filtered. The quantization is done using a flash ADC after the filter. The resulting signal and the error due to flash is fed back and subtracted from the input of the filter. The negative feedback reduces the error such that it does not appear on the desired signal frequency. An over sampling ADC trades sampling bandwidth for improved amplitude resolution.

Apart from the basic ADC architectures as described above, one way to achieve high sampling rate is time interleaved parallel structure. The sampled signal is interleaved to a channel architecture providing sequential samples to each channel. If M interleaved channels are used, each channel is required to operate at f_{sample}/M, reducing the conversion rate of each individual ADC at the receiver end as shown in Figure 1-2. The bandwidth and the sampling rate for an ADC can be increased by time interleaving the quantized samples from a parallel array of slow converters. This application achieves higher sampling rate, and less power dissipation, without sacrificing SNR bit value. The bandwidth can be increased easily by increasing the components in the parallel array. As a rule of thumb, operating M ADCs in parallel increases the sampling rate by a factor of M. The electronic ADC for conversion in this case can have less effective data rate as the signal comes to the receiver every M^{th} time slot. The major source of error in this architecture is converter matching error, i.e. the output of each converter with low jitter must have the sampled signal in its correct time slot.
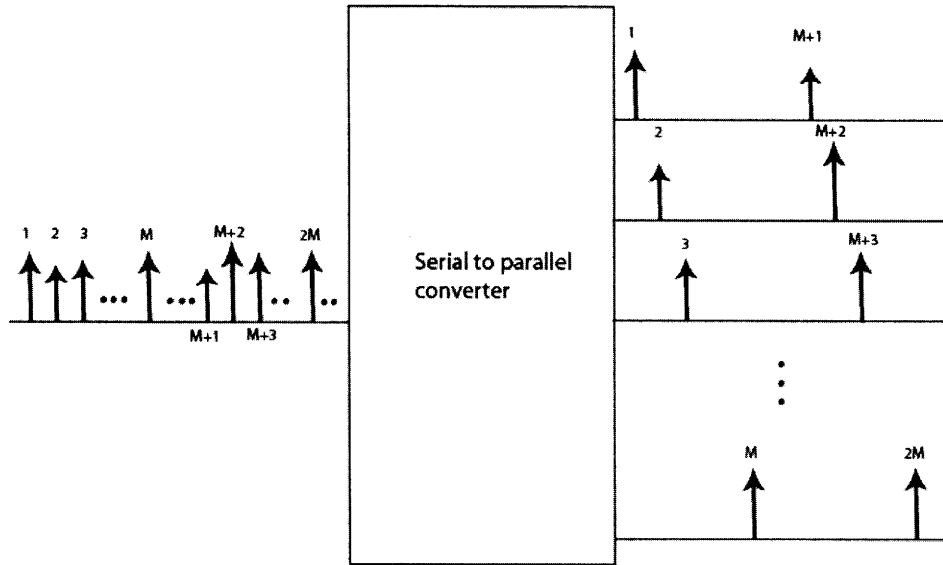
Figure 1-2: Time-interleaving architecture based on temporal demultiplexing.

Some of the other important terminologies for characterizing an ADC are described here. Effective resolution bandwidth (ERBW) is the value of signal frequency at which the SNR decreases to 3 dB below low-frequency value [4]. For most ADCs, ERBW must be greater than the Nyquist rate, which is half of the sampling rate ($\sim f_{sample}/2$). Spur-free-dynamic range (SFDR) is the ratio of single-tone signal amplitude, i.e. the rms fundamental signal, to the largest nonlinear distortion component or the largest spurious noise with the spectrum of interest [4]. To ensure large SFDR in an interleaved system: a) the sampling time of interleaved ADCs must be uniform, b) the converter-to-converter gain and the offsets must be precisely matched, and c) the crosstalk between ADCs must be minimal [14].

The limitation of an electronic ADC to achieve high resolution and large sampling rate at the same time is evident, due to all the noises involved. There is a need for other approaches to enhance the performance of an ADC, and that is where photonics can help.

1.3   System Driver:

As mentioned at the beginning of the system background, the main motivation for this work is the integration of electronics and optical components for an ADC, and optical interconnects for high performance supercomputers. An optically enhanced ADC is the main system of interest which is

described in this section. A system level description is also given for the optical interconnects for a microprocessor chip.

One of the key requirements for the development of these photonic systems is that all the optical devices have to be CMOS compatible. Silicon has been the semiconductor substrate of choice for the electronic industry as it has significant advantages over other semiconducting materials [17]. If optics can be developed in a silicon platform, we can take advantage of the existing fabrications technologies and make extremely small optical devices with significant functionalities. The silicon based material system including silicon (Si), silicon nitride (SiN), and silicon dioxide (SiO_2) is chosen for the fabrication of most of the optical devices for the system.

1.3.1 Electronic and Photonic Integrated Circuit (EPIC):

Research is being done on utilizing photonic devices for better performance of an ADC. One of the ways to get around the limitation of the electronic jitter is to replace the clock source that causes it. Optically enhanced ADCs can help to increase the sampling rate without sacrificing the effective bit number, as the aperture jitter for an optical clock source is fundamentally lower than the electronic counterpart. Precise and high repetition rate (>10 GHz) mode-locked lasers have low timing jitter (<20 fs pulse to pulse) compared to a PLL (~1 ps) [4]. The first ADC utilizing this photonic enhancement was developed in 1984 with 1 GSPS and 4 ENOBs [18]. In GSPS range, the electronic sampling jitter is limited to ~ 1 ps [14], which give the maximum of 8 bits resolution. Optical sampling jitter can be two orders of magnitude smaller and give more than 12 bits resolution for 1 GSPS [14].

Photonics can be used at various stages in an ADC: 1) photonic assisted ADC, 2) photonic sampling and electronic quantization, 3) electronic sampling and photonic quantization, and 4) all optical ADC. The detail review of all the types of systems is given in ref. [18]. Table 1-2 shows some of the recent results for the photonic enhanced ADCs in research. With the current state-of-the-art electronic ADCs, large performance enhancement can be achieved for the sampling rate and the ENOBs by using photonics for sampling and making use of the electronics for quantization. Electronic Photonic Integrated Circuit (EPIC) is based on Gigahertz High-resolution Optical Sampling Technique (GHOST) and electronic quantization for an ADC, with the system specifications of the sampling rate of 40 GSPS and the ENOBs of 7. The goal of EPIC is the integration of optical components in the silicon platform for optical sampling for an ADC.

23

	Material system	Sampling rate (GSPS)	ENOB	Power dissipation (mW)
Jalali et. al. [19]	LiNbO$_3$ (modulator)	12	5	
Esman et. al. [20]	LiNbO$_3$ (modulator)	0.4	6	
Juodawlkis et. al. [14]	LiNbO$_3$/InGaAs/InP	0.505	9.8	
Jalali et. al. [21] (*digitizer)		10,000	4.5	
Jalali et. al. [22]	LiNbO$_3$ (modulator)	130	7	
Miller et. al. [23]	GaAs	0.16	3.5	70
EPIC (proposed system)	Silicon based (CMOS compatible)	40	7	

Table 1-2: Summary of photonic enhanced ADC.

The 'photonic circuit' utilizes the low jitter properties of a mode-locked laser to develop high speed ADC beyond the bottleneck set by electronic jitter, and to achieve system performance better than today's technology in terms of sampling speed and resolution. The total aperture jitter that the system can tolerate to support the required sampling rate and ENOBs is less than 35 fs given by:

$$\tau_{jitter} = \frac{2^{-SNRbit}}{\sqrt{3}\pi f_{sample}}$$ (1.5)

The technique used in EPIC for the analog-to-digital conversion is time-interleaved optical sampling. The time interleaved architecture makes it possible to achieve the desired sampling rate of 40 GSPS with relatively low speed electrical ADCs at the receiver end behind the photodetectors. Wavelength-division (de)multiplexing (WDM) is used for sampling in the time interleaved architecture which assures high data density. In a WDM architecture, the optical signal from a mode-locked laser is chirped and modulated with an RF signal. The modulated optical signal is then filtered through a parallel array of tunable filters. An alternative to WDM is time-division demultiplexing. In time-division demultiplexing the optical signal is not chirped but the electrical signal is blanketed over the optical pulsed signal i.e. the amplitude of the pulsed light carries the electrical information. However, time-division demultiplexing requires accurate optical switches with synchronized time between all switches. The wavelength-division demultiplexing is chosen to avoid the need of accurate clocks for optical switches, and also it has been shown that the insertion loss is less for the wavelength-demultiplexing devices such as

tunable filters than optical switches [18]. Using wavelength-division demultiplexing, the sampled signal is sent to parallel photodetectors and electrical circuit for quantization. The schematic for EPIC is shown in Figure 1-3. The main optical components within EPIC system are mode-locked laser, modulator, tunable filters and photodetectors.
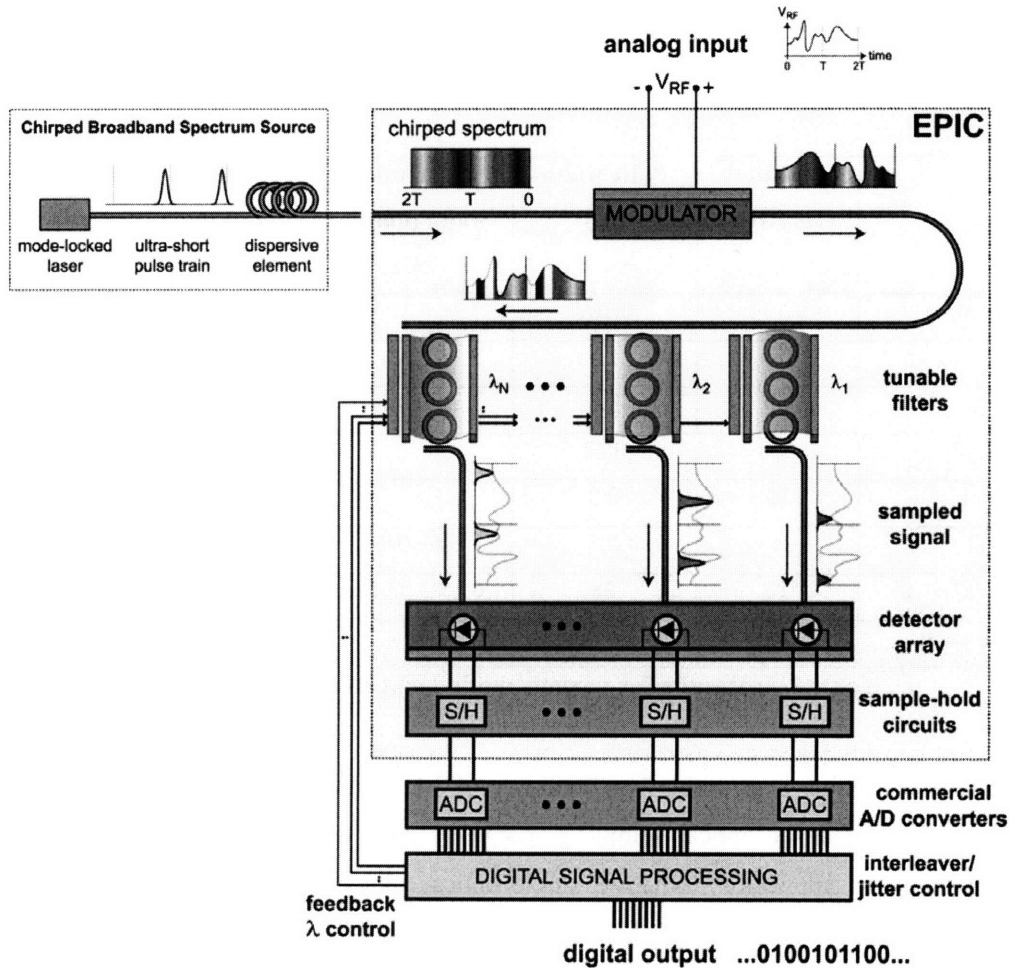
Figure 1-3: Schematic for EPIC. Figure courtesy: Milos Popovic

For various electronic and optical devices, one of the specifications that need to be maintained through out the system is the electrical SNR (~ 44 dB) or the equivalent ENOBs (~ 7). From Table 1-1, it is apparent that the electronic ADC with 7 ENOBs has the sampling rate limited to 2-5 GHz. For low power usage and better figure-of-merit, the ADC with sampling rate of 2 GHz is preferred to be used as the quantizer in the time-interleaved system. Once the sampling rate of the quantizer is known to be 2 GHz; for 40 GSPS data rate, we need 20 tunable filters for WDM. The repetition rate of the mode-locked laser is also determined by the quantizer sampling rate at 2 GHz.

An ultra short pulse train, with low jitter (<20 fs), is needed from a mode-locked laser which can be used as the source for the optical signal. The repetition rate and the spectral width of the pulse from a mode-locked laser define many of the device specifications in the system, namely for the tunable filter, which is discussed at the end of this section. Some of the research data for a mode-locked laser (@ 1550nm) are summarized in Table 1-3.

	Repetition rate (GHz)	Pulse width (ps)	Spectral width (nm) / ~THz	Timing jitter (fs)	Optical Power (mW)	Ref.
Chen et. al.	0.194	0.167		18	450	[24]
Gong et. al.	300	1.4			120	[25]
Ng et. al.	10	3.6	6 / 0.75			[26]
Gong et. al.	660	0.42			1200	[27]
Tien et. al.	10	0.8				[28]
Yu. Et. al.	1	0.5	5.6 / 0.7		400	[29]
Malowicki et. al.	10	28	0.15 / 0.018	21	200	[30]
Schlager et. al.	0.75	6		14.4	500	[31]

Table 1-3: Results for various mode-locked lasers at 1550nm.

An erbium-doped fiber laser with a repetition rate of 2 GHz and the spectral width of 22 nm (~ 2.8 THz) is utilized for optical sampling. Large spectral width of <2 THz is desired for telecommunication application, where a single optical source can cover most of the C-band (1530nm – 1569nm). The signal is chirped using a dispersive element such as a spool of fiber. The optical chirp (= pulse period/spectral width) obtained for the pulse is 22 ps/nm. For the desired spectral width of 2 THz, a linear optical chirp can be assumed. In an optical fiber, the linear chirp can be assured by optimizing the refractive index profile [32]. The RF signal is mapped onto the chirped optical pulse using a silicon based 10 GHz Mach Zehnder modulator. The modulator determines the analog bandwidth for the RF signal that is sampled by the optical signal. The modulated signal is sampled using tunable filters at 2 GHz. As mentioned earlier, the sampling rate i.e. the data density can be increased significantly by using the filters in an array for WDM. For WDM, various demultiplexers can be used, such as microring resonators, array waveguide gratings (AWGs), mach-zehnder (MZ) interferometer, or chirped grating. In most of these demultiplexing devices, lower-index contrast material systems result in large area due to limitation of the bend radius, and device parameters such as the number of wavelength channels.

Using a high-index-contrast (HIC) material system, the bend radius of a few microns can be achieved. However, in the grating devices especially an AWG, the miniaturization of the demultiplexers and their performance are inversely related [33]. One of the pronounced losses in an AWG in a high-index-contrast material system such as Si-SiO$_2$ is the scattering loss at the gaps between the array waveguides (0.3-0.5 dB/cm) [33]. To reduce the scattering loss, lower-index material is used for the coupler slab, which increases the overall device area. Crosstalk between waveguides also increases when the number of channels is increased and the overall area is kept fixed. The transfer function of the MZ filter is usually not narrow enough for WDM applications [34]. Thus, cascaded MZ filters are used as demultiplexers. The advantages and disadvantages of various kinds of filters are summarized in Table 1-4.
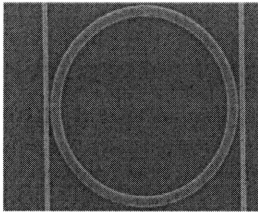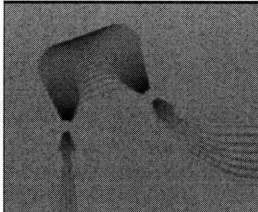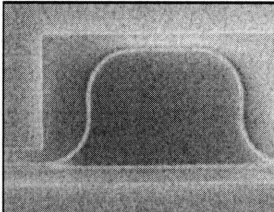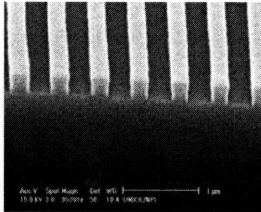
Microring resonator	Array waveguide grating (AWG)	(Cascaded) Mach-Zehnder Interferometer	Chirped grating
Advantages: • Area (20 channel)~ 0.05mm^2 ($\Delta n \sim 0.75$) • Low drop loss	**Advantages:** • Large tuning range (40nm)	**Advantages:** • Relatively fast switching speed (50ns) • Low production cost	**Advantages:** • Easier fabrication (no bends)
Disadvantages: • Slow thermo-optic tuning speed (ms)	**Disadvantages:** • Area (20 channel) ~ 0.25mm^2 ($\Delta n \sim 0.75$) • slow thermo-optic tuning (ms)	**Disadvantages:** • Low finesse (i.e. larger loss) due to inherent cosine shape in the transfer function • Small tuning range (< 5nm)	**Disadvantages:** • Slow tuning speed (ms) • Small tuning range (<10nm)

Table 1-4: Summary of filtering technologies.

Here, Silicon-rich-SiN microring resonators are used as tunable filters for optical sampling. One of the primary reasons for using SiN instead of Si for the ring resonator is due to the higher precision required to stabilize the more thermally sensitive silicon rings. Temperature dependence

to the resonant wavelength is discussed in detail in Chapter 3. The working principle of a ring resonator and the device specifications are explained in Chapter 2. The signal at the drop port of the filter is the time-interleaved optically sampled signal, with each filter operating at the repetition rate of the mode-locked laser (i.e. 2 GHz). The total sampling rate of the system is the clock rate of the mode-locked laser times the number of filter channels for WDM. With 20 channels in a single filter bank, and an optical source of 2 GHz repetition rate, the total sampling rate of 40 GSPS (= 20 * 2 GHz) is obtained. 20 channels have to fit within the spectral width of the pulse of the optical source (i.e. ~ 2 THz, linear chirp region). With a practical full-width-half-maximum (FWHM) of 25 GHz achievable for the filter, the channel spacing is 80 GHz which would allow 20 filters to fit within the linear chirp region of 2 THz (~ 80 GHz * 20 + 25 GHz *20). The FWHM and the channel spacing are also within the standard ITU grid policy of 1:3 ratio. Higher-order filter gives sharper roll-off to diminish the cross-talk between adjacent channels [35]. Thus, second-order filters are used for demultiplexing. The cross-talk between the adjacent channels is an important factor, as it determines the signal-to-noise ratio. The relation between optical and electrical SNR is given by [36]:

$$dB_{(electrical)} = 10\log\left(\frac{R*I^2_{out}}{R*I^2_{in}}\right) = 2*10\log\left(\frac{I_{out}}{I_{in}}\right) = 2*dB_{(optical)} \qquad (1.6)$$

In order to maintain -44 dB electrical SNR, the optical signal-to-noise has to be at least -22 dB. There have been many models to determine the penalty in dB, in the electrical domain due to channel cross-talk [37-40]. Theoretical power penalties for various numbers of interfering components of cross-talk in an optical network are recreated from ref. [38]. According to Figure 1-4, -30 dB cross-talk gives about <2 dB degradation in the electrical SNR.
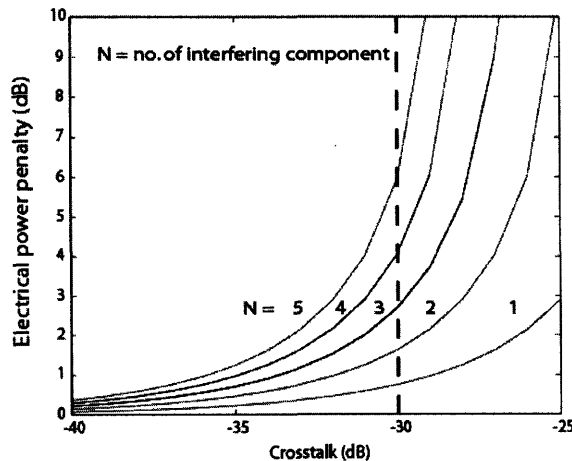
Figure 1-4: Optical crosstalk vs. electrical power penalty.

The total amount of power required for tuning of the filters is an important parameter. For EPIC, the filters need to be held at a steady temperature and no dynamic tuning is required. Thus, instead of a large tuning rage, low tuning power is important. Commercial electronic ADCs operate mostly from -40 to 85°C. If we take the photonic ADC with similar operating temperature, the maximum temperature fluctuation is that of 125°C. However, in real conditions we do not anticipate such high temperature fluctuations for the tunable filters. The ADC can be held with proper TEC modules and temperature controllers to keep the operating temperature within the nominal room temperature. However, the filters are highly sensitive to temperature and any small fluctuation can shift the frequency. Thus, each filter is allocated a modest 1 mW of power for tuning with temperature fluctuation range of ~ 5°C. This corresponds to the tuning power of 60 μW/GHz/channel.

Silicon-Germanium (SiGe) photodetector can be used at the receiver end before quantization. As mentioned earlier, an electronic ADC with 7 ENOBs and sampling rate of <2 GHz can be used as the quantizer. Summary of the system target and the parameters for the tunable filters is given in Table 1-5.

ADC Goal:	ENOB = 7 (SNR = 44dB)	Sampling rate = 40GSPS	Jitter = 35fs

	SNR (dB$_{elec.}$)	cross-talk (dB)	3dB bandwidth (GHz)	Channel spacing (GHz)	Tuning power (μW/GHz/channel)
Tunable filter	44	<-30	25	80	60

Table 1-5: Specification for a tunable filter for EPIC.

Thus, at the system level, better performance can be achieved from the optically sampled ADC using a low jitter femto-second mode-locked laser along with 20 channel filter bank, to ensure the sampling rate of 40 GSPS with the ENOBs of 7. The focus of this thesis will be on the microring resonators used as tunable filters described in detail in later chapters.

1.3.2 Ultraperformance Nanophotonic Intrachip Communications (UNIC):

Another system of interest is the demonstration of optical interconnects for microprocessor chips. Optical interconnects have been studied for many years as a reasonable replacement for the electronic version [41]. The limited bandwidth of the electronic interconnects have hindered the speed of CPUs. By using optics to communicate between different elements of a microprocessor chip with various optical components, the limitation of electrical bandwidth can be eliminated. The figure-of-merit in an interconnect system is in terms of Giga bits per length. In the electrical interconnect system, multilayer wires allow large data transfer. Multilayer lines for optical interconnect are not very feasible from fabrication perspective. One way to meet the interconnect bandwidth density requirement is using wavelength division demultiplexing. The microrings are sufficiently small that they can be incorporated in a microprocessor without consuming too much real estate. For the UNIC project, optical components such as a laser, modulator, filter and photodetector are to be used within a processor chip to transmit data between memory and the core processing unit such as ALU. Figure 1-5 shows a simple schematic for UNIC.
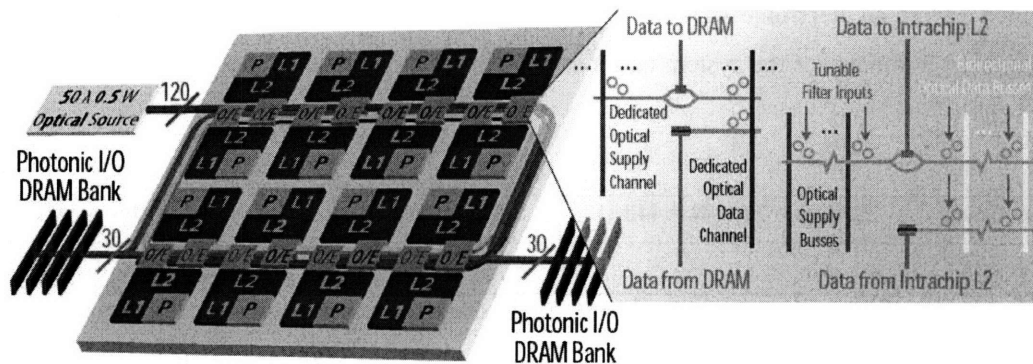
Figure 1-5: Schematic for UNIC. Figure courtesy: Jason Orcutt

Similar to EPIC, the ring resonators will be used as wavelength selective filters. In a microprocessor chip, the operating temperature varies widely (30-50°C) depending on the workload. Thus, larger tuning range is required for this application than that for EPIC, and also the dynamic tuning for the rings have to be considered. Power density is one of the limiting factors in a processor, mainly due to the limitations of the conventional cooling mechanisms such as forced convection or water cooling. The total energy dissipation for the UNIC system has to be less than 500 fJ/bit. This energy constraint requires very efficient thermal tuning of the ring with power consumption of less than 20 μW/GHz. Due to processing constraints, the proposed idea for thermal tuning of the resonator is with the poly-Si heaters fabricated on the same level of the waveguide.

1.4 Thesis Outline:

Ring resonators are one of the building blocks for optical and electrical integrated circuit. The working principle and all the major characteristics of a ring resonator are defined in Chapter 2. For the EPIC system, apart from the jitter due to the mode-locked laser, another place within the optical sampling where jitter can occur is during wavelength-division demultiplexing at the filters. The filters have to be tuned to a precise center frequency. Any deviation from the resonant frequency is seen as the timing jitter for sampling. If we allocate less than 20 fs jitter for the optical source, we can tolerate 15 fs jitter at the tunable filters. Thus, we need to be able to precisely control the resonant frequency of the filter, such that the jitter is within the desired specification. The timing jitter of 15 fs with the chirped pulse of 22 ps/nm corresponds to the stability of the resonant frequency to within 100 MHz. For a SiN based ring resonator, the resonant frequency shifts by 3.55 GHz for every degree rise in temperature. This is verified experimentally for the Si-rich-SiN microring in Chapter 3. To be able to control the resonant frequency of the ring within 100 MHz, the rings have to be thermally stable to within 30 mK of the desired absolute temperature. The thermal tuning is used for postfabrication trimming and for any environmental temperature fluctuations. Other tuning options are also briefly discussed in Chapter 3. Dynamic tuning is not required for the system as the purpose is to stabilize the rings within certain temperature. For EPIC, power efficiency of tuning and wavelength stability is more important metrics than tuning range.

Optimized thin film heaters are fabricated on top of the cladding to locally change the temperature of the resonator. One of the key parameters under consideration for the design of the heaters is the power dissipation required for tuning. Finite-element thermal simulation (FEMLAB) is used to study the temperature profile for the filter along with heaters. The upper cladding of 1.9 μm ensures optical isolation of the resonator from local heaters on top. Simulations done with FEMLAB have shown long heaters with high thermal impedance to be appropriate in order to minimize power dissipation for thermal tuning. Three different heater designs with various resistance and tuning powers are studied and presented in Chapter 4. The total tuning power of 80 μW/GHz is achieved for the second-order filter with tuning up to 2 nm which is sufficient for tuning across the entire channel spacing of 85 GHz.

The details of the thermo-optic effect and the thermal tuning of a ring resonator are discussed in Chapter 3, showing thermal tuning data for the silicon-rich-SiN rings using the on-chip heater. The details of the heat transfer theory and various heater designs are discussed in Chapter 4 along with descriptions of experimental methods used for heater characterization, namely the 3-ω method and thermoreflectance. Chapter 5 discusses the temperature controller circuit used with the heater for precise filter temperature control. A control loop feedback circuit with proportional-integral-derivative (PID) controller is used as the temperature controller and the circuit is modeled using the commercial modeling tool: SPICE to check the stability of the circuit. The experimental results show that the circuit is able to control the temperature of the filters within 80 mK, which assures the resonant frequency stability within 280 MHz. The future work and concluding remarks are presented in Chapter 6.

References:

1. R. A. Soref, "Silicon-Based Optoelectronics", Proceedings of the IEEE, Vol. 81, No. 12, Dec (1993).

2. B. Schuppert, J. Schmidtchen, A. Splett, U. Fischer, T. Zinke, R. Moosburger, K. Petermann, "Integrated Optics in Silicon and SiGe-Heterostructures", Journal of Lightwave Technology, Vol. 14, No. 10, Oct (1996).

3. W. Bogaerts, D. Taillaert, B. Luyssaert, P. Dumon, J. Van Campenhout, P. Bienstman, D. Van Thourhout, R. Baets, V. Wiaux, S. Beckx, "Basic structures for photonic integrated circuits in Silicon-on-insulator", Optical Society of America (2004).

4. R.H. Walden, "Analog-to-Digital Converter Survey and Analysis", IEEE Journal on Selected Areas in Communications, Vol. 17, No.4, pp. 539-550, April (1999).

5. IMEC, Press release, http://www.imec.be/wwwinter/mediacenter/en/ADC_ISSCC2007.shtml, (2007).

6. K. Poulton, R. Neff, B. Setterberg, B. Wuppermann, T. Kopley, R. Jewett, J. Pernillo, C. Tan, A. Montijo, "A 20GS/s 8b ADC with a 1MB Memory in 0.18μm CMOS", ISSCC 2003, session 18, paper 18.1, (2003).

7. K.H. Lundberg, "High-Speed Analog-to-Digital Converter Survey", unpublished material, Oct, (2002).

8. e2v: Sensors, Semiconductors & Electronic Tube Production, datasheet: http://www.e2v.com/module/page-398/datasheet.cfm, (2007).

9. Texas Instrument, datasheet: http://focus.ti.com/docs/prod/folders/print/ads6445.html, (2007).

10. National Semiconductor, datasheet: http://www.national.com/appinfo/adc/ghz_adc.html, (2007).

11. K.R. Nary, R. Nubling, S. Beccue, W.T. Colleran, J. Penney, K. Wang, "An 8-Bit 2 Giga sample per second Analog to digital converter", GaAs IC Symposium, pp 303-306, (1995).

12. T.N. Andersen, B. Hernes, A. Briskemyr, F. Telsto, J. Bjornsen, T.E. Bonnerud, O. Moldsvor, "A Cost-Effective High-Speed 12-bit Pipeline ADC in 0.18-μm Digital CMOS", IEEE Journal of solid-state circuits, Vol. 40, No. 7, July (2005).

13. X. Jiang, M.F. Chang, "A 1-GHz Signal Bandwidth 6-bit CMOS ADC with Power-Efficient Averaging", IEEE Journal of solid-state circuits, Vol. 40, No. 2, Feb (2005).

14. P.W. Juodawlkis, J.C. Twichell, G.E. Betts, J.J. Hargreaves, R.D. Younger, J.L. Wasserman, F.J. O'Donnell, K.G. Ray, R.C. Williamson, "Optically Sampled Analog-to-Digital Converters", IEEE Transactions on Microwave Theory and Techniques, Vol. 49, No. 10, pp. 1840-1853, Oct (2001).

15. E. Stebbins, P. Bradley, "Hypres flash ADC program report", Hypres, Inc., (1993).

16. Website: http://en.wikipedia.org/wiki/Analog-to-digital_converter (2007).

17. D.R. Lim, B.E. Little, K.K Lee, M. Morse, H. Fujimoto. H.A. Haus, L.C. Kimerling, "Micron-sized channel dropping filters using silicon waveguide devices", Proceedings SPIE conference, Vol. 3847, Sept (1999).

18. G.C. Valley, "Photonic analog-to-digital converters", Optics Express, Vol. 15, No. 5, March (2007).

19. F. Coppinger, A.S. Bhushan, B. Jalali, "12 GS/s wavelength division sampling analog-to-digital converter", Electronics Letters, Vol. 36, No.4, Feb (2000).

20. M.Y. Frankel, J.U. Kang, R.D. Esman, "High-performance photonic analog-digital converter", Electronics Letters, Vol. 33, No.25, Dec (1997).

21. J. Chou, O. Boyaz, B. Jalali, "Femtosecond real-time single-shot digitizer," presented at the March 2006 Meeting of the American Physical Society (2006).

22. A.S. Bhushan, P.V. Kelkar, B. Jalali, O. Boyraz. M. Islam, "130-GS/s Photonic Analog-to-Digital Converter with Time Stretch Preprocessor", IEEE Photonics Technology Letters, Vol. 14, No. 5, May (2002).

23. L.Y. Nathawad, R. Urata, B.A. Wooley, D.A.B. Miller, "A 40-GHz-Bandwidth, 4-Bit, Time-Interleaved A/D Converter Using Photoconductive Sampling", IEEE Journal of solid-state circuits, Vol. 38, No. 12, Dec (2003).

24. J. Chen, J.W. Sickler, E.P. Ippen, F.X. Kartner, "High repetition rate, low jitter, low intensity noise, fundamentally mode-locked 167 fs soliton Er-fiber laser", Optics Letters, Vol. 32, No. 11, June (2007).

25. Y. Gong, P. Shum, C. Lu, "Passively mode-locked fiber ring laser with tunable repletion rate output", Optical Engineering Letters, Vol. 44(6), June (2005).

26. W. Ng, L. Luh, D. Persechini, D. Le, Y.M. So, M. Mokhtari, C. Fields, D. Yap, J. Jensen, "Ultra-High Speed Photonic Analog-to-digital Conversion Technologies", Proceedings of SPIE, Vol. 5435, (2004).

27. Y.D. Gong, P. Shum, D.Y. Tang, C. Lu, X. Guo, "660 GHz soliton source based on modulation instability in a short cavity", Optics Express, Vol. 11, No. 20, Oct (2003).

28. M. Tien, W.W. Hsiang, Y. Lai, "Direct generation of a 10 GHz 816 fs pulse train from an erbium-fiber soliton laser with asynchronous phase modulation", Optics Letters, Vol. 30, No. 18, Sept (2005).

29. C.X. Yu, H.A. Haus, E.P. Ippen, "Gigahertz-repetition –rate mode-locked fiber laser for continuum generation", Optics Letters, Vol. 25, No. 19, Oct (2000).

30. J.E. Malowicki, M.L. Fanto, M.J. Hayduk, P.J. Delfyett, "Harmonically Mode-locked Glass Waveguide Laser with 21-fs Timing Jitter", IEEE Photonics Technology Letters, Vol. 17, No. 1, Jan (2005)

31. J.B. Schlager, B.E. Callicoatt, R.P. Mirin, N.A. Sanford, D.J. Jones, J. Ye, "Passively mode-locked glass waveguide laser with 14-fs timing jitter", Optics Letters, Vol. 28, No. 23, Dec (2003).

32. S.P. Survaiya, R.K. Shevgaonkar, "Dispersion Characteristics of an Optical Fiber Having Linear Chirp Refractive Index Profile", Journal of Lightwave Technology, Vol. 17, No. 10, Oct (1999).

33. P. Bienstman, F. Van Laere, D. Taillaert, P. Dumon, W. Bogaerts, K. De Vos, D. Van Thourhout, R. Baets, "High Index-Contrast Silicon-On Insulator Nanophotonics", 2006 International Conference on Transparent Optical Networks, Vol. 2, pp. 124-127, June (2006).

34. D. Sadot, E. Boimovich, "Tunable Optical Filters for Dense WDM Networks", IEEE Communications Magazine, Vol. 36, Issue 12, pp. 50-55, Dec (1998).

35. J.V. Hryniewicz, P.P. Absil, B.E. Little, R.A. Wilson, P.T. Ho, "High Oder Filter Response in Coupled Microring Resonators", IEEE Photonics Technology Letters, Vol. 12, No. 3, March (2000).

36. A.P. Gonzalez-Marcos, "Relation between optical and electrical parameters in photonics systems for first year university student", Proceedings of SPIE, Vol. 5578, pp. 747-755 (2004).

37. L.A. Buckman, L.P. Chen, K.Y. Lau, "Crosstalk Penalty in All-Optical Distributed Switching Networks", IEEE Photonics Technology Letters, Vol. 9, No. 2, Feb (1997).

38. E.L. Goldstein, L. Eskildsen, "Scaling Limitations in Transparent Optical Networks Due to Low-Level Crosstalk", IEEE Photonics Technology Letters, Vol. 7, No. 1, Jan (1995).

39. J.C. Attard, J.E. Mitchell, C.J. Rasmussen, "Performance Analysis of Interferometric Noise Due to Unequally Powered Interferes in Optical Networks", Journal of Lightwave Technology, Vol. 23, No. 4, April (2005).

40. D.J. Blumenthal, P. Granestrand, L. Thylen, "BER Floors due to Heterodyne Coherent Crosstalk in Space Photonic Switches for WDM Networks", IEEE Photonics Technology Letters, Vol. 8, No.2, Feb (1996).

41. Miller, D.A.B., "Rationale and challenges for optical interconnects to electronic chips", Proceedings of the IEEE, Vol. 88, No. 6, pp. 728-49, June (2000).

CHAPTER 2

MICRORING RESONATOR

2.1 Overview:

Microring resonators are used as tunable filters for wavelength-division demultiplexing (WDM) during optical sampling for an ADC. As mentioned in Chapter 1, there are various other devices which can be used as filters in WDM systems, but the microring resonators have the most advantages for the application of photonic ADC. In this chapter, the working principle of a ring resonator is explained with all the characteristics defined that are needed to understand the performance of a filter. Each parameter value for the filter is based upon the system specifications. Previous work in the filter development and its performances are mentioned in the background section.

2.2 Background:

One of the building blocks for an electrical and optical integrated circuit is a microring resonator (Figure 2-1), which has wide functionalities. Optical ring resonators have been widely studied and characterized as passive devices. Various aspects of microrings can be used to make wavelength converters, comb frequency generators, add-drop filters, dispersion compensators, wavelength division multiplexed (WDM) networks, lasers, modulators etc [1-4]. In this work, the microring is being used as an optical tunable filter for wavelength selection.

Input port   Through port

R

Drop port
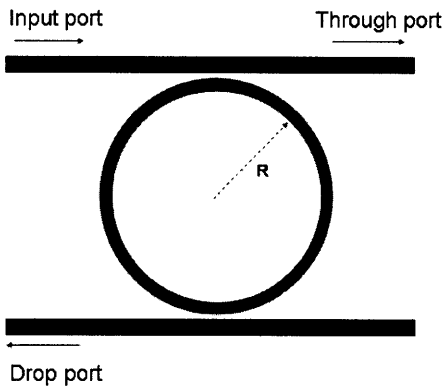
Figure 2-1: First-order ring resonator.

The idea of microring waveguides can be traced back to late 60's from Bell labs, where it was first fabricated and studied for different optical functions [2]. Till the early 80's large size ring resonators were being used for optical demonstrations [5], [6]. It was only in 1997 that B.E. Little [7] successfully analyzed optical coupling from a bus waveguide into a microring resonator (radius $\approx$ 2 µm) using couple mode theory and rigorous numerical finite difference time domain (FDTD) simulation. Most photonic applications require resonators with a large free-spectral range (FSR) and low loss, requiring rings to be fabricated with high-index-contrast (HIC) material, such that there is tight beam confinement. Large FSR is desirable for telecom applications where the C-band (1530-1569) covers approximately 40 nm in the spectrum range. The bending loss decreases exponentially with increasing the index contrast between the core and the cladding as shown in Figure 2-2; recreated using theoretical loss relation from ref. [8]. However, the scattering loss depends on the size of the waveguide and there is an optimum value for which the total loss will be minimum. Scattering loss analysis for micron sized waveguides is discussed in ref. [9]. Si as well as SiN optical waveguides are becoming integral components for optical systems because of the advantages of HIC and compatibility with silicon integrated circuits (IC). Due to the HIC, the rings can be made as small as 5 µm radius with low loss. Thus, more of these compact devices can be integrated in a smaller area. The details on how a ring resonator works are described in the next section.
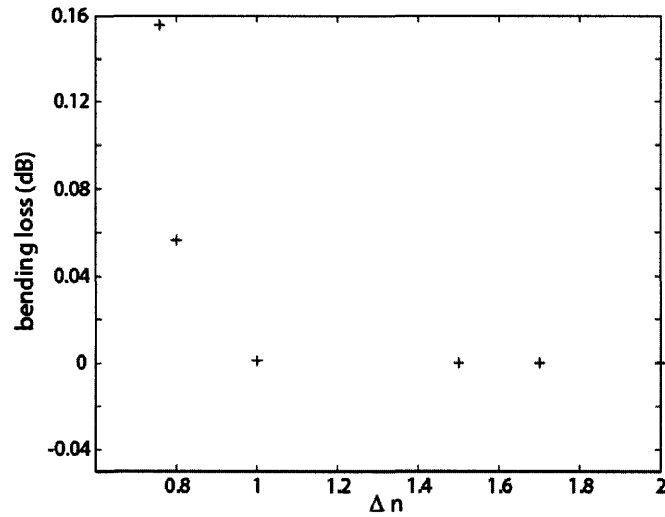
Figure 2-2: Bending loss vs. change in refractive index of core and cladding (Theory Ref. 8).

2.3 How does a ring resonator work?

The concept of a microring waveguide is to confine light of particular wavelength in a circular path of the core. Total internal reflection guides the light from the core-cladding interface and depending on the wavelength of the light; there may be constructive or destructive interference. For a greater confinement of light within these rings, large index contrast between core (n_1) and cladding (n_2) is desired, such that, the bending loss can be greatly minimized. The critical angle for total internal reflection is related to the refractive indices of the core and the cladding:

$$\theta_c = Sin^{-1}\left(\frac{n_2}{n_1}\right)$$ (2.1)

In a HIC system, the critical angle is very small, thus ensuring the reflection of most of the light at the core-cladding interface.

The ring resonators are highly wavelength selective and very useful as optical filters for various wavelength signals. Figure 2-3 shows a ray trace inside a single ring waveguide showing two coupled bus waveguides by its side. "Micro" refers to the size of these rings, whose radius is usually a few microns to ensure large free spectral range (FSR), and is also beneficial for area conservation in chips due to its compact size and possibility of high density integration.
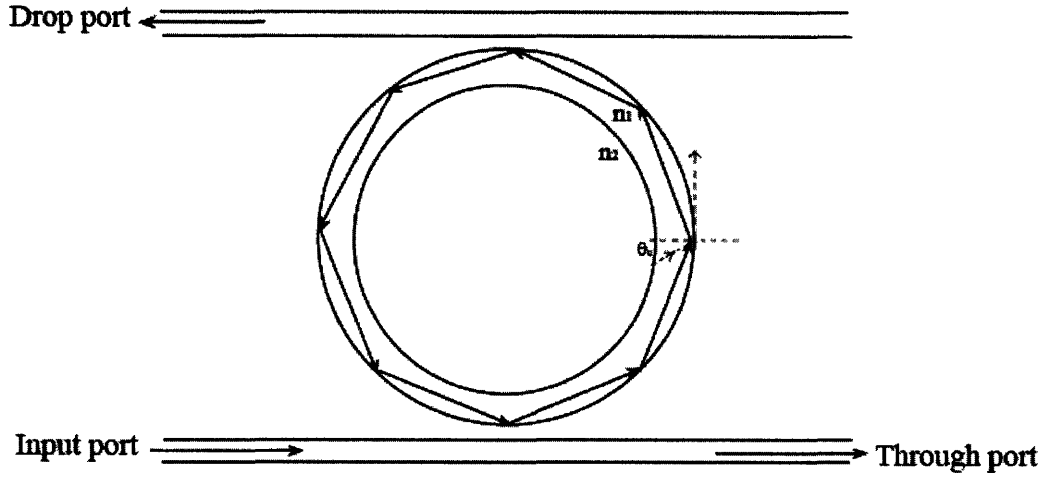
Figure 2-3: Simple ray trace inside a ring waveguide.

The light from the input port will evanescently couple into the ring. If the optical path length of the ring is equal to an integer number of the wavelength, it satisfies the resonance condition and most of the light of the corresponding wavelength is transferred to the ring. The light is then redirected to the drop port at the other side of the ring. The resonant wavelength for a ring depends on the geometry and the effective index (n_{eff}) of the sample. If the wavelength, for example λ_i, and a ring with radius r, satisfies the condition for resonance, such that the optical path length is,

$$2\pi n_{eff} r = \lambda_i N_i \qquad (2.2)$$

the signal couples into the drop port, while rest of the light will pass through the output port [10]. N_i is an integer and represents the resonance order. From equation 2.2, we get the resonant wavelength (λ_o) for a ring, depending on the ring geometry and its effective index.

$$\lambda_o = \frac{2\pi n_{eff} r}{N_i} \qquad (2.3)$$

The free spectral range (FSR) for a resonator is the frequency spacing of the resonance modes.

$$FSR = \frac{\lambda_o^2}{2\pi n_{eff} r} \qquad (2.4)$$

The FSR is inversely proportional to the radius of the ring. Thus, to have high FSR, a small ring is desired. In the EPIC system, the FSR for the ring is determined by the spectral width of the mode-locked laser which is 2.8 THz. Linear optical chirp is assumed for 2 THz, thus, the FSR for the ring is limited to 2 THz. Once the FSR is fixed and the working wavelength is taken to be 1.55 μm (for telecom applications), the radius of the ring is ~10 μm for the SiN material system.

Important parameters in designing a ring filter are ring radius, distance between bus and ring waveguide and refractive index contrast (i.e. material selection for the core and the cladding). The gap between the bus waveguide and the ring determines the coupling between them. The total loss for a resonator depends on the coupling coefficient. In a ring resonator, there can be three conditions: under, over or critical coupling. At critical coupling, the transmission coefficient (t) is equal to the total internal loss (γ) of the ring, and the transmitted power across the bus waveguide is zero (i.e. all the power is transferred to the ring). During critical coupling, there is perfect destructive interference in the through port between the transmitted field and the internal field coupled into the output waveguide. Small changes in the coupling coefficient can change the transmitted power.
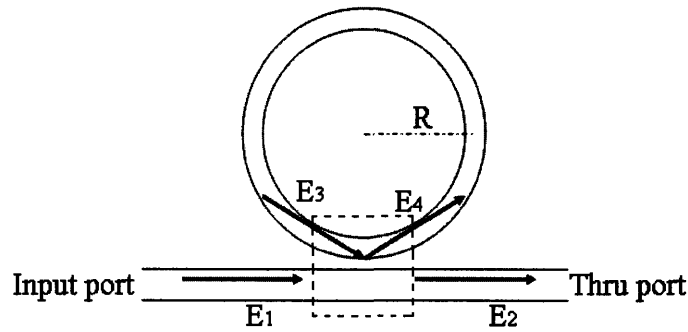
Figure 2-4: Light coupling from bus waveguide to the ring.

The coupling of light (Figure 2-4) into and out of the resonator can be described by the behavior of the directional coupler. Two assumptions are made in the coupler, 1) coupling is limited to the wave traveling in one direction (i.e. no reflection), and 2) there is no loss in the coupler. The amplitudes (E) of the field in the coupling region are related by the transmission coefficient (t) and the coupling constant (κ). The relation is given by [11-13]:

$$E_2 = tE_1 - j\kappa E_3 \tag{2.5}$$

$$E_4 = tE_3 - j\kappa E_1 \tag{2.6}$$

In the matrix representation, the unitary scattering matrix can define the coupled field as,

$$\begin{pmatrix} E_2 \\ E_4 \end{pmatrix} = \begin{pmatrix} t & -j\kappa \\ -j\kappa & t \end{pmatrix}\begin{pmatrix} E_1 \\ E_3 \end{pmatrix} \tag{2.7}$$

The coupling and the transmission coefficients are associated with the medium in-between the ring and the bus waveguide. The total coupling between the bus waveguide and the ring is given by $|\kappa^2|$ and,

$$|t|^2 + |\kappa|^2 = 1 \qquad (2.8)$$

The light that enters the ring will accumulate a round-trip phase shift 'φ', such that $\varphi = kL$. L is the circumference of the ring ($L = 2\pi R$) and k is defined as:

$$k = \frac{2\pi n_{eff}}{\lambda} \qquad (2.9)$$

The output at the through end can also be related to the phase accumulation and an amplitude transmission factor 'Γ' by [15],

$$E_2 = \Gamma \exp(i\varphi)E_4 \qquad (2.10)$$

The amplitude transmission factor (Γ) describes the total loss of the ring which is the sum of material loss, radiation loss due to bending and loss due to wall roughness (for example, $\Gamma = 0.95$ means 95% transmission and 5% loss). The transmission intensity factor at the through port is given by [15]:

$$T = \left|\frac{E_2}{E_1}\right|^2 = \frac{\Gamma^2 - 2t\Gamma\cos\varphi + t^2}{1 - 2t\Gamma\cos\varphi + t^2\Gamma^2} \qquad (2.11)$$

At resonance, the phase accumulated by the signal is the multiple of 2π, $\varphi = m2\pi$, and the light couples into the drop port. The transfer function is:

$$T = \left|\frac{E_2}{E_1}\right|^2 = \frac{(\Gamma - t)^2}{(1 - \Gamma t)^2} \qquad (2.12)$$

Figure 2-5 shows a theoretical plot for the transmission curve for a first-order SiN ring of 10 μm radius. The FSR seen in the spectrum is about 26 nm which is consistent with the calculation using Equation 2.4. As mentioned earlier, at critical coupling, $\Gamma = t$. Thus, at resonance, the total power transmitted will be zero as all the power is transferred into the ring.
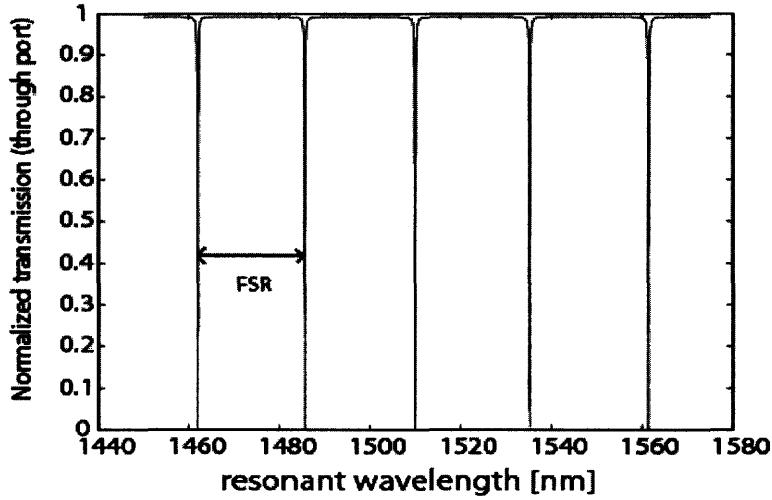
Figure 2-5: Transmission curve showing the FSR of ~ 26 nm.

The same principle of transmission can be applied for higher-order ring system, where the complete transfer matrix can be easily calculated using the individual ring matrices and transfer matrix between the bus and the ring waveguides. As mentioned earlier, higher-order ring system is used to get steeper drop response to reduce the cross-talk between the adjacent resonators. Also for the second-order filter, the direction of drop is same as that of the input and through ports which is useful in WDM applications.
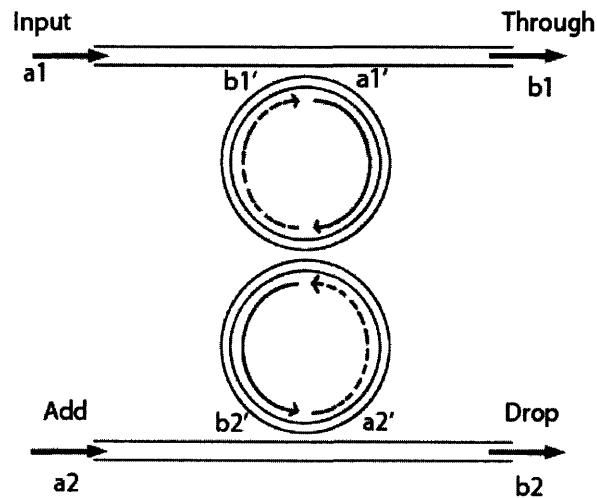
Figure 2-6: Second-order ring resonator.

The transfer matrix connecting the mode amplitudes at the bus waveguide and the first ring is similar to Equation 2.7 [16].

$$b_1 = ta_1 - j\kappa b_1'$$ (2.13)

$$a_1' = -j\kappa a_1 + tb_1'$$ (2.14)

$$b_1' = e^{2x}\left(t'a_1' - j\kappa'a_2'\right)$$ (2.15)

$$b_2' = e^{2x}\left(-j\kappa'a_1' + t'a_2'\right)$$ (2.16)

$$b_2 = ta_2 - j\kappa b_2'$$ (2.17)

$$a_2' = -j\kappa a_2 + tb_2'$$ (2.18)

where, $x = \left(j\omega\dfrac{T_r}{2} - \gamma\dfrac{L}{4}\right)$; γ is the absorption coefficient of the ring material and describes the loss in the ring, T_r is the round-trip signal time of the ring; $T_r = Ln_{eff}/c$, and L is the circumference of the ring. κ' is the coupling constant between the two rings. The propagating matrix (P) from one ring to another ring is:

$$P = e^{2(j\omega T_r/2 - \gamma L/4)}\begin{pmatrix} t' & -j\kappa' \\ -j\kappa' & t' \end{pmatrix}$$ (2.19)

The full transfer matrix (**M**) for a higher-order ring is then given by product of all the individual transfer and propagation matrices. For a second-order filter, the output at the drop (b_2), and the through port (b_1) is related to the input amplitude by:

$$Drop = \left|\frac{b_2}{a_1}\right|^2 = \left|\frac{jA\kappa^2\kappa'}{A_\phi t^2 - 2Att' + 1}\right|^2$$ (2.20)

$$T = \left|\frac{b_1}{a_1}\right|^2 = \left|\frac{t\left(1 + A_\phi\right) - At'\left(2t^2 + \kappa^2\right)}{A_\phi t^2 - 2Att' + 1}\right|^2$$ (2.21)

Where, $A = e^{\left(j\omega T_r - \gamma\frac{L}{2}\right)}$, and $A_\phi = e^{\left(j\omega 2T_r - \gamma L\right)}$.
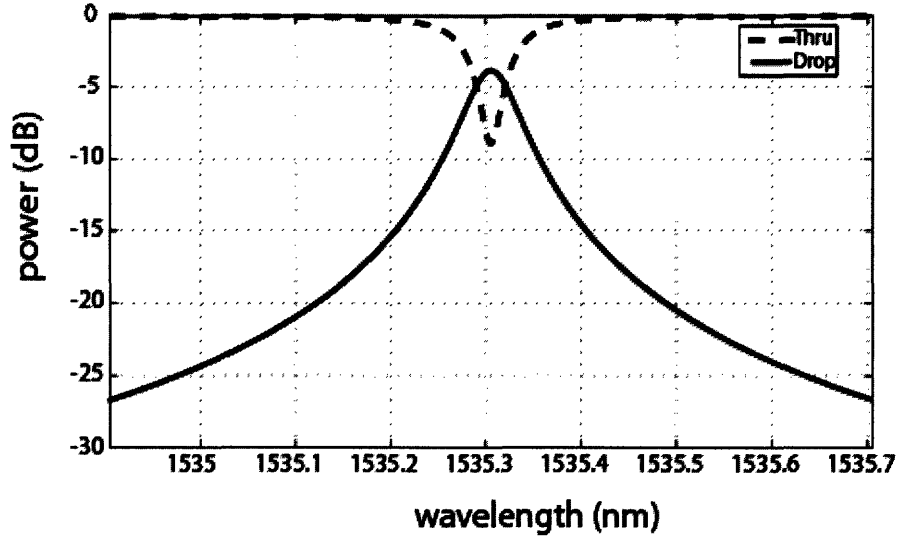
Figure 2-7: Second-order ring resonator: transmission curve (κ = 0.087, κ' = 0.7).

The quality factor (Q) is an important measure of the frequency selectivity of a ring. The Q-factor of a microring resonator is defined as the time averaged stored energy per optical cycle divided by the power leaving the resonator. The loaded Q includes coupling loss from the bus waveguide under working conditions and can be expressed as,

$$Q = \frac{\lambda_o}{\Delta\lambda_{1/2}} = \frac{v_o}{\Delta v_{1/2}}$$

(2.22)

Where $\Delta\lambda_{1/2}$ is the full width half maximum of the transmitted power, and it is proportional to the losses in the ring. Thus, the Q-factor of a ring is inversely proportional to the loss, and high Q-value is desirable for the application of interest. The internal Q-factor for the fabricated rings is within the range of 240,000–410,000, which corresponds to the propagation loss of around 1.5 dB/cm. For the given value of Q, the bandwidth for the passband is 25 GHz for the ring and a feasible channel spacing of 80 GHz is allocated between the filters, such that 20 filters can fit within the FSR range of 2 THz to give the desirable sampling rate of 40 GSPS as described in Chapter 1.

Another important parameter of a ring structure is finesse, which is related to the internal loss. Finesse is defined as,

$$f = \frac{FSR}{\Delta\lambda_{1/2}} \approx \frac{2\pi}{\gamma L} = \frac{1}{\gamma r}$$

(2.23)

where γ is the total internal loss of the ring. Higher loss leads to smaller finesse for the ring. To increase the finesse and the FSR, higher-order rings can be fabricated.

The transmission within the ring is governed by the internal and external losses in the device. As mentioned earlier, many important parameters of the ring depend on the loss. Important loss mechanisms in a ring resonator are bending loss, scattering loss due to surface roughness, coupling loss and material loss. High optical loss leads to small Q-value which is undesirable for the application of interest. The loss hampers the coupling of the light into and out of the ring, making the device less effective. Detailed studies have been done on the various loss mechanisms within waveguides [9], [15]-[21], and an optimized ring was designed for the purpose.

Second-order filters are fabricated with silicon-rich SiN (n = 2.2) cores and SiO_2 as a lower cladding and hydrogen silsequioxane (HSQ) as the upper and side cladding. With the use of an optimized annealing process, HSQ and SiO_2 have comparable, low refractive indices of 1.442 and 1.444 at 1.55 µm [21]. Hence, single-mode waveguides have submicron dimensions. HSQ was chosen as the upper cladding because of its gap filling property which was needed to fill in the high aspect-ratio gap between the ring and laterally coupled bus waveguide. The gap is one of the critical dimensions which determine the coupling coefficient.

The ring design was a part of research at MIT and design details can be found in ref. [19]. The design and optimization of the ring resonator is an effort of Milos Popovic and Anatoly Khilo, and the fabrication was done by Charles W. Holzwarth at MIT. Effort is being put into studying the multistage high-order rings with low loss [20], [22]. The dimensions for the rings and bus waveguide were optimized for low loss and large FSR [22]. Figure 2-6 shows an SEM picture of a second-order ring structure. The ring diameter of 20 µm, with group index of 2.3, gives a large FSR of 26 nm. The rings are fabricated such that the passband has 3 dB bandwidth of 25 GHz. Low drop loss (3.1 dB) and crosstalk of less than 30 dB has been obtained for these ring resonators.
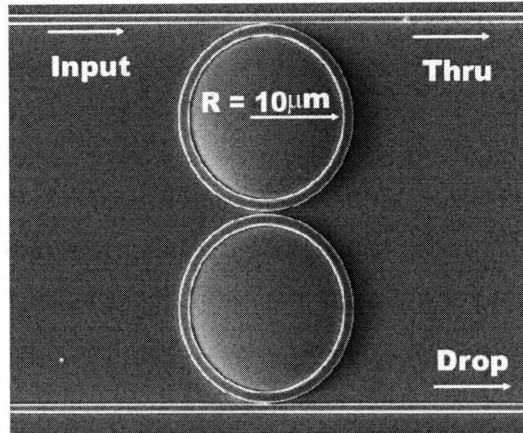
Figure 2-8: Top view of second-order microring resonator filter.

For the EPIC system, any fabrication error in the filters cause shifts in the resonant wavelength, which gives rise to the delay or the timing jitter for the optical sampling of the system. Apart from the dimensional errors during fabrication, other factors can also lead to shifts in the resonant wavelength. One of the main causes is the temperature variation of the filter. The spectral broadening of the optical pulse is called chirping, and for a chirped signal a shift in the wavelength leads to the time delay give by:

$$\Delta\tau = chirp[\,fs\,/\,nm] \times \Delta\lambda[nm] \tag{2.24}$$

If there is any disturbance in the resonant wavelength, the filters need to be tuned to its resonance condition. One can obtain the change in the wavelength of the filter by changing the effective index of the waveguide [23] as given by the formula below.

$$\frac{\Delta\lambda}{\lambda_o} = -\frac{\Delta n_{eff}}{n_{group}} \tag{2.25}$$

The change in the wavelength is related to both the effective index and the group index of the waveguide. When the refractive index is changed, the resonant wavelength varies due to change in the optical path length (nL) for the light traveling in the ring resonator. Also the coupling coefficient varies as the index changes. Let β be the propagation constant ($= n_{eff}\, 2\pi/\lambda_0$) at the resonant wavelength λ_o. The phase shift accumulated with one round trip in a ring filter is given by $\beta L = 2\pi N_i$ with N_i integer. If there is any change in the effective index, there is variation in the phase shift accumulated in the ring, thus changing the resonant wavelength. The index of the waveguide can be changed in different ways. Temperature variation is one of them and utilized here for tuning the ring filters. Other possibilities are also explored and explained in Chapter 3.

2.4   Summary:

Microring resonators are very useful optical devices which are used as tunable filters for wavelength division demultiplexing. When the resonance condition is satisfied, the power for the signal of certain frequency is transferred from the bus waveguide to the ring. At critical coupling, little to no signal is observed at these frequencies at the through port. This property of the ring resonator is utilized in EPIC for wavelength selective filter. Si-rich-SiN and SiO_2 are chosen as the material system for the ring resonator to give large index contrast. The dimensions and other parameters for the ring are based upon the system requirements. The rings are thermally tuned for maintaining a precise resonant frequency. The thermo-optic effect and the thermal tuning of the ring are discussed in the next chapter.

References:

1. R. A. Soref, "Silicon-Based Optoelectronics", Proceedings of the IEEE, Vol. 81, No. 12, Dec (1993).

2. E.A.J. Marcatili, "Bends in optical dielectric waveguides", The Bell System Technical Journal, Vol. 48, pp. 2103-32 (1969).

3. M. Nawrocka, T. Liu, X. Wang, "Tunable silicon microring resonator with wide free spectral range", Applied Physics Letters, Vol. 89 (2006).

4. B. E. Little, "Advances in Microring Resonators", Invited Talk, Integrated Photonics Research Conference (2003).

5. J. Haavisto, G.A. Pajer, "Resonance effects in low-loss ring waveguides", Optics Letters, Vol.5, No.12, pp. 510-12, Dec (1980).

6. K. Honda, E.M. Garmire, K.E. Wilson, K.E, "Characteristics of an integrated optics ring resonator fabricated in glass", Journal of Lightwave Technology, Vol.LT-2, No.5, pp. 714-19, Oct (1984).

7. B.E. Little, S. T. Chu, H. A. Haus, J. Foresi, and J.P. Laine, "Microring resonator channel dropping filters", Journal of Lightwave Technology, Vol. 15, No. 6, pp. 998-1005 (1997).

8. I. Kiyat, A. Aydinli, N. Dagli, "High-Q silicon-on-insulator optical rib waveguide racetrack resonators", Optics Express, Vol. 13, No. 6, March (2005).

9. T. Barwicz, H.A. Haus, "Three-Dimensional Analysis of Scattering Losses Due to Sidewall Roughness in Microphotonic Waveguides", Journal of Lightwave Technology, Vol. 23, No. 9, Sept (2005).

10. R. Marz, "Optical Waveguide Theory", Artech House, Boston 1995.

11. J.E. Heebner, V. Wong, A. Schweinsberg, R.W. Boyd, D.J. Jackson, "Optical Transmission Characteristics of Fiber Ring Resonators", IEEE Journal of Quantum Electronics, Vol. 40, No. 6, June (2004).

12. W.R. Headley, G.T. Reed, A. Liu, O. Cohen, D. Hak, M. Paniccia, S. Howe, I. Huille, "Fabrication of Optical Ring Resonators in Silicon on Insulator", Proceedings of SPIE, Vol. 5357, pp. 67-74 (2004).

13. A. Yariv, "Critical Coupling and Its Control in Optical Waveguide-Ring Resonator Systems", IEEE Photonics Technology Letters, Vol. 14, No. 4, April (2002).

14. A. Sakai, G. Hara, T. Baba, "Propagation Characteristics of Ultrahigh-Δ Optical Waveguide on Silicon-on-Insulator Substrate", Journal of Applied Physics, Vol. 40, pp L383-85 (2001).

15. A.N.M. Choudhary, T.R. Stanczyk, D. Richardson, A. Donval, R. Oron, M. Oron, "Method of Improving Light Coupling Efficiency Between Optical Fibers and Silicon Waveguides", IEEE Photonics Technology Letters, Vol. 17, No. 9 Sept (2005).

16. S.J. Emelett, R. Soref, "Design and Simulation of Silicon Microring Optical Routing Switches", Journal of Lightwave Technology, Vol. 23, No. 4, pp. 1800-1807, April (2005).

17. A.G. Rickman, G.T. Reed, F. Namavar, "Silicon-on-Insulator Optical Rib Waveguide Loss and Mode Characteristics", Journal of Lightwave Technology, Vol. 12, No. 10, Oct (1994).

18. D. Rafizadeh, J.P. Zhang, R.C. Tiberio, S.T. Ho, "Propagation Loss Measurements in Semiconductor Microcavity Ring and Disk Resonators", Journal of Lightwave Technology, Vol. 16, No. 7, July (1998).

19. T. Barwicz, M.A. Popović, P.T. Rakich, M.R. Watts, H.A. Haus, E.P. Ippen, H.I. Smith, "Microring-resonator-based add-drop filters in SiN: fabrication and analysis", Optics Express, Vol. 12, No. 7 (2004).

20. M.A. Popovic, T. Barwicz, M.R. Watts, P.T. Rakich, L. Socci, E.P. Ippen, F.X. Kartner, H.I. Smith, "Multistage high-order microring-resonator add-drop filter", Optics Letters, Vol. 31, No. 17, pp. 2571-2573, Sept (2006).

21. C.W. Holzwarth, T. Barwicz, H.I. Smith, "Optimization of Hydrogen Silsequioxane Films for Photonic Applications", accepted EIPBN, Denver (2007).

22. M.A. Popovic, M.R. Watts, T. Barwicz, P.T. Rakich, L. Socci, E.P. Ippen, F.X. Kartner, H.I. Smith, "High-index-contrast, wide-FSR microring-resonator filter design and realization with frequency-shift compensation", Optical Society of America (2003).

23. M. Popovic, "Theory and design of high-index-contrast microphotonic circuits", Ph.D. Thesis, Massachusetts Institute of Technology, Cambridge, MA (2008).

CHAPTER 3
THERMO-OPTIC EFFECT

3.1　Overview:

For wavelength division demultiplexing in the EPIC system, tunable filters have to be held at a precise resonant frequency. Any deviation in the frequency leads to the timing jitter in the signal as explained in Chapter 2. The deviation from a particular frequency might be due to fabrication errors or environmental temperature fluctuations. The thermo-optic effect is utilized for tuning, where the resonant frequency is trimmed by changing the effective index of the ring. The index change in induced by manipulating the ring temperature. Other alternatives for wavelength tuning and previous work on thermal tuning are discussed in Section 3.2. The thermo-optic effect in silicon-rich SiN is studied and explained in Section 3.3. Experimental results showing the thermal tuning of Si-rich-SiN rings are discussed in Section 3.4. Metal heaters are designed to sit on top of the rings for on-chip thermal tuning. The design process involved in making a power efficient heater for thermal tuning is explained in Chapter 4 along with descriptions of all heater designs.

3.2　Background:

The resonant frequency of the ring resonator has to be stabilized within 100 MHz to ensure that the timing jitter is within the device specification. There are various ways to tune a ring resonator. One of the ways to change the resonant frequency is by changing the effective index of the ring, and that can be accomplished by electro-optic effect. The electro-optic effect is a change in the optical properties of a material in response to an applied electrical field. Polymer microrings have been tuned with electro-optic effect which is relatively faster tuning mechanism, but the maximum achievable index of refraction change is small leading to the tuning range of less than 1nm [1]. Bulk and unstrained silicon has zero linear electro-optic coefficient (Pockel's effect). Kerr effect (non-linear) is observable only under large electric field. One of the future considerations for the SiN ring resonator is to move to pure Si material, which is more compatible with the current CMOS technology. Also, the material loss in silicon is less than SiN. No electro-optic effect in SiN has been reported till now. Thus, the electro-optic effect is not used for the

tuning purposes. Mechanical tuning is also popular for wavelength tuning of resonators. Micro-electro-mechanical systems (MEMS) actuators are used in ref. 2 to physically change the air gap to change the coupling and effective index of the waveguide. The precision and stability that can be obtained with MEMS tuning is very crude compared to other tuning mechanisms. The refractive index of a silicon nitride waveguide can be changed by oxygen plasma treatment such that the material composition of the waveguide is changed to form oxy-nitride, and a large shift in the resonant wavelength of 8.9 nm has been shown experimentally [3]. The other popular way of controlling the resonant frequency of these passive devices is thermal tuning. The thermo-optic effect is utilized to achieve a desired resonant frequency of the ring. As the name suggests, the effect relates any kind of thermal change in the ring to the variation in the optical property of the device. In this case, the change in the temperature of a ring waveguide leads to a change in the effective refractive index. The optical path length of the heated waveguide is changed due to the change in the effective refractive index, which causes shift in the resonant frequency. Details are described in Section 3.3.

Thermal tuning has been reported for various ring resonator structures as summarized in Table 3-1. Polymers have very low thermal conductivity and high thermo-optic coefficients ($\sim 10^{-4}$ i.e. an order of magnitude higher than SiN), thus thermo-optic tuning of polymer rings is very efficient. Details on physical mechanism behind thermal tuning is in Section 3.3. InP/InGaAsP microrings, fabricated with wafer-bonding using polymer (BCB), have been tuned with low power consumption of 26 μW/GHz [4]. A wavelength tuning of 16 nm was demonstrated with the input power of 50 mW. The marvel of such a large tuning range and low power for the ring discussed in ref. 4 is less exciting because of the fact that the rings were 20 μm in radius giving very small FSR of 5 nm. As mentioned earlier, large FSR is desired for communication applications, as many channels can be utilized in parallel for WDM to get large sampling rate. Vertically coupled microrings made of polyimide have been tuned with 50 μW/GHz, showing the total tuning of 9.4 nm with low power consumption of 60 mW [5]. However, microrings made of materials compatible with CMOS processing are preferred for electrical and optical integrated circuits. Earlier work on thermal tuning of ring resonators involved large scale devices such as 2 mm diameter Si_3N_4 ring with poly-silicon heaters [6]. A poly-Si resistor was used for the first time as a thermistor to measure the temperature of the waveguide. A first-order silicon ring has been tuned with low power of 28 μW/GHz and large tuning range of 16 nm [7]. In most of this early work, the heater design and the tuning power were not considered as the important factors, and the heating mechanism was not optimized. A single Si_3N_4 ring has been reported with a tuning

range of 20 pm/K and a tuning power of 400 μW/GHz [8]. The largest shift seen in this work was 3.6 nm for 180 mW of input electrical power. Microrings made of HIC material system, Hydex, has tuning rate of 17 pm/K [9]. In more recent works, small silicon rings (~ 2 μm radius) with large FSR (47 nm) and high Q-factor (~6730) have been thermally tuned with tuning range of 0.11 nm/K [10].

Material	Thermo-optic coefficient (dn/dT)	Tuning power	Tuning range	Ref.
InP/InGaAsP + BCB	-1.1×10^{-4} /°C	26 μW/GHz	16 nm	[4]
Polyimide	-5 to -7×10^{-5} /°C	50 μW/GHz	9.4 nm	[5]
Si	1.9×10^{-4} /°C	28 μW/GHz	16 nm	[7]
Si$_3$N$_4$	4.5×10^{-5} /°C	400 μW/GHz	3.6 nm	[8]
Si-rich-SiN	4.5×10^{-5} /°C	80 μW/GHz	<1 nm	This work

Table 3-1: Summary of previous work for thermal tuning of ring resonator.

In this thesis, efficient thermal tuning for Si-rich-SiN second-order filters is shown with a tuning power of 80 μW/GHz. This is the first attempt for such low power thermal tuning for a higher-order microring resonator made of Si-rich SiN. For the application, the maximum tuning range equivalent to a single filter channel spacing of ~ 0.7 nm is sufficient. One of the key aspects of ensuring efficient thermal tuning is to have an optimized heater design. Heater designing and optimization are described in detail in Chapter 4.

3.3 Thermo-optic Effect:

The change in temperature leads to many variations within the atomic structure of the material. In most intrinsic semiconductors, the change in the refractive index due to temperature variation is attributed to the thermal expansion and the change in the bandgap energy due to change in electron distribution. All materials have thermal expansion coefficient (SiN: 3.3×10^{-6} /°C) which relates the increase in the dimensions due to the temperature rise. For most semiconductor materials, the effect of thermal expansion is negligible due to small thermal expansion coefficients. However, in polymers, the expansion coefficient can be large (PMMA: 7.7×10^{-5} /°C). The refractive index varies according to the thermo-optic coefficient (dn/dT) which tells the effective change in the refractive index for 1°C change in the material temperature. Various factors affect the coefficient value including operating frequency range, crystal orientation,

operating temperature, doping concentration etc. Depending on the material, they can have positive or negative thermo-optic coefficient such that the refractive index increases or decreases with change in temperature.

Any formal study of the temperature dependence of the refractive index for Si-rich SiN has not been published in literature. However, closely related materials such as silicon, silicon dioxide, amorphous silicon nitride (Si_3N_4), and silicon-rich silicon oxide thin film have been studied. The refractive index of silicon-rich-SiN at room temperature falls in between pure silicon (3.45) and Si_3N_4 (2.05), depending on the content of silicon.

For silicon (both crystalline and amorphous), the thermo-optic effect is predominantly due to the temperature dependent bandgap energy. As the energy shifts, the refractive index also varies which depends on the bandgap [11]. The bandgap shift is mostly due to the electron-phonon interaction [12, 13]. The lattice expansion due to the thermal energy also causes the shift in bandgap, but the contribution is minimal compared to the electron-phonon interaction [12]. As the temperature increases, the inter-atomic spacing increases due to atomic vibrations. It decreases the average potential seen by an electron in a material and thus the bandgap decreases. The shift in energy can be calculated using perturbation theory i.e. Debye-Waller effect [12]. Varshni proposed a simple equation for temperature dependent bandgap energy [12].

$$E_g(T) = E_g(0) - \frac{\Lambda T^2}{T + \Pi}$$

(3.1)

where E_g (0) is the bandgap energy at 0 K, and Λ and Π are the fitting parameters which varies according to the material. The underlying assumption for this simplified equation is that the bandgap energy is proportional to T at high temperatures, and T^2 at low temperatures. The Sellmeier equation is an empirical relation between the refractive index and the operating wavelength, and it has been generalized to generate the temperature and wavelength dependent refractive index model (n (λ, T)) for an adequate fit for the empirical data for silicon and germanium [14].

In general, Si-rich-SiN is formed by the nucleation of Si clusters in a dielectric host [15]. As the silicon concentration increases, the optical properties, namely refractive index, are governed by the silicon atoms [15]. Si-rich-SiN formed by low pressure chemical vapor deposition (LPCVD) shows excess Si in the form of nanocrystals whose size depends on the temperature. The optical constants of the film depend on the stoichiometry (i.e. the ratio of the concentration of the Si and

N atoms). Higher Si concentration increases the refractive index value for silicon nitride [16-18]. Similarly, if the oxygen concentration is increased to form oxy-nitride, the index value goes down [17, 18]. The model for the dielectric function for silicon-rich silicon nitride described in ref. [19] has been obtained by generalizing the Philipp model where the Si-tetrahedral is the fundamental subunit. In this model, the dielectric response for SiN has been obtained with the scaled mixed response of a-Si and a-Si$_3$N$_4$. The model includes the average effective number of the electrons according to the stoichiometry and the average energy gap is calculated for the material from a-Si and a-Si$_3$N$_4$. Good agreement between the model and the experimental results for various wavelengths are shown in the reference [19].

For the silicon-rich silicon oxide thin film, the refractive index increases with increasing temperature and the index also increases by increasing the content of silicon [20] which is similar to silicon-rich SiN. The silicon rich oxide thin film consisted of nanocrystal silicon embedded inside the silicon dioxide matrix. The temperature dependent refractive index for Si-rich silicon oxide was modeled well with the theories relating index change to the temperature dependent bandgap (Varshni's model: Equation 3.1). For a given temperature change, the shift in the index and the bandgap energy is related by the Moss rule and it fits well for the experimental results for Si-rich silicon oxide [20].

$$4\frac{\Delta n}{n} = -\frac{\Delta E_g}{E_g} \qquad (3.2)$$

Using similar analogy from Si-rich silicon oxide, it can be concluded that for Si-rich SiN, the temperature induced change in the refractive index is mostly due to change in the bandgap energy.

For the EPIC system, a large number of filters are arranged in array to form filter banks such that the sampling rate is enhanced by the number of filters in the bank. Figure 3-1 shows an SEM picture of a second-order filter and a schematic of a two channel filter bank with input, output and drop ports. The ring resonators are fabricated with target channel spacing of 80 GHz with 5 GHz standard deviation due to random process variations, which cannot be corrected during fabrication. The 5 GHz deviation in the frequency corresponds to the dimensional uncertainty of 40 pm in the radius of the ring. Thus, a postfabrication tuning technique is required. In this work, thermal tuning is proposed for post fabrication trimming of the HIC microring resonators for stable and precise resonant frequency control. Thermal tuning with micro-heaters is beneficial due to its ease of integration and low power consumption.

(a)   **(b)**
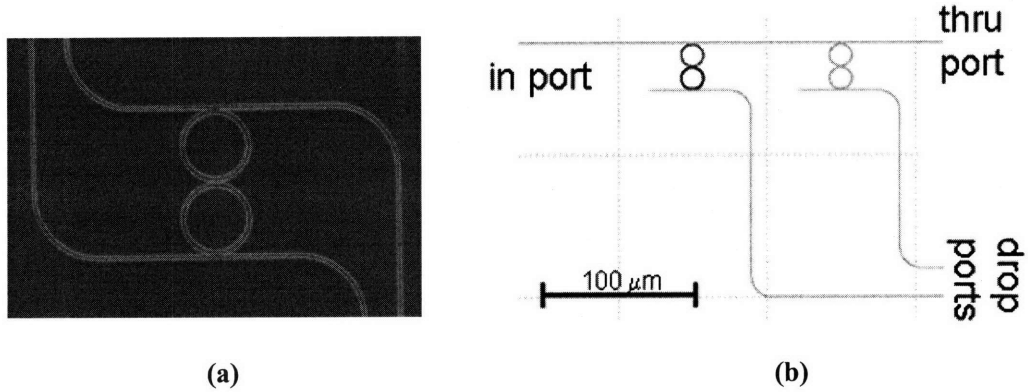
Figure 3-1: (a) SEM picture of second-order filter (top view) (b) Two channel filter bank layout.

In the case of a HIC ring resonator, when the refractive index changes, there is a shift in resonant wavelength as shown by the following relation [21].

$$\frac{\Delta\lambda}{\lambda_o} = -\frac{\Delta n_{eff}}{n_{group}} = -\frac{1}{n_{group}}\frac{\partial n_{eff}}{\partial T}\Delta T \tag{3.3}$$

For EPIC, dynamic tuning is not required as the purpose of thermal tuning is to compensate for any fabrication errors and, or environmental temperature fluctuations that might occur within the device. They do not require large tuning range. However, the sensitivity of the temperature control for the ring is critical.

As mentioned earlier, the thermo-optic coefficient of a material is temperature dependent as well as wavelength dependent. At 1.55 μm, the thermo-optic coefficients for SiN and SiO$_2$ are 4e-5 K^{-1} and 1.5e-5 K^{-1} respectively. In the case of a waveguide structure, the shift in resonant wavelength can be attributed to change in refractive index of the core and the cladding. As the temperature of the ring changes, the refractive index of both the core and the cladding material changes which causes the shift in the resonant wavelength for the ring structure. Equation 3.4 gives the tuning range for the waveguide [21].

$$\frac{\Delta\lambda}{\Delta T} = -\frac{\lambda_o}{n_{group}}\left(\frac{\partial n_{eff}}{\partial T}\right) = \frac{\lambda_o}{n_{group}}\left(\frac{\partial n_{eff}}{\partial n_{core}}\frac{\partial n_{core}}{\partial T} + \frac{\partial n_{eff}}{\partial n_{lc}}\frac{\partial n_{lc}}{\partial T} + \frac{\partial n_{eff}}{\partial n_{uc}}\frac{\partial n_{uc}}{\partial T}\right) \tag{3.4}$$

For a SiN core, HSQ upper cladding, and SiO$_2$ lower cladding, the group index is 2.29 at 1550 nm, and the theoretical tuning range is 28 pm/K ~ 3.55 GHz/K. If only effective refractive index (1.46) is used for the theoretical prediction, the thermal tuning range for the Si-rich-SiN

waveguide is 44 pm/K which is an over-estimate compared to what has been measured and reported in literature. HSQ is a type of spin-on-glass material and it is assumed to have the same thermo-optic coefficient as silicon dioxide. For the theoretical calculation, the thermo-optic coefficient is taken to be a constant value for all operating temperature. However, experiments on silicon have shown the thermo-optic coefficient to vary with temperature [22-24].
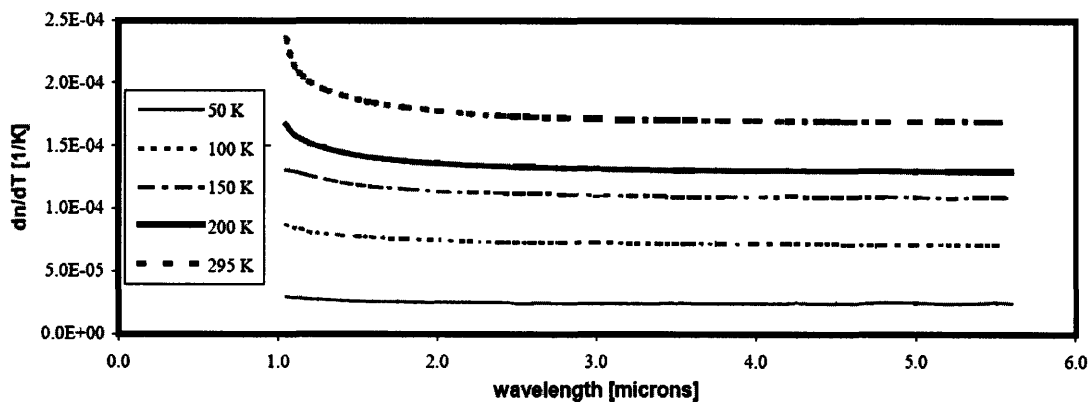
(a)
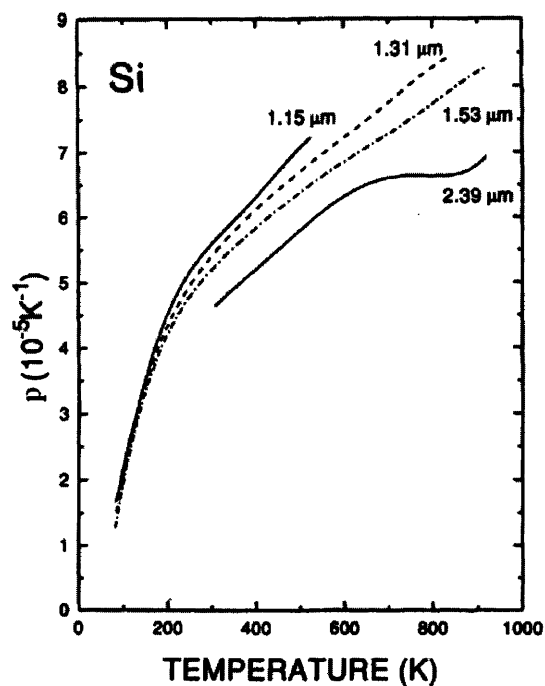
(b)

Figure 3-2: (a) Experimental data showing various thermo-optic coefficients at different operating temperatures for Silicon [Ref. 22], (b) p = (1/n) (dn/dT) for Silicon [Ref. 23].

From ref. 23, the temperature dependence of the thermo-optic coefficient for silicon near the room temperature (~ 373 K) can be estimated to be 2.2e-8. Since the refractive index of Si-rich SiN is closely governed by the silicon content of the material, the temperature dependence of the thermo-optic coefficient will also be similar to that of silicon. The temperature dependence of the thermo-optic coefficient might be one of the causes for slight variation in the experimental results which are discussed in the next section.

For the experimental verification, the optical output at the drop port of the ring resonator is analyzed to study the thermal tuning effects. Figure 3-3 shows the output spectrum of an 8 μm radius second-order SiN ring resonator showing the free spectral range (FSR) of 22 nm and the peak at 1538.5 nm which is consistent with the geometry of the resonator. A mismatch between the resonant frequencies of the two rings of a single filter causes two peaks at the drop spectrum as seen at 1560 nm in Figure 3-3. The mismatch might be due to the difference in the ring dimensions or coupling coefficient mismatch between the two rings.
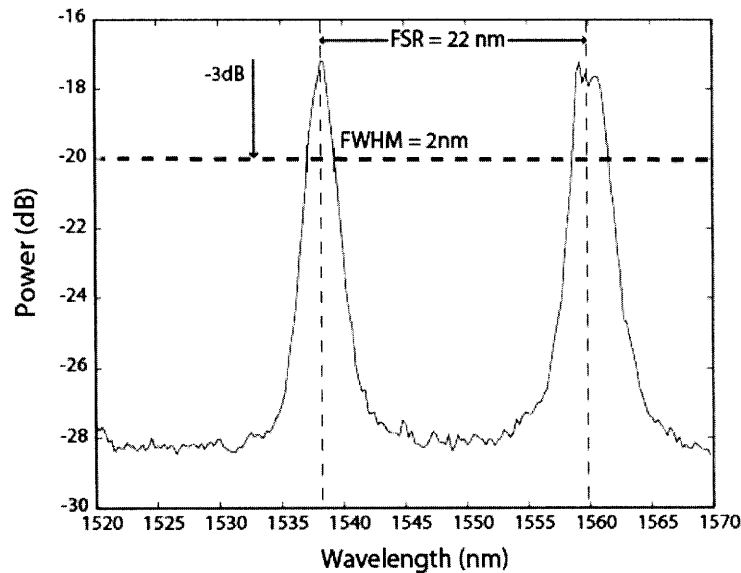
Figure 3-3: Optical spectrum for a second-order filter at drop port: full spectrum showing FSR with first resonance peak shown at ~1538.5nm

3.4   Thermal Tuning (External Heating):

To confirm the thermal tuning before HSQ deposition, experiments were performed on the second-order filters with air as the upper-cladding using external heaters. Figure 3-4 shows the

cross-section of the ring with silicon dioxide as lower-cladding and air as upper-cladding for the test sample.
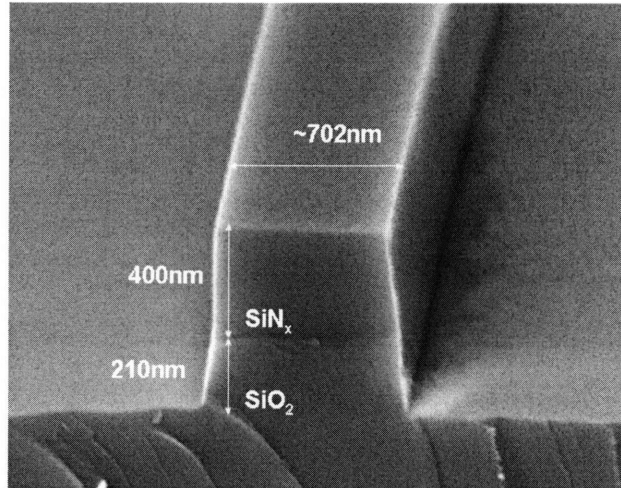
Figure 3-4: Cross-section for the ring waveguide showing SiO$_2$ as lower-cladding below SiN.

A schematic of the experiment for the thermal tuning measurement with the external heating is shown in Figure 3-5(a). An Agilent Lightwave measurement system (8164A) is used as the light source with the wavelength range of 1510-1640 nm. The light enters the waveguide through a polarization maintaining (PM) single mode lensed fiber. Using an x-y-z piezo cube and the piezo servo controller, the fiber is aligned very close to the input waveguide of the filter. At the other end of the sample, the light is collected onto a photodetector through free space coupling using a 100x microscope objective. An adjustable mirror allows focusing the beam spot to an infra-red camera (Micron-viewer 7290A) or the photodetector. The voltage corresponding to the optical signal hitting the photodetector is read through a DAQ (6020E) that is connected to a computer.

(a)

(b)
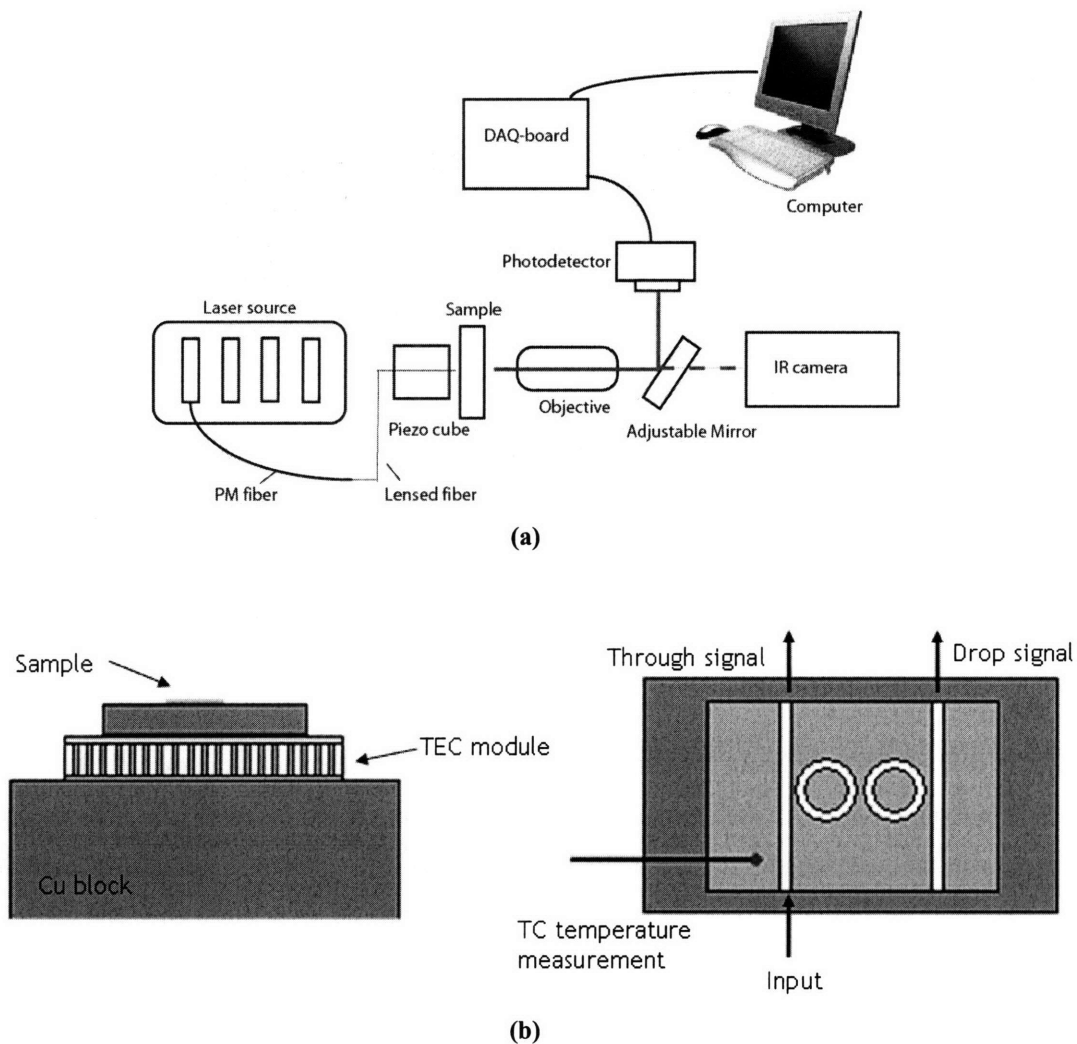
Figure 3-5: (a) Experimental setup for measuring the optical output of the resonator to show the thermal tuning (b) Placement of the sample on TEC.

The microrings are designed to support a transverse electric (TE) fundamental mode. Thus, polarization is an important issue during experiment. In non-PM fibers, there is polarization scrambling along the length and the output signal at the drop port is very low. Optical amplifiers could not be used during the experiment due to the polarization restriction. As the light was injected into the waveguide, the fiber was rotated and aligned such that there was maximum optical signal at the drop port. If the optical amplifier was to be used, the fiber would have to be re-aligned every time when the amplifier is turned on since the light coming out from the amplifier is not along the same axis each time. Thus, an optical amplifier was used only during fiber alignment and aligning the free-space coupling components. The fiber alignment is very susceptible to disturbance from the surrounding environment where the experiment was carried.

Strong air flow around the setup or vibration to the optical table was enough to misalign the fiber tip. The sample was heated using a thermo-electric cooler (TEC) and a temperature controller (ILX Lightwave LDC 3714). The TEC module was set at a fixed temperature and a micro-thermocouple was used to measure the temperature at the top of the sample (Figure 3-5 b). Thermal simulations done in FEMLAB show that the actual temperature of the ring and the top of the sample vary by as much as 17%.

One of the earlier observations in the experiment was a broad spectrum at the output for various sample temperatures. The broadness in the spectrum was mainly due to dust accumulation on the rings which increases the total loss of the resonator, which is indeed seen as a broader peak and a lower Q value. The sample was rinsed in ethanol in an ultrasonic wave cleaner and this caused the peaks to be narrower. Figure 3-6 shows the output spectrum of the ring at various temperature before the sample was cleaned. The actual output for the ring after cleaning is shown in Figure 3-7.
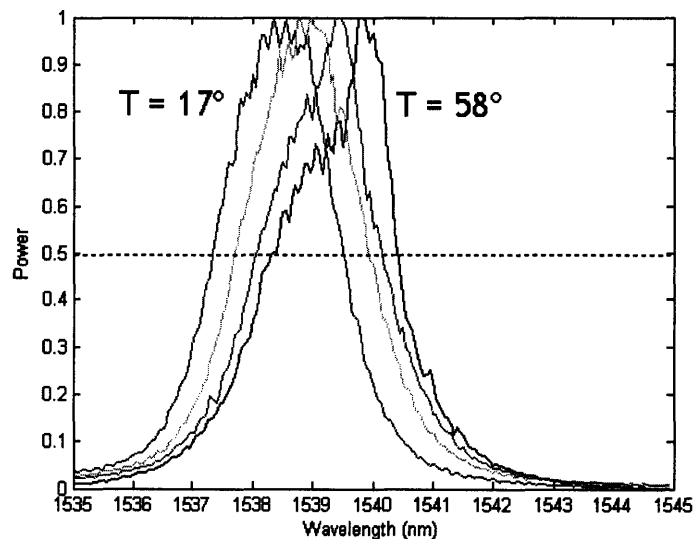
Figure 3-6: Optical spectrum of the second-order filter as the temperature of the sample is increased. The broad peak is mostly due to dust particles on the rings.

The temperature of the sample was changed by increasing the TEC's set temperature. Figure 3-7 shows the shift in resonant wavelength of the second-order filter as the temperature rises from 21°C to 70°C.
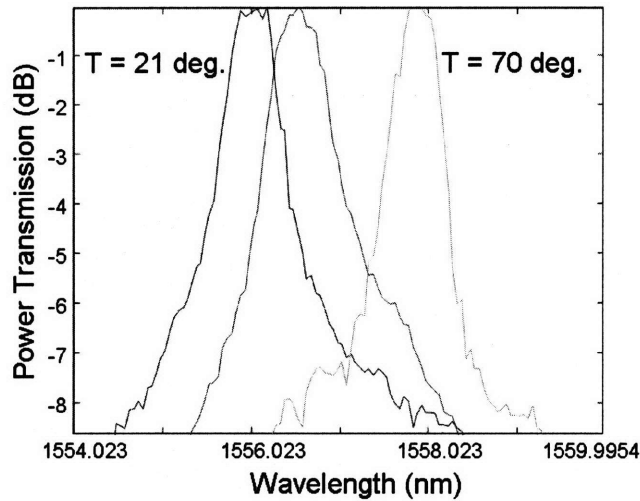
Figure 3-7: Optical spectrum of the second-order filter as the temperature of the sample is increased (after cleaning).

The resonant wavelength is taken to be the wavelength with maximum power at each temperature. The plot shown in Figure 3-8 summarizes the shift in resonant wavelength due to the change in temperature of the sample as measured by the thermocouple. A linear fit gives the tuning range of 36 pm/K.
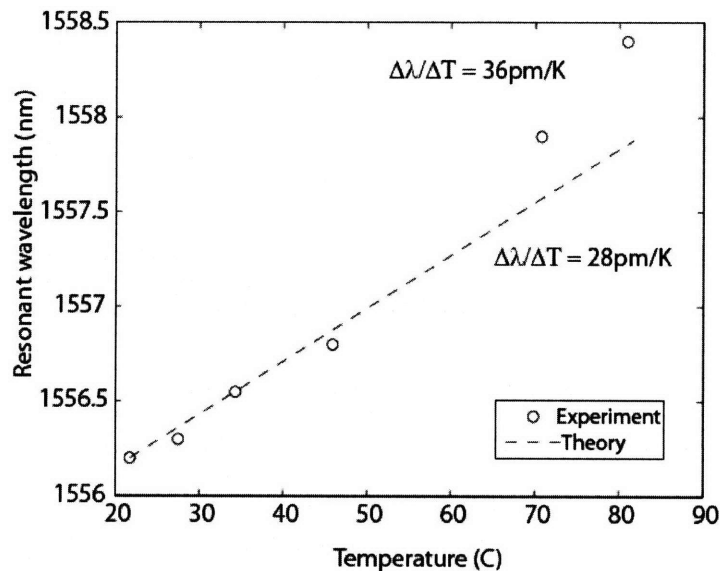
Figure 3-8: Thermal tuning for the second-order filter (without overcladding) is observed by changing temperature of the rings. Total shift of 2.2nm is seen due to heating the rings from 21°C - 81°C.

The second-order filter with over-cladding of HSQ was measured with similar procedure to get more accurate results for thermal tuning. The resonant wavelength shift for increase in the ring temperature is shown in Figure 3-9. To get an accurate tuning range, the temperature of the ring waveguide is needed. The micro-thermocouple measures only the top of the sample. Using FEMALB, the temperature of the rings can be predicted by knowing the temperature of the top of the sample and the TEC set temperature at the bottom of the sample. Figure 3-10 shows the plot for resonant wavelength shift versus the temperature of the rings. When linear dependency is assumed, the tuning range of 30 pm/K is obtained, which is within 7% of the theoretical prediction for the Si-rich SiN waveguide.
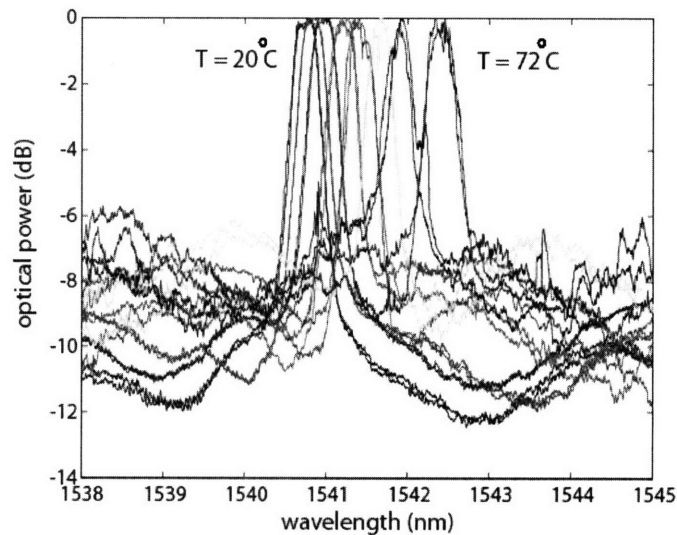
Figure 3-9: Optical spectrum of the second-order filter (with HSQ overcladding) as the temperature of the sample is increased.

At higher operating temperature, the peak broadens and the extinction ratio decreases. This is mainly due to the frequency mismatch between the resonance peaks of the two rings which causes the total output power to decrease. Also, it was observed that the accuracy of the TEC controller at higher temperature above 40°C was ±0.5°C due to fluctuation in the set temperature-the PID constants that keep the set temperature constant at lower temperature do not work very well at high temperature.
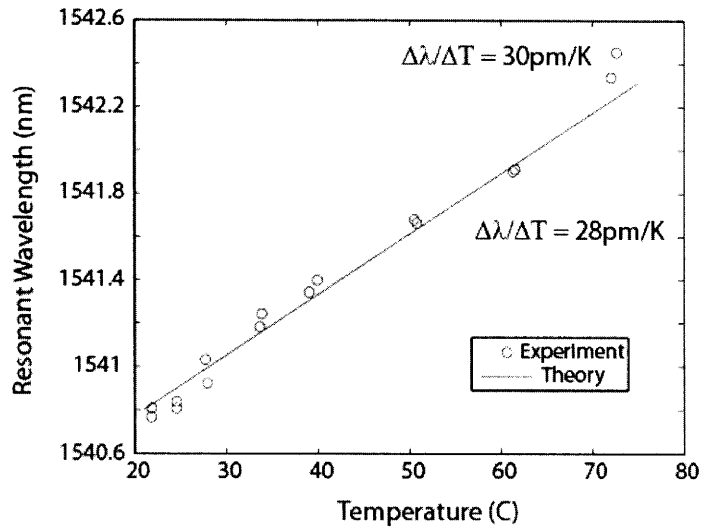
Figure 3-10: Thermal tuning for the second-order filter (with HSQ over-cladding) is observed by changing temperature of the rings.

3.5 Summary:

The thermal tuning for a second-order Si-rich-SiN ring resonator using external heaters is shown in this chapter. The final data for thermal tuning is obtained by heating the rings using on-chip heaters that are described in the next chapter. The tuning range for the SiN waveguide was measured to be 30 pm/K which matches well with the theoretical prediction. The power consumption for the thermal tuning will be obtained from similar experiment described in this chapter using on-chip heater. The heater designs and optimization parameters are described in the next chapter.

References:

1. P. Rabiei, W.H. Steier, "Tunable Polymer Double Micro-Ring Filters", IEEE Photonics Technology Letters, Vol. 15, No. 9, Sept (2003).

2. T. Mamdouh, D. Khalil, "A MEMS tunable optical ring resonator filter", Optical and Quantum Electronics, Vol. 37, pp 835-53, (2005).

3. T. Wang, Y. Huang, H. Chen, "Resonant-Wavelength Tuning of Microring Filters by Oxygen Plasma Treatment", IEEE Photonics Technology Letters, Vol. 17, No. 3, March (2005).

4. I. Christiaens, D. Van Thourhout, R. Baets, "Low-power thermo-optic tuning of vertically coupled microring resonators", Electronics Letters, Vol. 40, No. 9, April (2004).

5. Y. Kokubun, "Wavelength Selective Integrated Device by Vertically Coupled Microring Resonator Filter", IPAP Books 2, pp. 303-316 (2005).

6. P. Heimala, P. Katila, J. Aarnio, A. Heinamaki, "Thermally Tunable Integrated Optical Ring Resonator with Poly-Si Thermistor", Journal of Lightwave Technology, Vol. 14, No. 10, Oct (1996).

7. F. Gan, T. Barwicz, M.A. Popovic, M.S. Dahlem, C.W. Holzwarth, P.T. Rakich, H.I. Smith. E.P. Ippen, F.X. Kartner, "Maximizing the Thermo-optic Tuning Range of Silicon Photonic Structures", Proceedings Photonics in Switching (2007).

8. D.H. Geuzebroek, E.J. Klein, H. Kelderman, F. S. Tan, D.J.W. Klunder, A. Driessen, "Thermally Tunable, Wide FSR Switch based on Micro-ring Resonators", Proceedings Symposium IEEE/LEOS Benelux Chapter, (2002) Amsterdam.

9. B.E. Little, S.T. Chu, P.P. Absil, J.V. Hryniewicz, F.G. Johnson, F. Seiferth, D. Gill, V. Van, O. King, M. Trakalo, "Very High-Order Microring Resonator Filters for WDM Applications", IEEE Photonics Technology Letters, Vol. 16, No. 10, Oct. (2004).

10. M.S. Nawrocka, T. Liu, X. Wang, R.R Panepucci, "Tunable silicon microring resonator with wide spectral range", Applied Physics Letters, Vol. 89, N0. 071110, (2006).

11. G. Cocorullo, F.G. Della Corte, I. Rendina, "Temperature dependence of the thermo-optic coefficient in crystalline silicon between room temperature and 550 K at the wavelength of 1523 nm", Applied Physics Letters, Vol. 74, No. 22, May (1999).

12. R.D. King-Smith, R.J. Needs, V. Heine, M.J. Hodgson, "A First-Principle Calculation of the Temperature Dependence of the Indirect Band Gap of Silicon", Euro Physics Letters, Vol. 10, No. 6, pp. 569-574 (1989)

13. R. Bhargava, "Properties of Wide Bandgap II-VI Semiconductors", IEEE EMIS Data Review Series 17, INSPEC Publications (1997).

14. B.J. Frey, D.B. Leviton, T.J. Madison, "Temperature-dependent refractive index of silicon and germanium" Proceeding of the SPIE, Vol. 6273, pp. 62732J, July (2006).

15. L. Dal Negro, J.H. Yi, J. Michel, L.C. Kimerling, T.W.F. Chang, V. Sukhovatkin, E.H. Sargent, "Light emission efficiency and dynamics in silicon-rich silicon nitride films", Applied Physics Letters, Vol. 88, No. 233109 (2006).

16. V.Em. Vamvakas, N. Vourdas, S. Gardelis, "Optical characterization of Si-rich silicon nitride films prepared by low pressure chemical vapor deposition", Microelectronics Reliability, Vol. 47, pp. 794-797 (2007).

17. W.R. Knolle, "Correlation of refractive index and silicon content of silicon oxynitride films", Thin Solid Films, Vol. 168, pp. 123-132 (1989).

18. M. Villa, E. Roman, C. Prieto, "Electrical conduction mechanism in silicon nitride and oxy-nitride-sputtered thin films", Journal of Applied Physics, Vol. 97, No. 113710, June (2005).

19. D.E. Aspnes, J.B. Theeten, "Dielectric function of $Si-SiO_2$ and $Si-Si_3N_4$ mixtures", Journal of Applied Physics, Vol. 50, No. 7, July (1979).

20. S. Seo, J. Lee, J.H. Shin, E. Kang, B. Bae, "The thermo-optic effect of Si nanocrystals in silicon-rich silicon oxide thin films", Applied Physics Letters, Vol. 85, No. 13, pp. 2526-28 (2004).

21. M. Popovic, "Theory and design of high-index-contrast microphotonic circuits", Ph.D. Thesis, Massachusetts Institute of Technology, Cambridge, MA (2008).

22. F.J. Bradley, L.B. Douglas, M.J. Timothy, "Temperature-dependent refractive index of silicon and germanium", http://arxiv.org/ftp/physics/papers/0606/0606168.pdf

23. J.A McCaulley, V.M. Donnelly, M. Vernon, I. Taha, "Temperature dependence of the near-infrared refractive index of silicon, gallium arsenide, and indium phosphide", Physical Review B, Vol. 49, No. 11 (1994).

24. F.G. Della Corte, M. Bellucci, G. Cocorullo, M. Iodice, I. Rendina, "Measurement and Exploitation of the Thermo-Optic Effect in Silicon for Light Switching in Optoelectronic Integrated Circuits", Proceedings of SPIE, Vol. 3953 (2000).

CHAPTER 4

HEATER DESIGN & THERMAL TUNING POWER

4.1 Overview:

Designing a heater with low power consumption for the thermal tuning of the ring resonator is an important part of this project. The key requirement for the heater design is the high power efficiency for thermal tuning. For EPIC, the power efficiency for tuning and the wavelength stability are more important metrics than the overall tuning range, as the requirement is to stabilize the output of the rings at a certain frequency. Thermal tuning can be utilized for two applications: large tuning range or low power consumption. The optimization parameters for the two requirements are slightly different and will be explained in the later section of the chapter. The heaters serve the dual purpose of heating the rings as well serving as sensors for temperature measurements. Various heater geometries are studied using the three-dimensional finite element simulations (FEMLAB). Experimental techniques such as the 3ω-method and thermoreflectance are used to verify and characterize the micro-heater performance. For better understanding of the heat transfer in the device, the various modes of heat transfer are described along with the boundary conditions used for the theoretical simulations. The finite element simulations of three different types of heaters are described and the most power efficient heater is chosen.

4.2 Heat Transfer:

Finite element simulation is utilized to estimate the temperature profile of the heater due to joule heating. The energy is dissipated from a resistive heater and it is assumed that all the electrical power contributes to the heating of the element. FEMLAB estimates precise temperature at any given point of the sample. The boundary conditions and electrical-thermal model used are described below.

4.2.1 Modes of Heat Transfer:

Heat transfer is the flow of energy due to a difference in temperature. Conduction, convection and radiation are the three modes of heat transfer [1]. For designing a heater, it is important to understand the heat flow in the device such that the temperature of the ring resonator can be predicted by knowing the electrical input power to the heater.

For conductive heat exchange, the energy is transferred via vibration of molecules within the medium. It is a common mode of heat transfer in solids. The mathematical model for conductive heat transfer is give by:

$$Q = \frac{C}{Vol.}\frac{\partial T}{\partial t} + \nabla.\left(-\xi \nabla T\right)$$ (4.1)

The total heat flux [Q - W/m^3] transferred through conduction is related to the volume [Vol. - 1/m^3], heat capacity [C - J/K], and thermal conductivity [ξ - W/m K] of the material. For a steady state model, the temperature does not change with time, thus, reducing the conductive heat transfer model to a simpler expression.

$$Q = \nabla.\left(-\xi \nabla T\right)$$ (4.2)

The convective heat transfer is carried via fluid flow, which is characterized by the heat transfer coefficient 'h'. For a solid to air interface, the natural convection heat transfer coefficient is taken to be 5 W/m^{2}K [2]. The total power distributed within an area 'A' due to convection is given by,

$$Q = \frac{hA\Delta T}{Vol.}$$ (4.3)

Radiation is the mode of heat transfer when there is exchange of thermal radiation (electromagnetic radiation) energy between two bodies. An implicit assumption for the heater model is that there is no radiation and no loss of heat from any other mechanism apart from conduction and convection. Thus, the focus of the heat transfer will be on these two modes.

4.2.2 Boundary Conditions:

There are two types of boundary conditions for solving the heat flow in a system: the Dirichlet type and the Neumann type [2]. For Dirichlet type boundary condition, the temperature of the boundary is set to a fixed value. Whereas in the Neumann type, the heat flux across the boundary is specified.

For a heat source, such as a resistive heater, the heat flux can be specified as q_0 [W/m^2] which enters the domain and is transferred through conduction and convection to the surrounding environment. $\hat{n}$ is the normal vector of the boundary.

$$q_o = -\hat{n}.(-\xi\nabla T) - h(T_{inf} - T) \qquad (4.4)$$

Equation 4.4 is the energy balance model where the input heat flux (q_o) is dissipated through conduction and convection (Equations 4.2 and 4.3), represented by the two terms in the right hand side of the equation. For the EPIC system, there are multiple filters in an array. Instead of modeling the entire system, we can use the symmetry of the system to our advantage. Figure 4-1 shows a schematic of a filter bank, where a single second-order filter can be simulated as a unit block. The condition of symmetry is useful for the reduced model size as in the case of this theoretical modeling. According to the condition of symmetry, the temperature gradient across the boundary is zero.

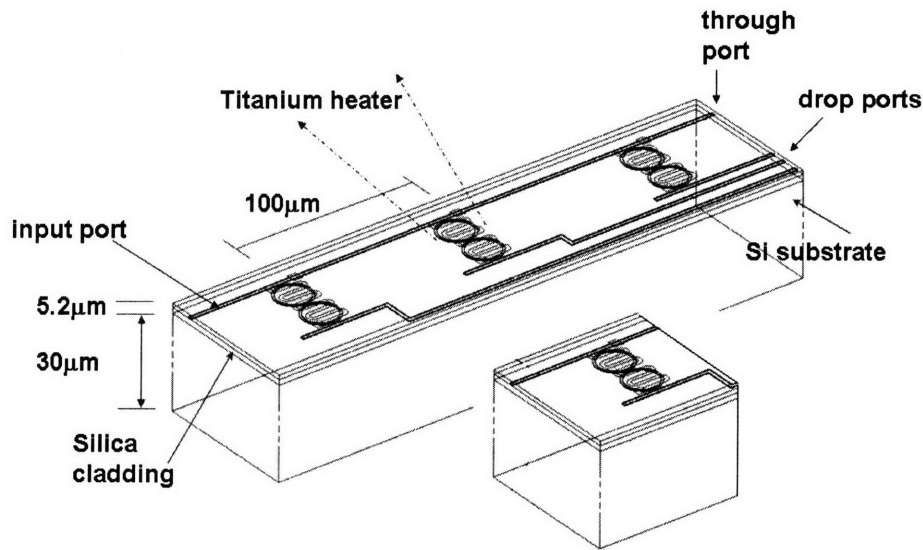$$-\hat{n}.(-\xi\nabla T) = 0 \qquad (4.5)$$

Figure 4-1: A single second-order filter can be used as unit cell to get thermal distribution for a larger number of filter banks.

The interior boundaries have the condition of continuity, according to which the normal heat flux on the upside of the boundary is equal to the normal heat flux on the downside of the boundary.

4.2.3   Electrical – Thermal Model:

For the theoretical simulations, it is assumed that the heat from the resistive element is transferred through conduction and convection. The silicon substrate (<30 μm) is assumed to be in contact with an ideal heat sink with ambient temperature (293K). The heater design is optimized to have the largest change in temperature for a given input power. The idea here is that the largest temperature rise in the heater will cause the waveguide underneath to also have large temperature rise leading to efficient thermal tuning. The governing equation for the heat transfer is given by the conduction as it is the primary source of heat flow in the system. In FEMLAB, an appropriate electrical-thermal heater modeling is given by "Thin conductive shell and heat transfer applications", which uses the basic governing equations of the heat transfer from the heater to the substrate. The total input power (electrical) for a resistive heater of resistance 'R' and applied voltage 'V' is given by,

$$P = IV = \frac{V^2}{R} \tag{4.6}$$

The nominal resistance for a given heater at room temperature can be calculated from the geometry and the basic material properties.

$$R = \rho \frac{L}{A} \tag{4.7}$$

where ρ is the resistivity of the material, L is the length, and A is the cross-section area of the heater.

In the electrical-thermal model, an important assumption is made according to which, all the electrical energy is utilized to heat the resistor as joule heating. The governing equation for the electrical-thermal simulations in FEMLAB relates the heat flux as the joule heating due to applied voltage.

$$heat\_flux = \frac{Power}{Area} = \left(\frac{V^2}{R}\right)\frac{1}{A} \tag{4.8}$$

The total heat flux into the system is given by the gradient of the applied voltage:

$$q_o = d_s\sigma(\nabla_t V)^2 \tag{4.9}$$

where d_s is the thickness of the heater [m], σ is the electrical conductivity [S/m], subscript t in the gradient means tangential gradient, and V is the electrical potential [V].

The resulting heat transfer equation for the heater is given by:

$$-\hat{n}.(-\xi \nabla T) = q_o + h(T_{inf} - T) - \nabla_t.(-d_s\xi_s\nabla_t V) \tag{4.10}$$

According to the equation, the total heat flux is dissipated from the sample due to conduction and convection. The last term on the right hand side represents the additional heat flux due to the thin conducting layer of the heater and ζ_s is the thermal conductivity in the layer.

Some of the key assumptions for FEMLAB simulations are:

- Steady state (DC simulation): All the theoretical values for the heater designs are considered to be steady state.

- The heater is modeled as a thin conducting layer to use the appropriate application module. The heaters are 100 nm thick and can be considered thin compared to the cladding (1.5 μm) and waveguide's thickness (400 nm). Since the heater material is a metal (Titanium), it is a good electrical conducting layer ($\sigma = 1.3*10^6$ S/m).

- For most materials, the resistance varies with respect to the temperature. In the theoretical modeling, the resistance of the heater is kept constant.

- Heat flux due to joule heating is specified as the boundary condition at the surface of the heater.

- Heat is dissipated to the surrounding air by convection; most of the heat flows towards the substrate via conduction; and sidewalls have symmetry for boundary condition (Figure 4-1).

- Natural convection is assumed between air and the heater surface on the top, as there is no forced air flow in the system. Heat transfer coefficient is h = 5 W/m^{2}K [2].

For the thermal tuning of the ring resonators, the heaters can be fabricated on top of the rings as well as on the same level of the resonator. For EPIC, the heaters are fabricated on top of the ring resonator with 2 μm of over-cladding in between to ensure good optical confinement. The optimized ring dimensions for high intrinsic Q (>50,000) are 10 μm center radius and 400 nm thickness.

The filter bank is fabricated with various layers, namely the substrate, the cladding and the core. Theoretically we can predict the temperature of the rings by knowing the composition of the

device, the total input electrical power and the boundary conditions. Using FEMLAB, the pattern of heat flow is predicted for various heater designs, which gives an insight to the temperature as a function of position. Based on the thermal resistance and the total thermal power, heater designs are optimized for the highest power efficiency.

4.2.4 Thermal Impedance:

Thermal impedance is the measure of thermal resistance of a system, and gives an insight to the heat flow and barriers to heat transfer from high temperature to lower temperature. Thermal impedance (Z_T) can be taken as the amount of change in temperature (ΔT) due to certain input power (P).

$$\Delta T = Z_T P \tag{4.11}$$

A simple one-dimensional heat flow can give a rough estimate of the thermal impedance of the system (Figure 4-2a),

$$Z_T = \frac{d}{\xi A} \tag{4.12}$$

In the given equation, d is the distance of the heat source from the heat sink, A is the area and ξ is the thermal conductivity of the material separating the source from the ideal sink. A finite disk model as shown in Figure 4-2(b) can be used as a rough three-dimensional estimate for the thermal impedance of the system with the heater as a disk on top of the half space. In this case, the thermal impedance is give by:

$$Z_T = \frac{1}{2s\xi} \tag{4.13}$$
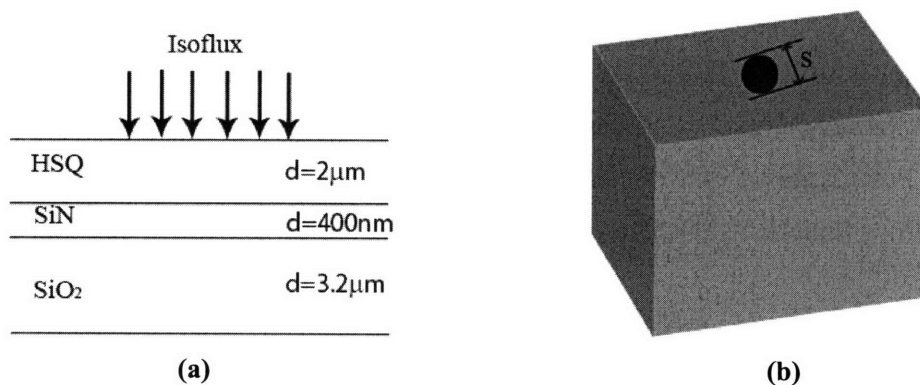
's' is the diameter of the disk.

Figure 4-2: Thermal impedance modeled for 1-dimension and 3-dimensional geometries.

In case of a ring resonator filter, the thermal tuning can be utilized to obtain a large tuning range or high power efficiency tuning. For applications such as reconfigurable optical add-drop multiplexers (R-OADM), large tuning range is necessary. For a large tuning range, the goal is to get the waveguide temperature as high as possible, i.e. close to the heater temperature. Larger area heater as shown in Figure 4-3(a) gives nearly one dimensional heat flow towards the substrate, and the average change in temperature of the waveguide is larger compared to the heater in Figure 4-3(b). For comparison purposes, the temperature of both the heaters is this simulation is taken to be 100°C. The amount of power required to raise the temperature of the heater to 100°C is different for both cases. Less than 50% of the input power of the large heater can bring the temperature of the smaller heater to the equal temperature value. Thus the second heater is better in terms of power consumption. However, since the average waveguide temperature rise is less for the smaller heater, the total tuning range is smaller. If similar tuning range is required from the second heater, i.e. the average waveguide temperature rise has to be 26°C, the amount of power required is about 0.13 mW. The tuning power is still less than the larger heater. However, the downside of the small heater design is that the temperature of the heater gets very high even with relatively low power, mostly due to large current density. With 0.13 mW, the temperature of the heater is 175°C. The heater temperature cannot be increased indefinitely. The problems of electromigration and oxidation will be prominent at higher temperature. Electromigration has been seen in the experiments which is described later in the chapter.
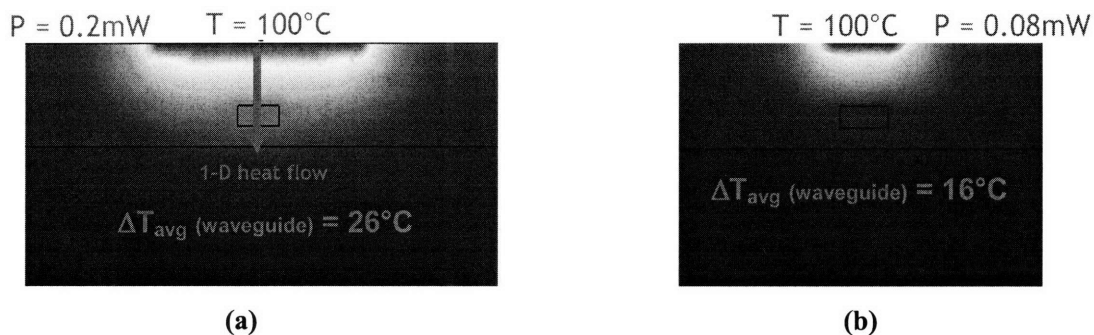
Figure 4-3: (a) 1-D heat flow for larger thermal tuning range, (b) heater with higher thermal impedance for power efficient tuning.

Thus, for large tuning range, one would focus on designing heaters that give nearly 1-D heat flow such that the ring temperature is very close to the heater temperature. However, that is not the

case for power efficient design. Thermal impedance is the key parameter for optimization. Higher thermal impedance means larger change in waveguide temperature due to relatively smaller input power, which directly makes the heaters power efficient. Thus, heaters with larger thermal impedance are desired for the tuning purposes for EPIC.

4.3   Materials & Design Curves:

One of the important aspects of designing a heater for thermal tuning of the ring resonator is the selection of the heater material. For the theoretical simulations, various materials were used. However, fabrication ease also has to be taken into consideration. At the beginning of the project, design curves were generated to optimize the material choices.

4.3.1   Heater Material Selection:

All the materials for the ring resonator are chosen to be "CMOS compatible", such that the present IC fabrication technology can be utilized. For EPIC, silicon-rich silicon nitride (SiN) rings are fabricated on silicon substrate with 3 μm of silicon dioxide as undercladding for mode confinement and low loss. 2 μm of hydrogen silsesquioxane (HSQ) is used for over-cladding. The titanium heaters are designed to sit over the rings for thermal tuning. Figure 4-4 shows the cross section and the top view of the ring layout for the second-order filter.

Figure 4-4: Basic layout of the second-order filter (a) cross-section (b) top view.

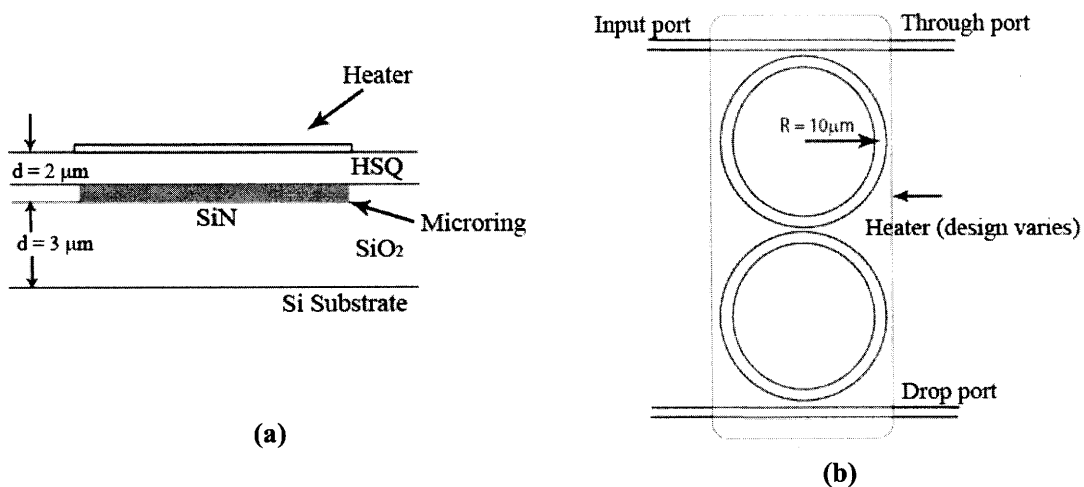Various materials were studied for making the heaters. Poly-silicon, amorphous silicon, chromium alloy and titanium were studied in detail as all of these materials are compatible with silicon processing and could be potentially used to make heaters. Various properties of the materials were studied. The thermal expansion coefficient of the heater has to match well with the cladding material, such that the stress due to thermal mismatch is minimum at the interface. Silicon dioxide's thermal expansion coefficient is 5×10^{-4}/°C. The material with larger temperature coefficient is desired so that a small change in temperature can give large resistance change in the heater for better temperature sensing purposes. Similarly, the material with a large thermal conductivity is preferred for efficient heat flow from the heater to the cladding. Poly silicon is compatible with high temperature processing with silicon dioxide, and has been used as heaters for thermal tuning of resonators [3]. However, compared to metals, the poly silicon used in Ref. [3] has a smaller resistive temperature coefficient (9.5×10^{-4}/°C). Also, the temperature coefficient of poly Si is highly dependent on the doping level and could be negligible in some cases. Chromium metal has been used most frequently as heater and thermistor material for tuning applications [4]. Due to the fabrication ease, titanium metal is chosen as the resistive heater. A thin layer (10nm) of gold is put on top of the metal layer to prevent oxidation. The measured temperature coefficient ($0.0012\pm4\%$) for titanium is less than the cited values. It has been reported that the temperature coefficient for titanium films are highly dependent on the processing [5]. The impurities during the deposition can give various temperature coefficients, and the values might also be different due to the gold layer at the top of the heater.

Material	Thermal conductivity (ξ) [W/m K]	Electrical conductivity (σ) [S/m]	Temperature coeff. [1/K]	Thermal expansion coeff. [1/K]
Chromium alloy	93.9	8×10^6	0.0028	4.9×10^{-6}
Titanium	21.9	2.38×10^6	0.0020 - 0.0038	8.6×10^{-6}
Poly Silicon*	125	Highly dopant dependent	Highly dopant dependent	$\sim 9.4 \times 10^{-6}$
Amorphous silicon*	1.8	-	-	$\sim 2 \times 10^{-6}$
Gold	318	4.5×10^7	0.0037	12.4×10^{-6}

Table 4-1: Summary of material properties for resistive heaters. (* Properties of semiconductors depends on doping and impurities).

4.3.2 Temperature Control Sensitivity:

At the beginning of the project, design curves were generated to find the sensitivity of the temperature control needed for the devices. As an initial step for the design problem, various criteria were looked into that could be optimized for the sensitivity of the temperature control of the thermal tuning of the resonators. The variable in the design curve shown in Figure 4-5 is the cladding material which has different thermo-optic coefficients. As mentioned in Chapter 1, the system requirement for the tuning of the rings is that the total tuning power efficiency has to be less than 60 μW/GHz per channel, and the resonant frequency has to be controlled within 100 MHz. According to the design curve, if polymers such as PMMA (with negative thermo-optic coefficient) are used for the cladding around the core waveguide, the power dissipation is higher. However, the temperature control is much relaxed to achieve the stability of 100 MHz. For polymers, the change in refractive index with temperature is mostly due to density variation [4]. For polymers such at PMMA, the density decreases with increase in temperature [6]. The increase in volume due to relatively higher thermal expansion coefficient (70 x 10^{-6} /°C), leads to decrease in material density [7, 8] which causes the refractive index to go down; thus most polymers have negative thermo-optic coefficient. If positive thermo-optic coefficient materials such as SiO_2 are used, power dissipation is much lower, however much more precise temperature control is needed for the desired stability in frequency. From the following design curve, SiO_2 is the optimum choice for the cladding material as the power dissipation is within the requirement and the temperature fluctuation can be tolerated within 30 mK for stable center frequency.
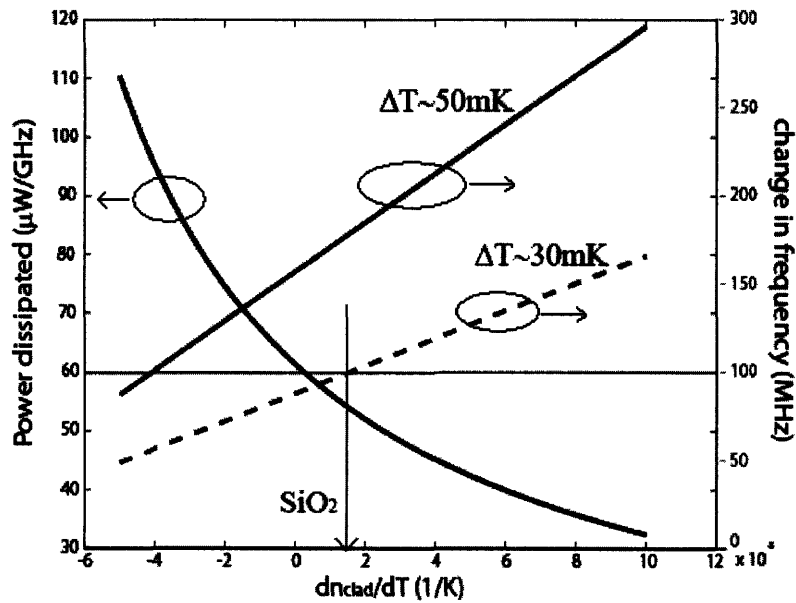
Figure 4-5: Design curves for different cladding (lower and upper) materials.

The cladding material is also selected by the index ratio between the core and the cladding. To confine the mode in the core and decrease the loss, high-index-contrast (HIC) system is required. Silicon dioxide (SiO_2) provides high index contrast with silicon or silicon nitride waveguide and is also well suited for low power dissipation tuning. HSQ has comparable properties as silica with refractive index of ~1.4. The material has low thermal conductivity resulting in smaller thermal cross-talk (ξ = 0.4-1 W/m K) compared to the traditional silica over-cladding. Thus, HSQ is used as the over-cladding material for the waveguide. Also, HSQ has a good gap-filling quality that is necessary for the critical gap between the bus waveguide and the ring which is about 500 nm.

4.3.3 Over-cladding Thickness:

Reducing the thickness of the over cladding helps as the temperature of the waveguide can be increased with smaller heater powers. However, if the metal is too close to the core of the waveguide the optical loss increases. Figure 4-6 shows a plot which illustrates that as the thickness of the cladding is decreased, the power efficiency increases. With 2 μm thick over-cladding, the optical loss is minimal and the power consumption is well within the requirement.
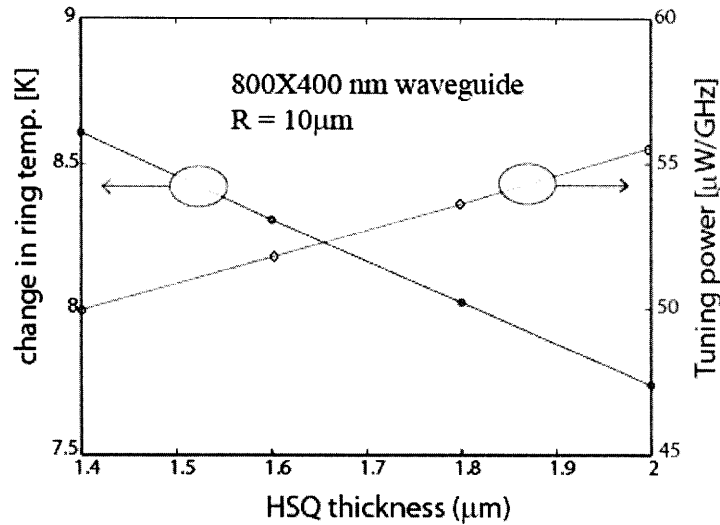
Figure 4-6: Dependence of tuning power on over-cladding thickness.

4.4 Theoretical Finite Element Simulations:

Using FEMLAB, various heater designs were developed and studied. Their power consumption and thermal impedance were the main criteria for comparison and optimization. Among the designs, three main heaters are described below.

4.4.1 Circular Heater:

These are the preliminary heater designs. Each ring is allocated its own heater on top of the over-cladding. For thermal tuning of a second-order filter, the voltage is applied to both the heaters. The heaters are designed such that they cover the entire ring structure. The width of the heater is approximately 2.5 times the width of the ring, and the heater covers the largest surface area compared to all the designs. Due to greater heat spreading over the lateral directions, this design is the least efficient of all the other designs. The heaters have comparatively lower thermal impedance due to larger area. Figure 4-7 shows the thermal simulation for a three channel second-order filter bank with the heaters on top of the two filters at the edges.
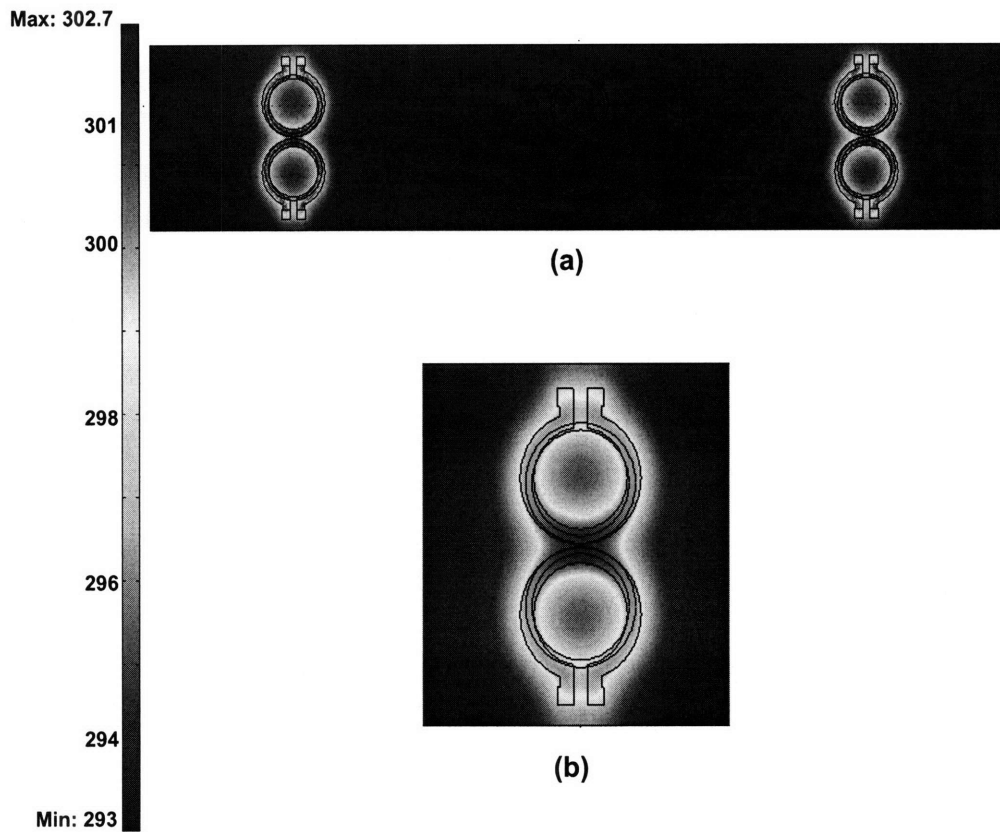
Figure 4-7: (a) Circular heaters (b) Thermal profile at the waveguide level.

Using the material property of Titanium (resistivity = 7.83 x 10^{-7} Ω m) and geometrical dimensions, the electrical resistance of a single titanium heater is roughly calculated to be 300 Ω. With the applied voltage of 0.5 V, the total input electrical power for a single heater should be about 0.83 mW. In the simulations, the total electrical power is the integral of the total heat flux (W/m^2) across the resistive heater which is 0.77 mW. For the theoretical power calculation of 0.83 mW, the resistance is estimated by taking the length of the heater to be the circumference of the circle with radius 10 μm, whereas the simulated heaters had the leads for the contact as seem in the figure above. For the given input electrical power, the average temperature rise of a single ring is 5.2 K. In case of tuning two rings as in the second-order filter, twice the input power is needed to raise the temperature of the rings. The total thermal impedance of the system for a second order filter is about 3400 K/W. The required tuning power per filter for SiN ring is 82 μW/GHz (~ 12.7 GHz/mW).

In micro-scale systems such as EPIC or UNIC, one of the important thing under consideration is the thermal cross-talk between the rings and the adjacent heaters. The amount of thermal disturbance due to an adjacent heater can have a severe and unwanted effect on the filter and its resonance frequency. For the cross-talk simulations, the channels are kept 100 μm apart, and the worst case scenario is studied, where the middle filter is not tuned thermally but the adjacent heaters are turned on (as shown in Figure 4-7 a). The change in temperature of the middle rings due to two adjacent heaters give the cross-talk measure for the device. The cross-talk between the adjacent channels is 1.3 GHz/W which is very small compared to the thermal tuning.
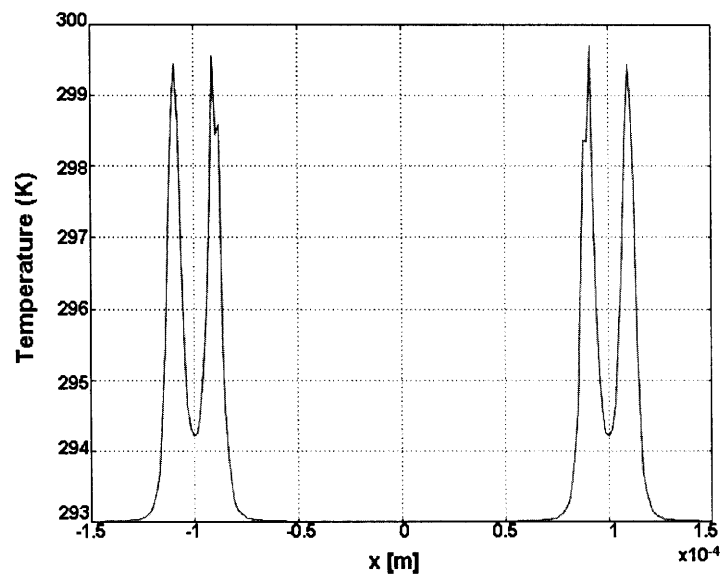
Figure 4-8: Temperature profile across the cross-section of the three filters.

Figure 4-8 shows the temperature profile of the filters along the cross-section. It can be seen that the maximum temperature rise is underneath the heaters, and the cross-talk is small as the temperature rise of the rings in the middle is negligible.

4.4.2 S-shaped Heater:

Another heater design is the S-shaped heater or the snake heater. In this design, a single thin resistive element is used to heat a second-order filter. With the applied voltage, the Joule heating causes the temperature of the rings to increase. The main disadvantage of the design is the unnecessary heating at the center of the filter where hotspots are created as seen in the figure below. As mentioned in the theory of heat transfer, the heat flow is in the direction of lower

temperature. With this heater design, the heat flow in the lateral direction is somewhat checked by the adjacent sides of the heater as the energy flow is towards lower temperature. The heater also has smaller surface area compared to the two circular heaters, which leads to higher thermal impedance. Thus, this heater has better power efficiency for thermal tuning.
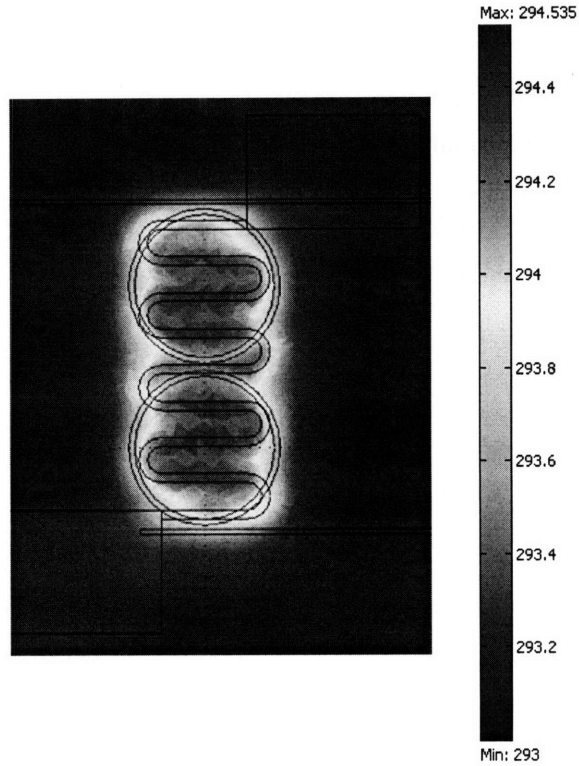
Figure 4-9: S-shaped heater design (temperature profile at the waveguide level).

According to the geometry, the heater resistance is 670 Ω. With the input power of 0.21 mW, the average temperature rise of a ring is 0.82 K. Thus, the thermal impedance of the system is more than 3900 K/W. The tuning power for this heater is 72 μW/GHz (~ 14 GHz/mW). For cross-talk simulation, the thermal effects of the adjacent heaters were studied on the middle ring. The cross-talk is very low within the range of 0.21 MHz/W. Figures 4-10 and 4-11 show the thermal simulations of the heater with cross-talk measurement. The temperature profile shows that there is comparatively no temperature change at the middle rings due to two adjacent heaters, indicating very low cross-talk when the adjacent channels are 100 μm apart.
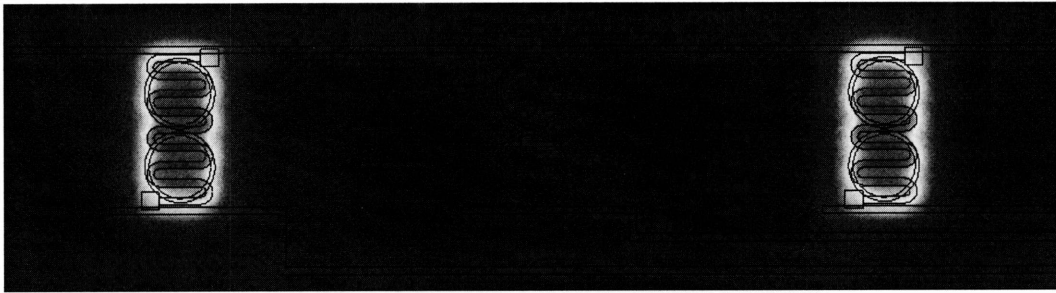
Figure 4-10: Thermal cross-talk simulations for adjacent heaters.
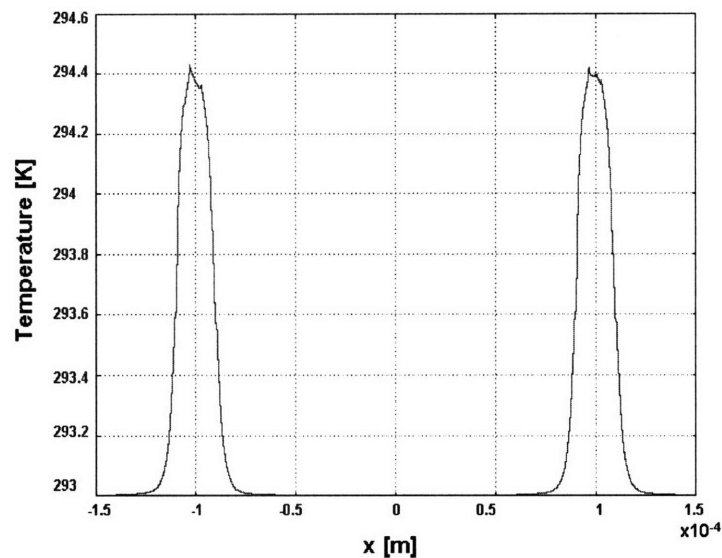
Figure 4-11: Temperature profile across the cross-section of the three filters.

4.4.3 Horse-shoe Heater:

The best power efficient heater design (Figure 4-12) is the horse-shoe shaped heater. At the first glance, these heaters look like the regular circular heaters discussed earlier. However, the design is more power efficient than both the previous discussed heaters as the surface area is optimized to heat most of the ring and create no hotspot. The heaters are made up of thinner wires which help in decreasing the total surface area. As mentioned earlier, the most efficient heater design is the one with the maximum thermal impedance. In case of the system with large thermal impedance, huge temperature rise can be obtained for the rings with minimal input electrical power.
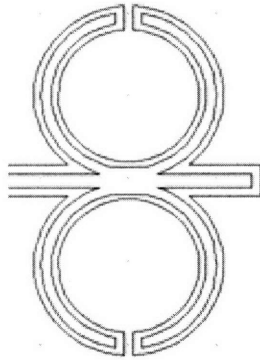
Figure 4-12: Best heater design with large thermal impedance.

Similar power and cross-talk simulations were done for this heater. The total resistance of the heater is about 2.3 KΩ. With the power consumption of 1.5 mW, the average temperature rise of the ring filter is 6.7 K. Thus, giving the thermal impedance of 4800 K/W. The tuning power consumption for this heater is 60 µW/GHz (~ 17 GHz/mW) and the cross-talk is minimal at 1.6 GHz/W.
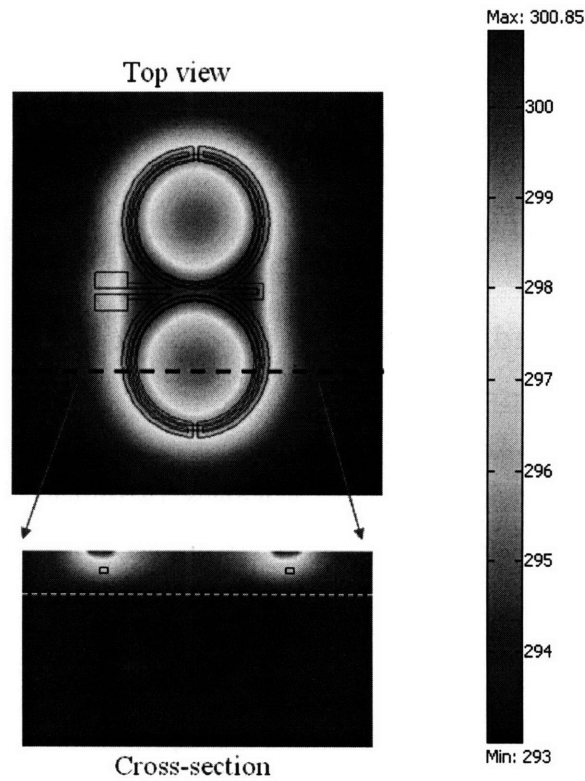
Figure 4-13: Thermal profile of the heater with cross-section temperature profile.

Figure 4-13 shows the thermal simulation of the heater with cross-section temperature profile. The cross-section shows the temperature distribution from the heater to the substrate with the rings in between. Heat flow across the cross-section is not one dimensional towards the substrate as would be required if the application was for large tuning range. The cross-talk is tolerable between the adjacent filters that are separated by 100 μm.

The following plot summarizes the three heater designs and the comparison factors: namely the thermal impedance and the power dissipation for tuning.
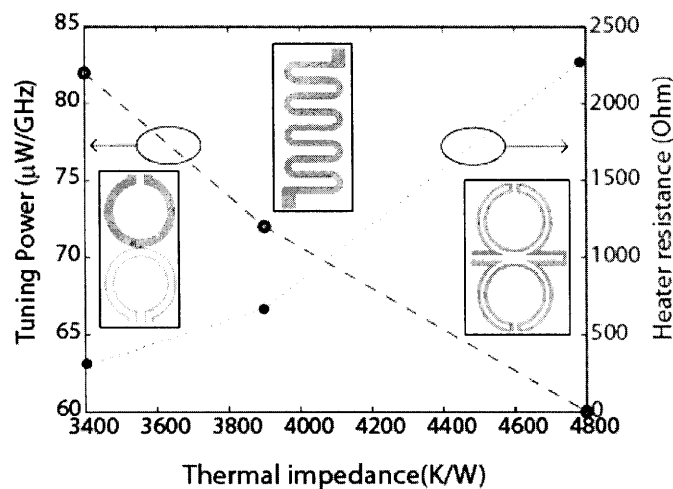
Figure 4-14: Heater designs with different thermal impedance and tuning power.

4.5   Experiments and Results:

The validation of the FEMLAB simulation is done by measuring the temperature of the heater and comparing the thermal impedance of different designs. Two different methods can be utilized to obtain the temperature of the heater: 3-ω method and thermoreflectance, which are described in this section.

4.5.1   3-ω Method:

For accurate measurement of the thermal impedance, precise temperature measurement of the heater is required. 3-ω is a popular technique to measure the temperature and thermal conductivity of thin films [9-12]. In the 3-ω method, an applied current of ω frequency across a

resistive element causes the resistance and the temperature of the sample to change with 2ω frequency. The voltage across the resistor has higher frequency component, namely the 3ω component which has the information about the temperature of the sample. The temperature is related to the applied voltage and the 3ω frequency component as derived below.

The resistance of the heater is temperature dependent and varies with temperature coefficient 'α'. R_0 is the nominal resistance at room temperature.

$$R = R_0\left(1 + \alpha \Delta T\right) \tag{4.14}$$

The change in temperature of the device is due to Joule heating given by:

$$\Delta T \approx I^2 R_0 Z_T \tag{4.15}$$

where, Z_T is the thermal impedance of the device. The voltage measured across the sample is:

$$V = IR = I_0 \cos(\omega t) * R_0\left(1 + \alpha \Delta T\right) \tag{4.16}$$

$$V \approx I_0 \cos(\omega t) * R_0\left(1 + \alpha\left(I_0 \cos(\omega t)\right)^2 R_0 Z_T\right)$$

$$V \approx I_0 \cos(\omega t) * R_0\left(1 + \alpha\left(\frac{I_0^2}{2}\left(1 + \cos(2\omega t)\right)R_0 Z_T\right)\right)$$

$$V \approx \left(I_0 R_0 + \frac{\alpha I_0^3 R_0^2 Z_T}{2} + \frac{\alpha I_0^3 R_0^2 Z_T}{4}\right)\cos(\omega t) + \left(\frac{\alpha I_0^3 R_0^2 Z_T}{4}\right)\cos(3\omega t)$$

The measured voltage across the resistor has a 'ω' and a '3ω' component, and the measured temperature oscillation due to the sinusoidal signal is:

$$\Delta T \approx \frac{4}{\alpha}\frac{V_{3\omega}}{V_{\omega}} \tag{4.17}$$

A simple experiment was carried on a diffused silicon resistor (6.152J wafer) to show the working of the 3-ω process. This is a four-point measurement as shown in Figure 4-15, where the current is applied through two probes and the voltage is measured across the resistor.
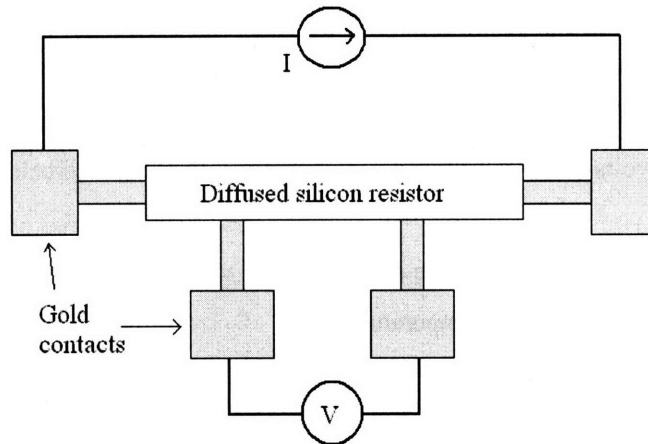
Figure 4-15: Simple schematic for 3-ω measurement.

As the total input power across the resistor is increased, the temperature of the device goes up as shown in the plot below. With this experiment, the smallest temperature change measured was 36 mK. The temperature coefficient for the diffused silicon was measured to be 1.8×10^{-3} K^{-1} using the four point resistance measurement at various temperatures.
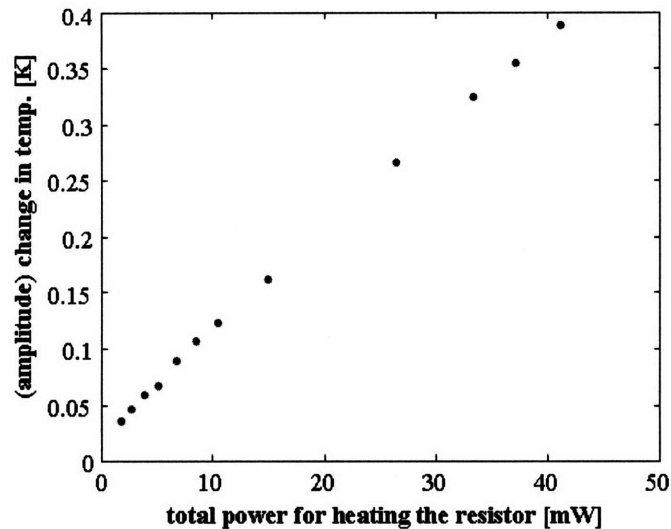
Figure 4-16: Change in temperature of the diffused resistor measured by 3-ω method.

The thermal conductivity measured from the resistor for the silicon layer is 1.38 W/cm K which is similar to the reported values of silicon of 1.3 W/cm K [13].

There are some basic assumptions made for the 3-ω method as discussed in ref. 9, and 10. These assumptions are for the geometry of the sample and the operating frequencies within which the

method gives accurate results. The thickness of the sample has to be greater than the thermal penetration depth, and the heater's width has to be small compared to both the thermal penetration and sample thickness. The thermal penetration depth (d) is related to the diffusivity (D) and operating frequency (ω) by:

$$\left|\frac{1}{q}\right| = \left|\left(\frac{D}{i2\omega}\right)^{1/2}\right| = d \qquad (4.18)$$

Figure 4-17 shows the thermal penetration depth for HSQ ($D = 4.7 \times 10^{-7}$ m^2/s) which is underneath the heater. For very thin layer of HSQ (<5 μm), operating frequencies near 10 Hz is sufficient to meet the geometrical conditions for 3-ω method.
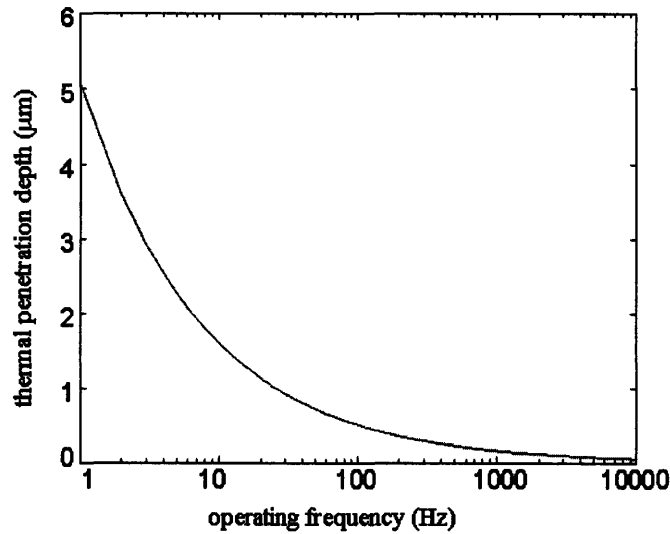
Figure 4-17: Thermal penetration depth for HSQ for various operating frequencies.

The temperature coefficient for the titanium heater was measured to be 0.0011 K^{-1} using the four-point resistance measurement at various temperatures as shown in the plot below.
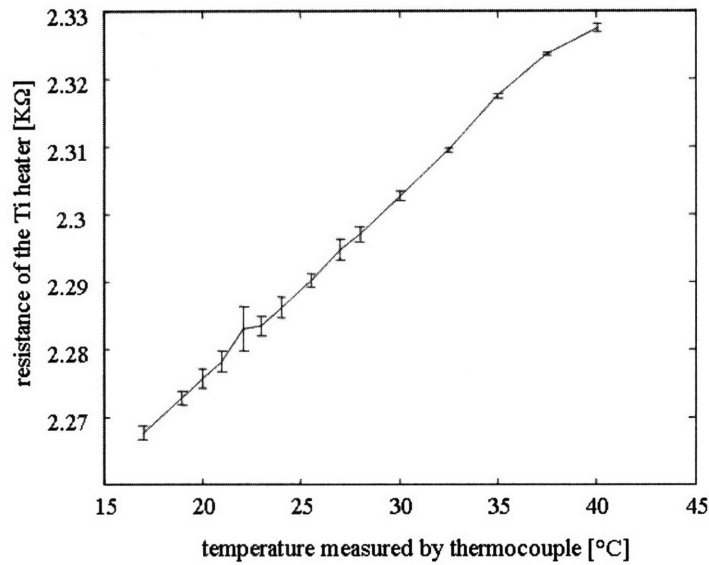
Figure 4-18: Temperature coefficient measurement for titanium heater.

The measurement was done on several heaters and the average temperature coefficient was found to be 0.0012 K^{-1}.

The final three heater designs (Figure 4-19: a,b,c) were experimentally characterized using 3-ω method. The heaters were fabricated by Charles W. Holzwarth at MIT.

| (a) | (b) | (c) |
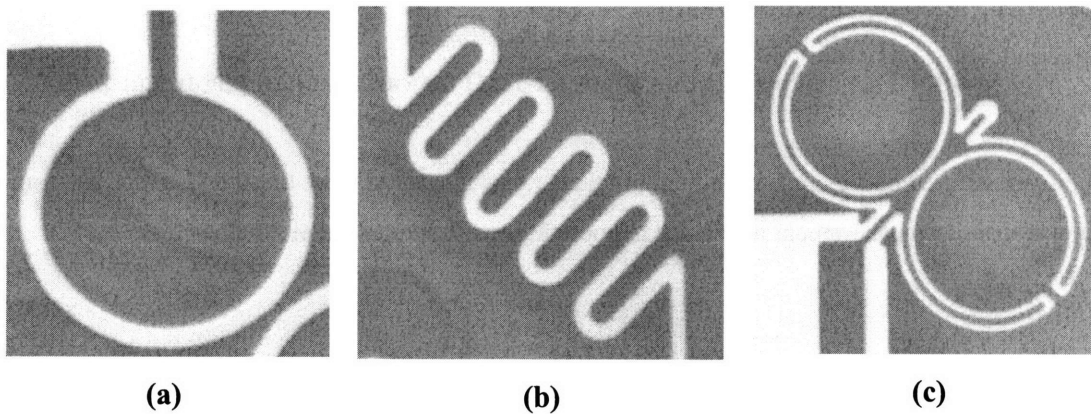
Figure 4-19: SEM pictures of the test heaters.

Systematic measurement shows the thermal impedances for the optimized heater to be 8807 K/W respectively. The FEMLAB simulations indicate the heater with similar geometrical shape and composition to have thermal impedance of 9180 K/W. To make the mesh size and simulation run-time reasonable, the substrate thickness was only assumed to be 30 μm for the theory as

compared to 500 μm in the real sample. The thermal conductivity for silicon (1.3 W/cm K) is two orders of magnitude smaller than that for silicon dioxide (125 W/cm K). Thus, using a thinner substrate in the simulation does not affect the impedance of the ring resonator by much. The thermal impedance was calculated as the slope of the power versus temperature as shown below.
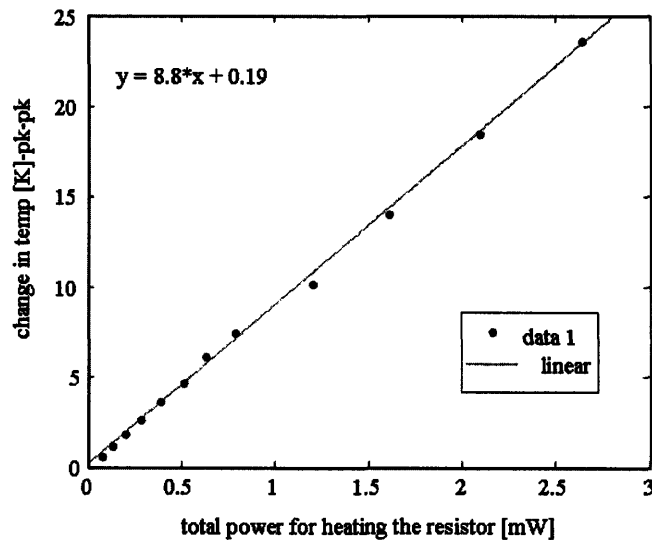
Figure 4-20: 3-ω measurement data for the optimized heater.

The thermal impedance calculated from the 3-ω measurement takes into account only the heater, and does not give the actual temperature of the buried ring waveguide. The actual temperature of the metal heater will always be larger than the buried ring. Thus, the thermal impedance of the heater is also larger than the thermal impedance seen by the ring that includes average temperature rise of the ring.

Figure 4-21 summarizes all the heaters that were studied theoretically and tested using the 3-ω method. The measured electrical resistances for the heaters are also close to the approximated value.
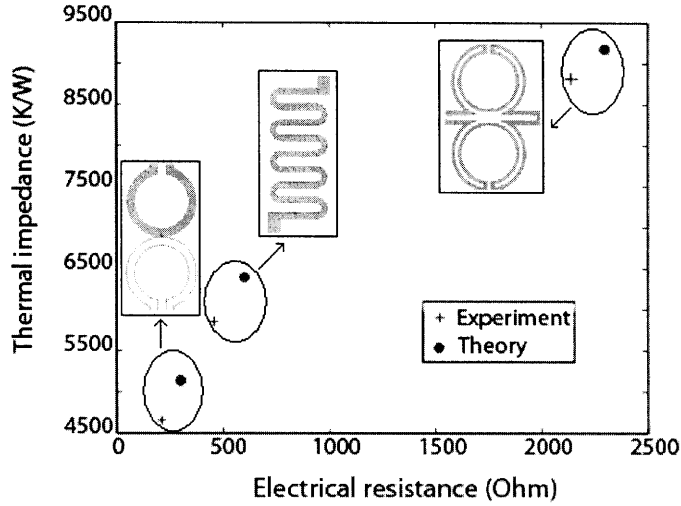
Figure 4-21: Experimental results for the thermal impedance of the heaters.

4.5.2 Thermoreflectance:

Various kinds of thermal imaging have been used to study the temperature profile of different devices. Thermoreflectance is a useful methodology to get precise temperature with very high spatial resolution [14-16]. Thermoreflectance microscopy measures the normalized change in surface reflectivity due to modulation of the surface temperature. The concept of thermoreflectance is based on the relation of change in reflectivity of the material and its temperature. The thermoreflectance coefficient relates the average amplitude of the change in temperature and reflectivity change ($\Delta\Re$) which is taken from a CCD camera.

$$\frac{\Delta\Re}{\Re} = \left(\frac{1}{\Re} \frac{\partial\Re}{\partial T} \right) \Delta T = \psi.\Delta T \tag{4.19}$$

$$\Delta T = \psi^{-1} \frac{\Delta\Re}{\Re} \tag{4.20}$$

The 4-bucket technique [14, 15] is used for thermoreflectance measurement which has the accuracy of the temperature scale to within 10 mK. The thermoreflectance calibration coefficient (Ψ) depends on the material, the illumination wavelength and the operating temperature. To demonstrate the process of thermoreflectance, preliminary measurements were done on a silicon waveguide from Lincoln laboratories. These waveguides are 1.8 μm long with the thickness of 100 nm. The calibration coefficient for silicon in the green light (512 nm) is 1.1 x 10^{-4} K^{-1} [15]. Using this information, we can deduce the temperature profile of the waveguide from the change in reflectivity as shown in Figure 4-22.

Optical Image   Thermoreflectance (ΔR/R)

(a)

ΔR/R
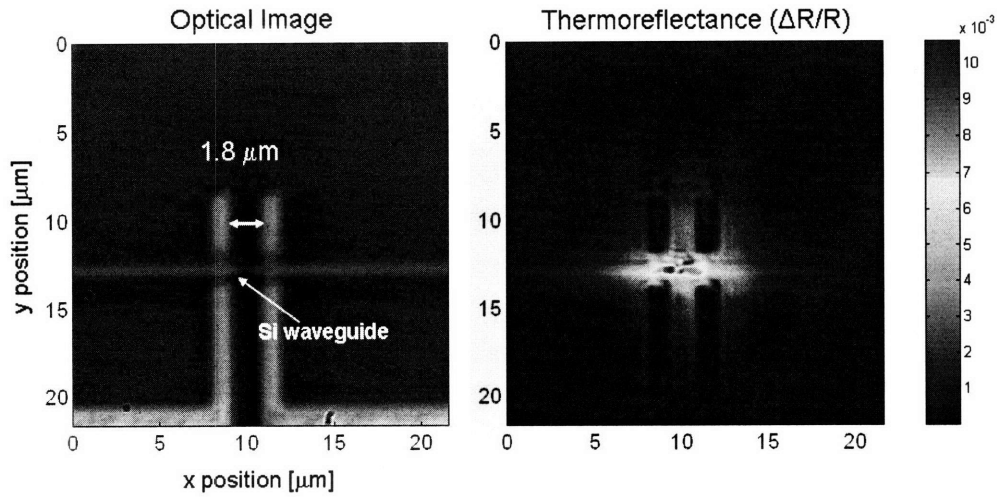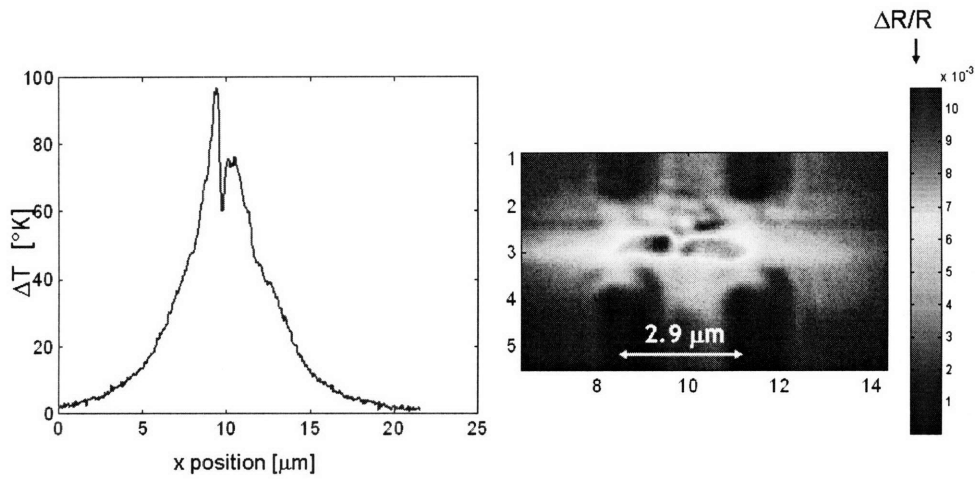
(b)

Figure 4-22: Thermoreflectance used to verify the temperature of a silicon waveguide of dimensions 1.8 μm structure (a) Optical and thermal image of the waveguide (b) temperature profile and change in reflectivity.

Thermoreflectance is used to get the temperature profile of the heater as shown in Figure 4-23. Titanium is covered with a thin 10 nm layer of gold to prevent oxidation. The skin depth for gold at the working wavelength of 467 nm (blue light) is about 3 nm, which is smaller than the thickness of gold layer.

$$skin\_depth(\delta) = \sqrt{\frac{2}{\omega \mu_r \mu_0 \sigma}} = 2.9nm \qquad (4.21)$$

Thus, thermoreflectance coefficient of gold in the blue light is used for temperature calibration (Ψ = 3.3 x 10^{-5} K^{-1}). The change in temperature measured by thermoreflectance is the average value for the amplitude of the temperature oscillation.
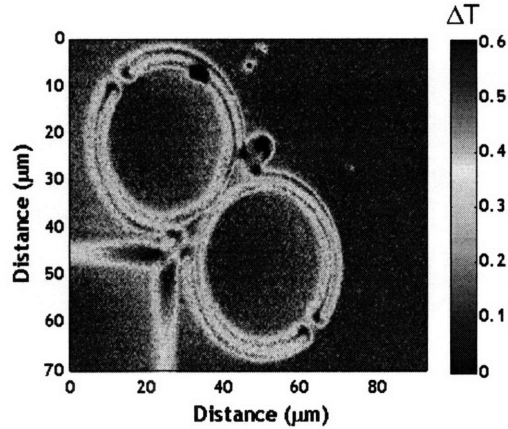
Figure 4-23: Temperature profile of the heater at input power of 0.15 mW.

For the input power of 0.14 mW, the temperature oscillation of the heater is ~ 1.2 K. Thus, the thermal impedance of the heater is 8500 K/W, which is similar to the value obtained from the 3-ω measurement. One of the disadvantages of the thermoreflectance measurement is the long iteration time, which actually helps the process by reducing the noise and makes it possible to measure very small signal. However, electromigration for the heater was seen as a pronounced effect due to running the current for long time (<15 hours). Electromigration [17-19] is the transport of material in a conductor caused by the momentum transfer between conducting electrons and diffusing material atoms. This phenomenon is very easily visible in narrow (sub-micron width) electrical wires. The width of the heater that is used in the experiment is in the order of 0.2 μm. Apart from large current density causing electromigration, the time for which the current is put across the resistor is also important. Black's Law [18] gives the median time of failure for a wire which depends on the current density. For a large current density, the time of failure due to electromigration is short, whereas for small currents electromigration might not occur during the lifetime of the device. Instantaneous electromigration was not observed for these heaters. However, for a few milli-watts of power, electromigration occurred when the experiment of thermoreflectance was carried for a day. The microscopic picture of a heater destroyed by electromigration is shown in Figure 4-24.
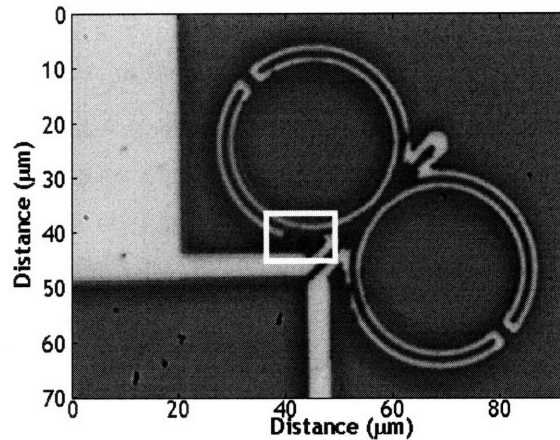
Figure 4-24: Heater destroyed by electromigration.

4.5.3   Thermal Tuning with On-chip Heater:

The final set of experimental data for thermal tuning was obtained by heating the ring waveguides using the on-chip heater. The optical measurement was taken at the drop port for each input power. Figure 4-25 shows the optical spectrum at the drop port of the second-order filter. At higher power, the spectrum is broad and the frequency mismatch between the two rings of a filter is very distinct, as seen by the two peaks. This can be well explained with the heater misalignment (Figure 4-26) during fabrication which causes one ring to heat more than the another.
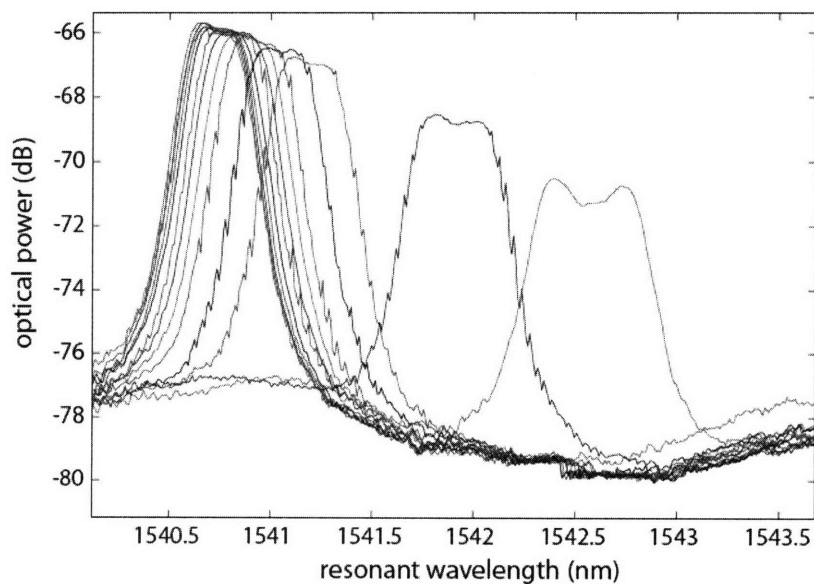
Figure 4-25: Optical spectrum showing shift in resonance as the heater power is increased.

The misalignment during the fabrication leads to non-uniform heating of the ring. From the theoretical simulation using FEMLAB, if the heater is placed 5 μm diagonally away from the exact position of the rings, the difference in the thermal impedance of the ring is more than 25% at only 3570 K/W, as compared to the optimized value of 4800 K/W. The filters also had the frequency mismatch between the two rings of the second-order filter from the initial state which got worst when the heater power was increased in this non-uniform heating as shown from the experimental data.
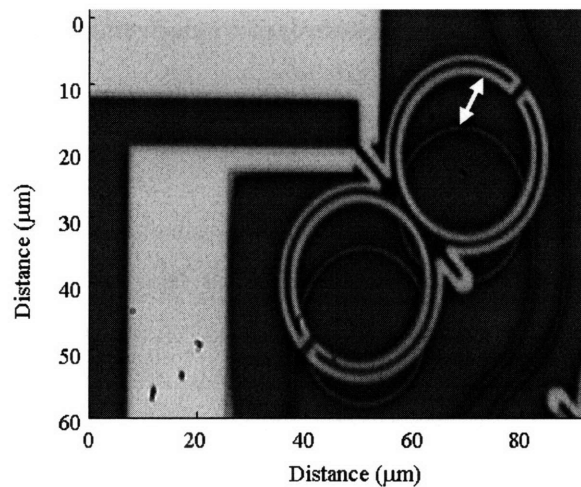
Figure 4-26: Misalignment of the heater on top of the ring waveguide.

Figure 4-26 shows the plot for electrical power versus resonant wavelength according to which the filters are tuned for more than a single channel spacing with the total power efficiency of 80 μW/GHz.
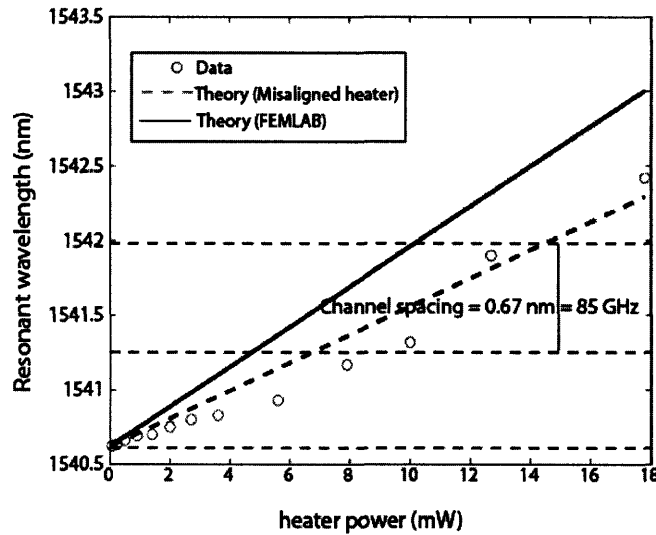
Figure 4-27: Thermal tuning efficiency for the optimized heater.

When linear dependency is assumed, the efficiency for thermal tuning is 12.3 GHz/mW (~ 80 μW/GHz). The theoretical prediction with the optimized heater structure on top of the ring filter is 17 GHz/mW (~ 60 μW/GHz). The discrepancy is attributed to the misalignment of the heater, which brings the tuning power efficiency of the heater down to 13 GHz/mW, similar to the experimental results.

4.6   Summary:

The electrical characterization for the micro-heaters using both thermoreflectance and the 3-ω method show high spatial and temporal resolution needed for the accurate temperature measurement of the heaters. Relatively good agreement between the theoretical simulation and the measurements within the fabrication errors for the heaters indicate that the proposed optimized heaters will have low power dissipation. The optimized heater is fabricated and tested to verify the thermal impedance, and the thermal tuning is achieved for a second-order filter with on-chip heaters with power consumption of 80 μW/GHz for a second-order filter channel. The next step is to put a temperature feedback control along with the heater that will ensure the steady resonance frequency of the filter within 100 MHz. The negative feedback circuit used for this application and the experimental results for thermal stability are discussed in Chapter 5.

References:

1. L.C. Thomas, "Heat Transfer – Professional version", Capstone Publishing Corporation, 2nd Edition (1999).

2. "Heat Transfer Module – User's Guide", Comsol Multiphysics, version 3.3 (2006).

3. P. Heimale, P. Katila, J. Aarnio, A. Heinamaki, "Thermally tunable Integrated Optical Ring Resonator with Poly-Si Thermistor", Journal of Lightwave Technology, Vol. 14, No.10, Oct (1996).

4. Z. Zhang, P. Zhao, P. Lin, F. Sun, "Thermo-optic coefficients of polymers for optical waveguide applications", Elsevier, Polymer 47, pp. 4893-4896, (2006).

5. D. Gerstenberg, "Structure and Electrical Properties of Evaporated and Sputtered Titanium Films", Annalen der Physik, Vol. 466, No. 7-8, pp. 354-364 (1963).

6. S.B. Sane, T. Cagin, W.G. Knauss, W.A. Goddard III, "Molecular dynamics simulations to compute the bulk response of amorphous PMMA", Journal of Computer-Aided Materials Design, Vol. 8, No. 87-106, (2001).

7. M.B.J. Diemeer, J.J. Brons, E.S. Trommel, "Polymeric Optical Waveguide Switch Using the Thermooptic effect", Journal of Lightwave Technology, Vol.7, No. 3, pp. 449-53, March (1989).

8. A. Priyadarshi, L. Shimin, E.H. Wong, R. Rajoo, S.G. Mhaisalkar, V. Kripesh, "Refractive Indices Variation with Temperature and Humidity of Optical Adhesive", Journal of Electronic Materials, Vol. 34, No. 11, pp. 1378-84, (2005)

9. D.G. Cahill, "Thermal conductivity measurement from 30 to 750K: the 3ω method", Review of Scientific Instruments, Vol. 61, No. 2, Feb (1990).

10. D.G. Cahill, H.E. Fischer, T. Klitsner, E.T. Swartz, R.O. Pohi, "Thermal conductivity of thin films: Measurements and understanding", Journal of vacuum science and technology A, Vol. 7, No. 3, May/June (1989).

11. C. Dames, G. Chen, "1ω, 2ω, and 3ω methods for measurements of thermal properties", Review of Scientific Instruments. Vol. 76, (124902) (2005).

12. B.W. Olson, S. Graham, K. Chen, "A practical extension of the 3ω method to multilayer structures", Review of Scientific Instruments, Vol. 76, (053901) (2005).

13. H.R. Shanks, P.D. Maycock, P.H. Sidles, G.C. Danielson, "Thermal Conductivity of Silicon from 300 to 1400 K", Physical Review, Vol. 130, No. 5, June (1963).

14. D. Luerβen, J. Hudgings, P. Mayer, R. Ram, "Nanoscale Thermoreflectance with 10mk Temperature Resolution using Stochastic Resonance", 21st IEEE SEMI-THERM Symposium, pp. 253-8 (2005).

15. P. Mayer, "High-density Thermoelectric power generation and Nanoscale Thermal Metrology", PhD Thesis, Massachusetts Institute of Technology, Cambridge, April (2007).

16. G. Guizzetti, L. Nosenzo, E. Reguzzoni, G. Samoggia, "Thermoreflectance spectra of diamond and zinc-blend semiconductors in the vacuum-ultraviolet region", Physical Review B, Vol. 9, No. 2, Jan (1974).

17. F.M. D'heurle, "Electromigration and Failure in Electronics: An Introduction", Proceedings of the IEEE, Vol. 59, No. 10, pp. 1409-18, Oct (1971).

18. J. Black, "Electromigration Failure Modes in Aluminum Metallization for Semiconductor Devices", Proceedings of the IEEE, Vol. 57, No. 9, pp. 1587-94, Sept (1969).

19. A.H. Verbruggen, "Fundamental questions in the theory of electromigration", IBM J. Res. Develop. Vol. 32, No. 1, Jan (1988).

CHAPTER 5

FEEDBACK TEMPERATURE CONTROLLER

5.1   Overview:

Thermal tuning is used for the post-fabrication trimming and stabilizing the resonant frequency of the microring filter. The heater is run by a temperature controller feedback circuit which helps in maintaining a steady temperature against the environmental temperature perturbation. The electronic circuit described in this chapter works on the principle of the Wheatstone bridge, where the circuit senses the change in the resistance of the heater induced by the change in its temperature. The voltage difference across the bridge passes as the error through a feedback control loop which sets appropriate voltage across the bridge to reduce the error. There is no direct non-invasive technique of measuring the temperature of the microrings. Thus, the circuit monitors the temperature of the heater by monitoring its resistance as a measure of the filter temperature. With FEMLAB simulations, the temperature of the rings can be obtained from knowing the heater temperature. Examples of commercial temperature controllers and previous related work are described in Section 5.2. The circuit is introduced in Section 5.3. The theoretical simulation for the circuit using SPICE is discussed in Section 5.4. The experimental procedure and results for the stability measurements using the circuit are shown in Section 5.5.

5.2   Previous Work:

Most commercial feedback temperature controllers have thermo-electric cooler (TEC) as the heating/cooling device and thermistors to monitor the temperature of the module for feedback purposes. Figure 5-1 shows two such modules from Analog Devices [1] and Electronic Wavelengths (PID-1500) [2] that can be used for precise temperature control. The block diagram in Figure 5-1(a) shows an optical module which has a TEC device, and a thermistor connected to the controller that sets the TEC temperature. The controller monitors and controls the output by reading the thermistor temperature for the feedback. Similarly, the PID-1500 has a resistive heater for heating the module and a thermistor connector for feedback.

(a)

(b)
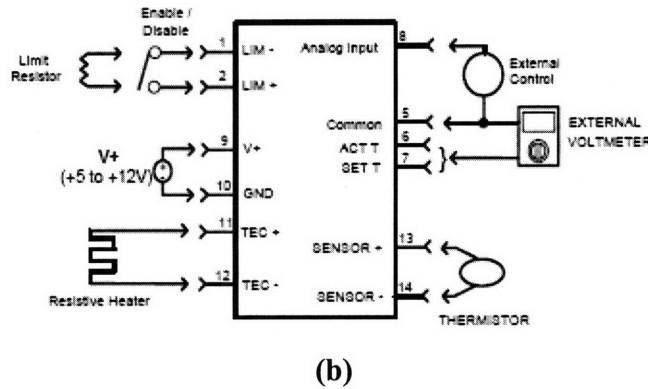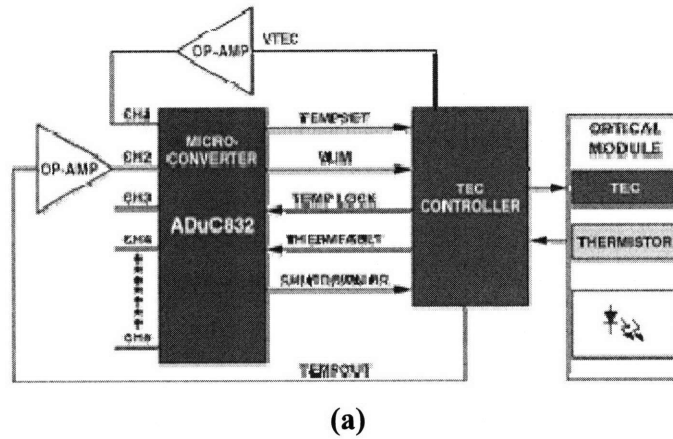
Figure 5-1: Temperature controller circuit models using TEC/resistive heaters and thermistors [1, 2].

The commercial TEC controllers as shown above are used widely for maintaining temperature within the precision of 0.01°C for laser diode and other optical modules. In a laser, the temperature precision is mostly needed for the wavelength stability at the output. For our purpose also, the wavelength stability at the output of the ring resonator is a requirement in order to reduce the error due to timing jitter during sampling. Due to the circuit design restriction, a single resistor cannot be used as both the heater and the sensor in the commercial controllers. The input sense current in the thermistor is only in the micro-amperes regime, which is not enough to drive the heater. One of the constraints for the on-chip integrated circuit is the chip area and the dimensions of the devices. For various reasons mentioned in Chapters 1-3, the photonic devices in the integrated chip have very small feature sizes (~1-2 μm). To minimize the total area usage on a chip, the proposed temperature controller uses a thin-film resistive element both as a heater and a temperature sensor, instead of using two different elements as needed in the commercial TEC controllers. Control feedback is utilized to regulate the temperature of the sample.

Thermal tuning is a widely used method for regulating the resonant frequency of a ring structure, and various techniques have been used in the past for monitoring and controlling the temperature of the ring resonator. One such example is illustrated in Figure 5-2, where a micro-control loop for the rings uses a resistive heater and a temperature sensor made from platinum wire [3]. The rings in this demonstration are 70-100μm large. A disadvantage of putting the sensor on the edge of the resonator is the possibility of inaccurate temperature reading due to thermal crosstalk.
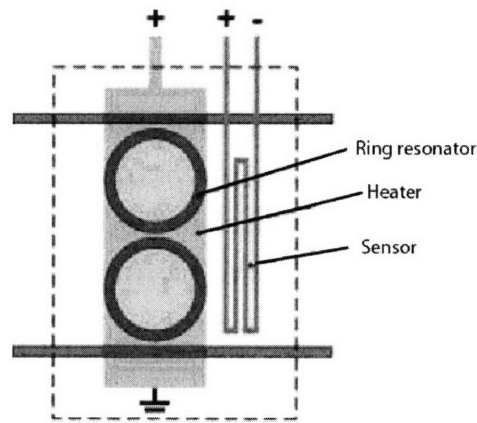
Figure 5-2: Micro-Control loop.

One of the earlier works [4] shows a poly-Si film as a heater and a temperature sensor for a large diameter (~ 4mm) ring resonator. Two bands of poly-Si are laid within the circumference of the ring as shown in Figure 5-3. One film is used as a heater, while the other is used to measure the temperature of the ring. Since the ring diameter was large, two resistors could be easily fit inside it. However, for EPIC, with 10 μm radius ring, the inner resistor would have been very small and the measurements would be affected by parasitic contact resistance.
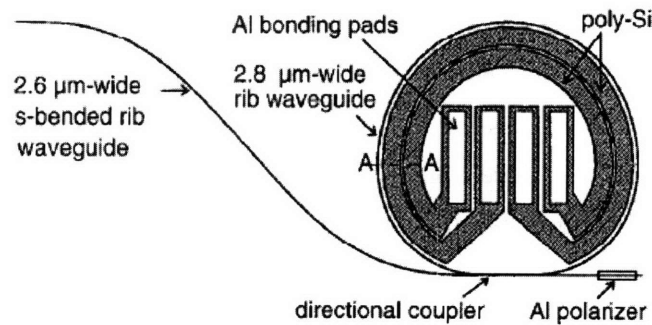
Figure 5-3: Poly-Silicon heater and temperature sensor for tuning a microring [Ref.4].

Reference 5 and 6 describe two circuits that demonstrate experiments where a single resistor is used as a heating element and as a temperature sensor. The key concept of these circuits is the Wheatstone bridge architecture. With these resistor bridge circuits, the observable temperature modulation is limited by the noise and the off-set voltage limitations of the operational amplifiers. Using the components as mentioned in the references, the temperature sensitivity is 75-90 mK. Even though, the same resistor is used as the heater and the thermistor, in both cases, switches are used to separate the heating and the measuring mode. The interchange between the two modes is facilitated by a switch which operates at a low frequency of 50 Hz [5]. In such circuits, the change in the resistance of the heater is used as the temperature measure. The resistance of the heater changes due to change in its temperature which is quantified by its temperature coefficient. Thus, metals with high temperature coefficient are beneficial for sensor applications. Accurate resistance measurement is given by the bridge circuit in which the unknown resistance, i.e. the heater, is compared with a known reference resistor. The reference resistor is equivalent to setting the reference temperature that we want the heaters to be at. In the circuits for ref. 5 and 6, the voltage across the heater and the reference resistor is measured to get the error which controls the power regulator and the amount of current flowing to the heater. The temperature controller circuit for this research also uses similar architecture of the Wheatstone bridge to measure the resistance change and appropriate temperature variation, and the feedback circuit controls the voltage across the bridge in order to minimize the errors.

5.3 Circuit Specification:

The following circuit (Figure 5-4) described in this chapter is used for the temperature stability of the ring resonator. The circuit is based on the resistance bridge structure where the change in the resistance of the heater is measured to indicate the change in temperature. The temperature controller is not an on-chip circuit in the EPIC project. In the Wheatstone bridge architecture, the heater is the unknown resistor and the other three resistors are assumed to be temperature independent. One of the resistors is a potentiometer which sets the resistance value for the heater. Once the bridge is balanced, if there is any temperature change in the ring/heater, the resistance of the heater changes according to its temperature coefficient. The error in the voltage between the set resistor and the heater is measured by an instrumentation amplifier (low noise – 0.28 μV_{pp}, low offset voltage – 15 μV) which passes through a feedback circuit to control the total input voltage to the bridge. If the heater resistance is smaller than the set value, the current flow increases through the heater which causes larger power dissipation and increase in temperature

102

due to joule heating, thus increasing the overall resistance to maintain the temperature. Similarly, if the heater resistance is higher than the set value, the current flow decreases causing decrease in the temperature rise due to joule heating, thus decreasing its resistance.
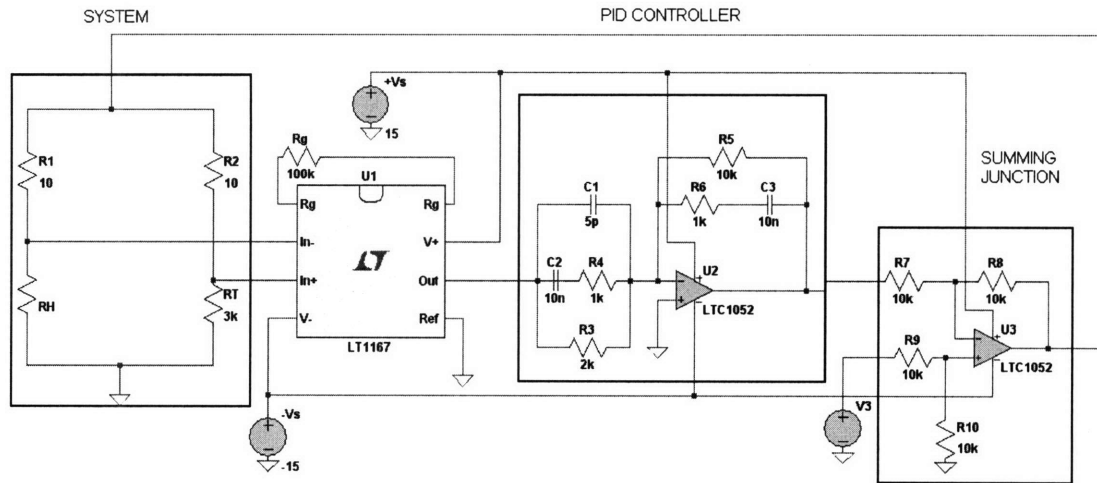
Figure 5-4: Temperature controller feedback circuit.

The feedback circuit tries to maintain the overall balance between the voltages of the two resistors such that the error in the voltage difference measured by the instrumentation amplifier is minimum. The feedback controls the total voltage across the bridge circuit. One of the widely used control feedback mechanism is the proportional-integral-derivative (PID) controller. A general schematic for a closed loop feedback system with a PID controller is shown in Figure 5-5.
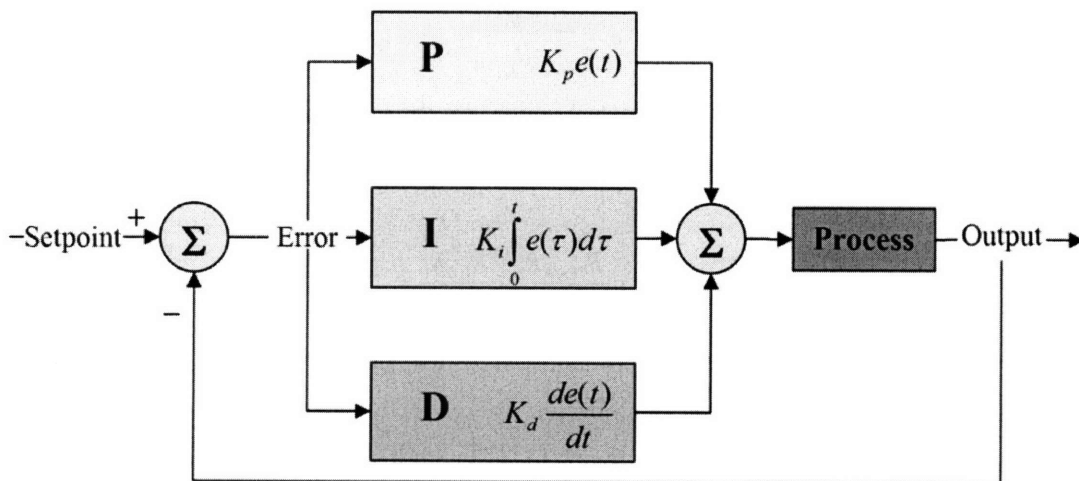
Figure 5-5: Feedback system using PID for stability.

The error signal is multiplied by a proportional gain (K_p) to reach a setpoint. The error is also integrated and multiplied by an integral gain (K_i) to accelerate reaching the setpoint and also eliminates any steady-state error due to the proportional gain. The derivative action slows down the rate of change for reaching the setpoint and thus helps decrease the overshoot. The PID controller used for the circuit is shown in Figure 5-4, and the details of the circuit are discussed in the next section along with the circuit simulations. Figure 5-6 shows the block diagram representation of the temperature controller.
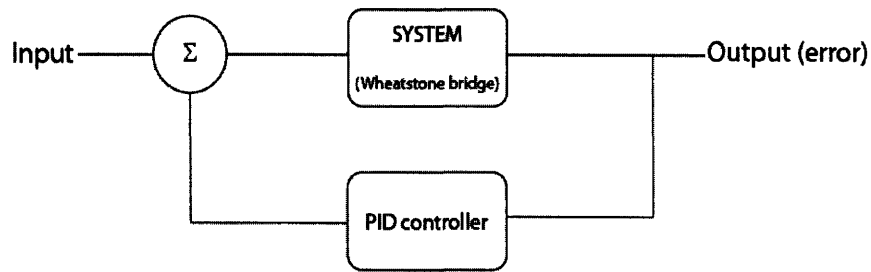
Figure 5-6: Temperature control feedback diagram.

The resistance of the heater varies with respect to the temperature according to:

$$R_H(T) = R_{H0} + R_{H0}\alpha\Delta T \tag{5.1}$$

R_{HO} is the nominal resistance of the heater at the room temperature and α is the temperature coefficient of the heater (For titanium/gold: $\alpha = 0.0012\text{K}^{-1}$). For a balanced bridge, the resistance of the heater is controlled by three other resistors in the bridge and is given by:

$$R_H = \frac{R_{TEMP}R_2}{R_1} \tag{5.2}$$

R_{TEMP} is a variable resistor (e.g. potentiometer) which sets the temperature of the heater by fixing the resistance. From equation 5.1 and 5.2, the change in temperature can be related to the resistors as:

$$\Delta T = \frac{R_{TEMP}R_2 - R_{H0}R_1}{R_{H0}\alpha R_1} \tag{5.3}$$

An instrumentation amplifier continuously adjusts the total voltage drop across the resistance bridge to maintain its two inputs at equilibrium. The error for the feedback is measured by a single resistor gain instrumentation amplifier (LT1167) with low noise. The theoretical limitation for the measurement is the thermal noise of the resistor, given by:

$$V_{noise} = \sqrt{4k_B TR\Delta f} \tag{5.4}$$

The nominal heater resistance is 2.4 KΩ at the room temperature (T = 293K). Thus, the theoretical thermal noise limit for the resistor is 6 nV/√Hz. The frequency of interest for the measurement is related to the time scale at which the thermal disturbances occur in the surrounding near the resonator. The temperature variations of the air around the device can be minimized by keeping it in an enclosed box and controlling the air convection. However, in an electronic chip, the larger temperature perturbation occurs due to heating of the entire chip. The studies done on the thermal management in an electronic device such as a microprocessor have shown the heat distribution across the chip [7, 8]. According to an experimental result of the temporal temperature variation for a working microprocessor, the average switching speed for the temperature variation is in the order of 1 ms [7]. At a measurement bandwidth of 1 kHz, the thermal noise due to the heater is in the order of 190 nV. For the balanced resistor bridge, the voltage error measured by the instrumentation amplifier is due to the resistance variation in the heater caused by the temperature perturbation. A change in the temperature of 30 mK for the heaters causes the resistance change of 82 mΩ. The equivalent voltage signal to be measured by an ideal amplifier with the gain of one is 2 μV. The current of 25 μA across the heater used to calculate the voltage signal of 2 μV causes self-heating with the temperature variation of less than 10 mK. The signal to noise ratio (SNR) for the measurement across the heater if limited by the thermal noise of the heater is:

$$SNR = 2\ \mu V\ /190\ nV = 10.52 \tag{5.5}$$

However, when using operational amplifiers and instrumentation amplifiers, the measurement is limited by the noise performances of the electronic components. A commercial simulation package-SPICE is used for the circuit simulation. To improve the SNR of the measurement, higher gain value can be chosen for the amplifier, but higher gain results in higher noise for the circuit as shown in the results of the simulations discussed in the next section.

5.4   SPICE Model:

In the feedback circuit, there are three main parts: the system (the Wheatstone bridge), the PID controller and the summing junction. First, the open-loop circuit analysis is done to show the operation of the Wheatstone bridge. The loop is closed with the feedback from the system using a PID controller. The noise analysis and the transient response are performed using SPICE models of the specific amplifiers.

The open-loop transfer function for the circuit only involves the Wheatstone bridge and the instrumentation amplifier (Figure 5-7). An idealized amplifier is assumed for the calculation of this transfer function with a gain ($g_{amplifier}$). The transfer function is the ratio of the output voltage of the instrumentation amplifier to the input voltage of the bridge and is given by:

$$K = \left(\frac{R_{TEMP}}{R_2 + R_{TEMP}} - \frac{R_H}{R_1 + R_H} \right) * g_{amplifier} \qquad (5.6)$$

$$\mathbf{V_{in}} \longrightarrow \boxed{K = \left(\frac{R_{TEMP}}{R_2 + R_{TEMP}} - \frac{R_H}{R_1 + R_H} \right) * g_{amplifier}} \longrightarrow \mathbf{V_{out}}$$
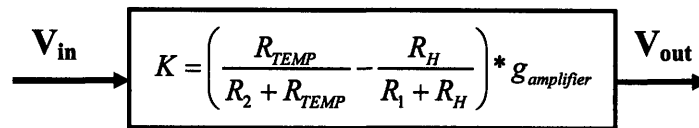
Figure 5-7: Temperature controller without feedback.

The circuit was modeled using the SPICE simulator. The net file for SPICE simulation is attached in Appendix A. The three amplifiers (LT1167: the instrumentation amplifier, and LTC1052: the operational amplifier for the PID compensation and the summing junction) used in the circuit are from the Linear Technology (LT) Inc., which allowed usage of the web-free version of the CAD III tool for the SPICE modeling provided by LT. The SPICE macro-models for all the amplifiers were available in the library of the program tool box. The CAD tool can be downloaded from ref. 9.

The noise analysis for an open loop circuit (Figure 5-8) shows that the limitation in the measurement is due to the instrumentation amplifier noise rather than the resistance in the circuit. The best commercially available instrumentation amplifier with low noise (0.28 μV_{p-p} -0.1Hz to 10Hz) is used for the circuit. As the gain of the amplifier is increased, the noise also increases, as shown in the plot below.
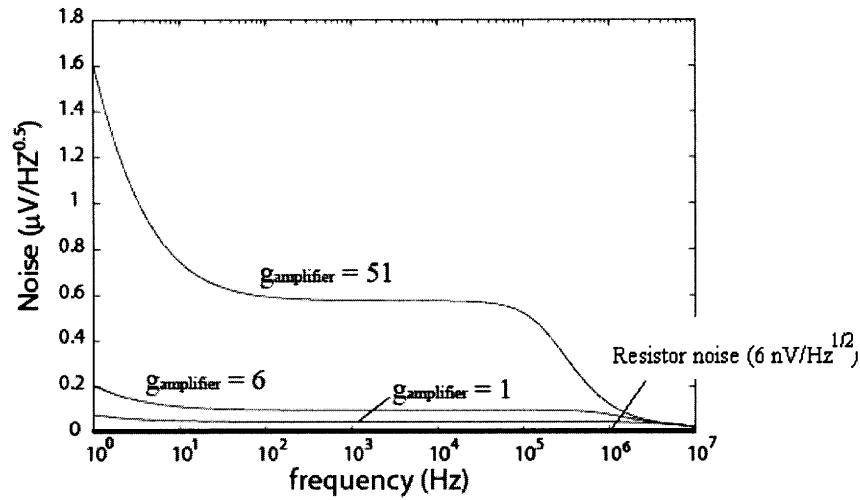
Figure 5-8: Noise analysis for the open-loop circuit.

With the amplifier gain of 51, the SNR for measuring 30 mK temperature variations is only 2 which sets the limitation for a precise measurement. Figure 5-9 shows the theoretical simulation for the error measured by the instrumentation amplifier for various input voltages. It matches well with the measured results.
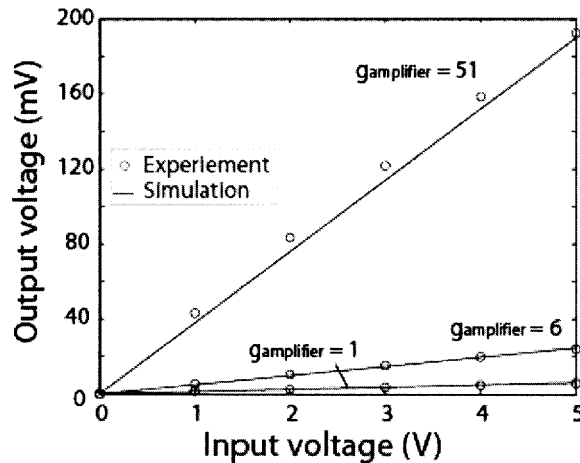
Figure 5-9: Various error voltages measured at different amplifier gains.

A PID controller is implemented at the feedback loop to ensure a stabilized output of the circuit. The transfer function for the closed-loop system with the feedback gain (G) is given by the Black's formula as:

$$\left| \frac{V_{out}}{V_{in}} \right| = \left(\frac{K(s)}{1 + K(s)G(s)} \right)$$

(5.7)

where, $G = \dfrac{Z_2}{Z_1}, Z_1 = \dfrac{R_3 R_4 C_2 s + R_3}{R_3 R_4 C_1 C_2 s^2 + (R_4 C_2 + R_3 C_1 + R_3 C_2)s + 1}, Z_1 = \dfrac{R_5 R_6 C_3 s + R_5}{(R_6 + R_5)C_3 s + 1}$.
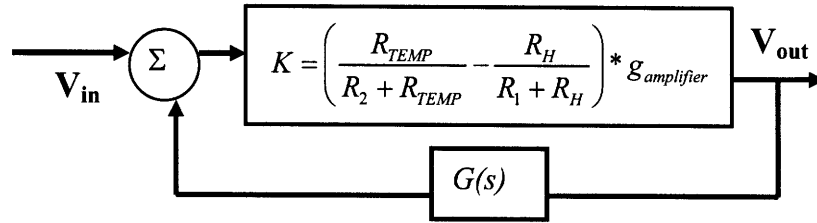
Figure 5-10: Block diagram for the temperature controller with feedback using PID compensation for stability.

The step response simulations for the feedback circuit shows slight overshoot at the beginning which is well compensated to reach the setpoint with the settling time of 2 µs, and there is no oscillation or instability.
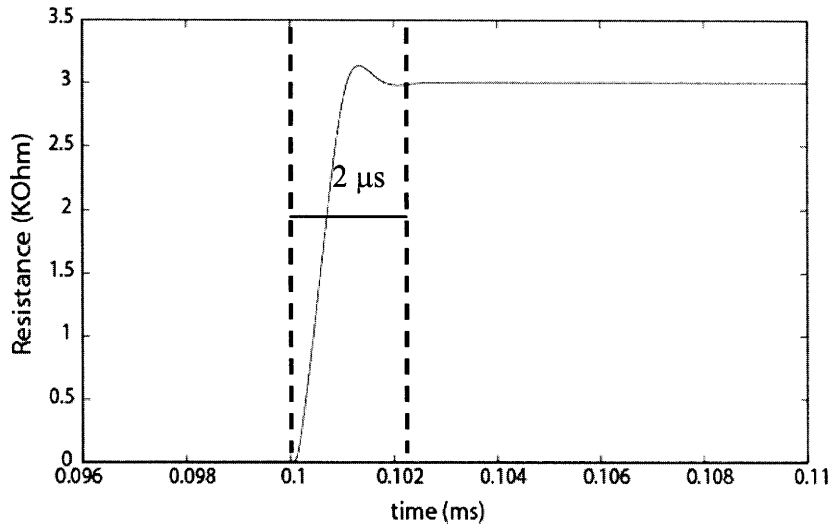
Figure 5-11: The step response for the feedback circuit.

The noise analysis for the closed loop circuit shows the noise at the output of the instrumentation amplifier to be 160 nV/√Hz which limits the measurement of the sense voltage to 5 µV. The resistance change for the heater corresponding to this sense voltage is 0.2Ω, which sets the temperature limitation for the circuit to 67 mK. This limitation is set by the noise of the instrumentation amplifier.

5.5   Stability Measurement:

The overall instability seen in the intensity at the output of the drop port of the filter is due to many contributing factors: the filter response fluctuation due to temperature instability, the laser power fluctuation, the laser wavelength instability, and the fiber coupling variation due to actual movement of the tip of the fiber. A lock-in technique is used to measure the thermal instability due to the filter response, where the other contributing factors namely the fiber coupling variation is cancelled.

The measured laser power fluctuation at a single wavelength is very small compared to the fluctuations seen with the ring resonator, and can be considered as a stable source for the experiment. The bigger problem during the experiment in the intensity fluctuation over time is the thermal drift in the piezo cube which is used for aligning the fiber tip near the waveguide. During the course of experiments, it was observed that the fiber tip had to be realigned after every set of experiments. If anything on the optical table was moved around, the fiber had to be realigned for the maximum output. Similarly, if the experiment was conducted after a period of halt (2-3 hours), the fiber had to be realigned. In one of the early experiments, the intensity of light at the drop port is seen to decrease over the time period of less than 30 minutes. To determine the temperature instability of the filter response, the coupling variation due to the thermal drift of the piezo aligner had to be removed. Thus, a two-color lock-in technique is used for the thermal stability measurement (Figure 5-12).
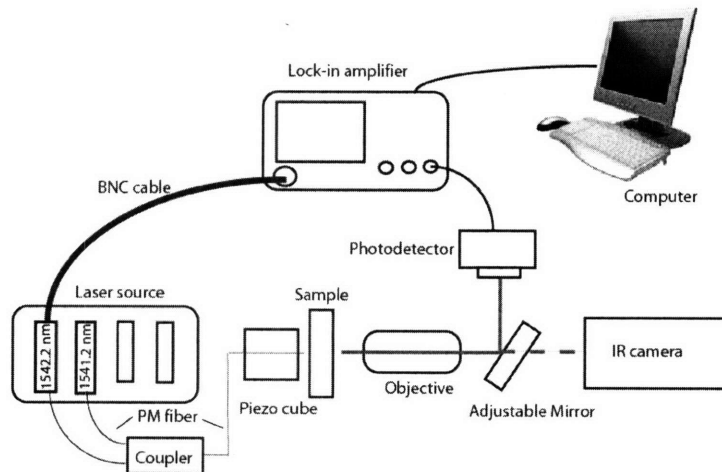
Figure 5-12: Thermal stability measurement setup.

For the experiment, the two optical signals from two laser modules (8164A and 81554SM) are coupled into the waveguide using the available 4-1 polarization maintaining coupler (Micro-Optics Inc. SN9404). One of the optical wavelengths is taken to be at the steepest slope in the pass-band of the filter and another signal is taken as the reference, away from the pass-band. Both the signals are externally modulated with two phase-locked function generators at two different frequencies (ω_1 = 5 KHz, and ω_2 = 35 KHz), and measured through a photodetector (New Focus 2011, gain = 3×10^4) and a lock-in amplifier (SR830) in the dual-harmonic mode. The lasers could not be internally modulated with the digital on-off modulation due to the presence of higher order harmonics in the signals. With the sinusoidal modulation, the 7th harmonics for 5 KHz signal was an order of magnitude lower than the second signal at 35 KHz. The variation due to the coupling misalignment is the common noise factor in both the signals measured by the lock-in amplifier, which is cancelled by subtraction and the residual deviation is due to the thermal fluctuation of the filter. To show that the measurement is not limited by the electronics of the setup, the thermal stability measurement was taken for the laser with a commercial athermal MUX-DEMUX (E-TEX). The optical output of the commercial filter (Figure 5-13 a) was passed through the 4-1 coupler, and measured with the photodetector at the gain of 3×10^4 such that the detected power was similar as for the microring resonator. The standard deviation for the drift in the wavelength was measured to be only 0.28 pm over the time range of more than an hour (Figure 5-13 b).

(a)   (b)
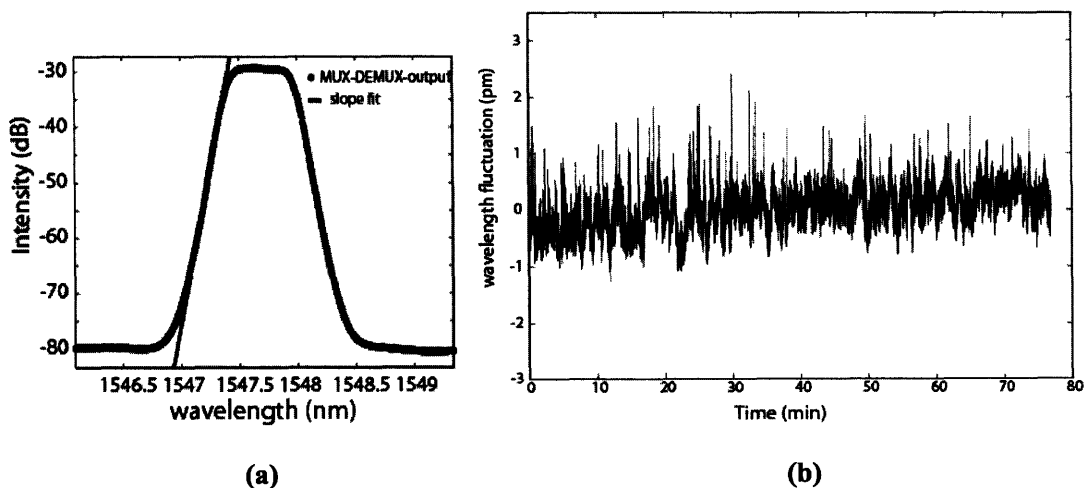
Figure 5-13: Laser output stability measurement with a commercial MUX-DEMUX.

For the SiN ring resonator, 30 pm shift in the resonant wavelength corresponds to a change in temperature of 1 K. If the rings are assumed to be in absolute athermal conditions, the wavelength drift of the laser for 0.28 pm would correspond to the temperature variation of 10 mK which is the limiting factor for the stability measurement due to the laser inaccuracy.

The thermal stability for the microring resonator was first measured with the open-loop circuit. The input voltage of 3 V was applied to the circuit. The standard deviation in the frequency due to the thermal variation was measured to be 500 MHz (~4.5 pm), which corresponds to the filter temperature fluctuation of 145 mK (Figure 5-14 a). The two optical inputs were at 1541.2 nm and 1542.2 nm. The extinction ratio for the second-order filter was only 12 dB. Thus, even the light with the wavelength of 1542.2 nm which is away from the pass-band was seen at the drop port through the photodetector. The drop port spectrum is shown in Figure 5-14 (b) with the slope estimate at the wavelength of interest (1541.2 nm – 32.28 dB/nm).
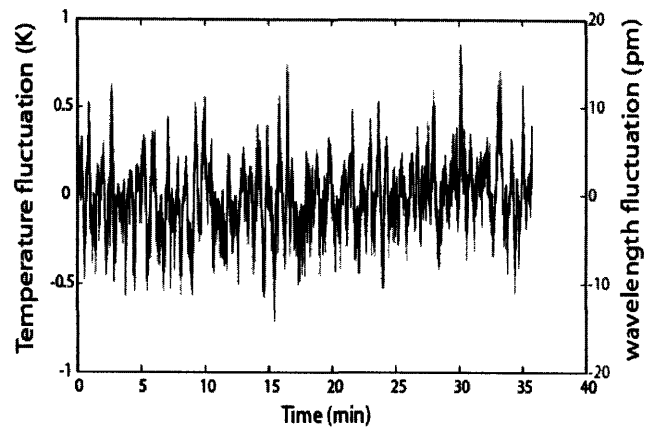
(a)
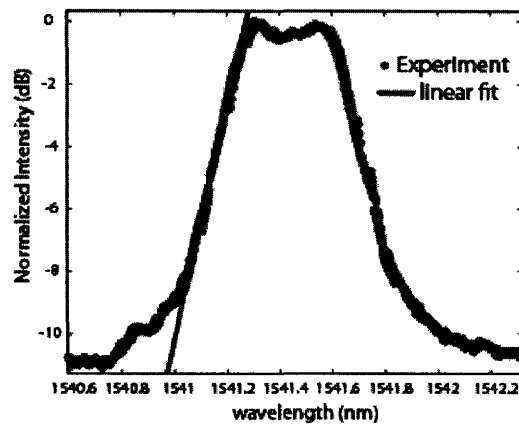
(b)

Figure 5-14: (a) Temperature fluctuation over time measured with the lock-in technique for the open loop circuit, (b) Drop port spectrum for the filter with slope fitting.

The fluctuation in the intensity of the light at the drop port of the filter was measured by the lock-in amplifier. The slope (32.28 dB/nm) along the roll-off of the pass-band gives the measure of the change in the intensity versus the change in the resonant wavelength. Thus, the temperature fluctuation of the filter can be calculated from the intensity deviation measurements. With the closed-loop feedback circuit, the temperature perturbation can be controlled with higher precision than with the open-loop circuit. Similar stability measurements show the thermal deviation of less than 100 mK for the filter response, with the best achieved value of 80 mK thermal stability, which is equivalent to the frequency variation of 280 MHz. Figure 5-15 shows the temperature fluctuation measured for the closed loop circuit.
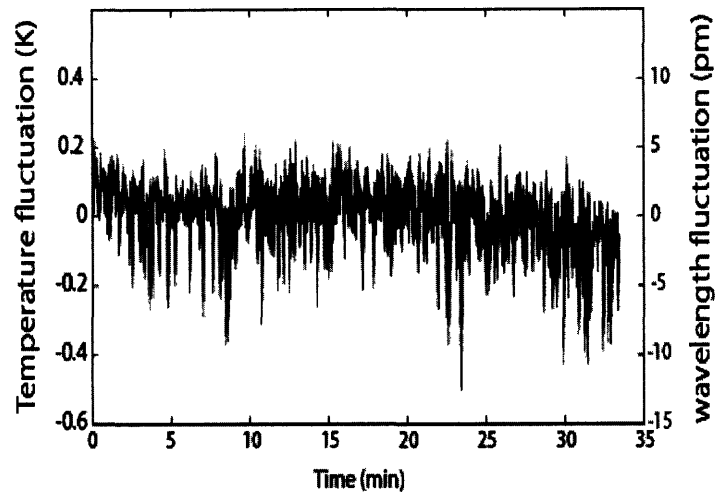
Figure 5-15: Temperature fluctuation over time measured with the lock-in technique for the closed-loop circuit (amplifier gain = 6).

Another experiment was done to show the thermal stability of the system where an external temperature perturbation is introduced by shining a white light source on to the sample. When the light is on, the temperature variation of nearly 1 K is introduced to the heater which is shown in Figure 5-15 with the open-loop measurement. With the closed-loop feedback, the temperature variation is reduced to be equivalent to the fluctuation of 80 mK. The sense voltage measured across the resistor is different when the light is turned on and off. When the light is turned on, the temperature of the heater increases, thus the voltage across the heater goes down such that there is less joule heating. With the amplifier gain of 1, the closed-loop does not perform any better than the open-loop circuit as the gain is not enough to reach the setpoint. When the proportional gain is increased to 50, the external temperature variation is compensated by the circuit.
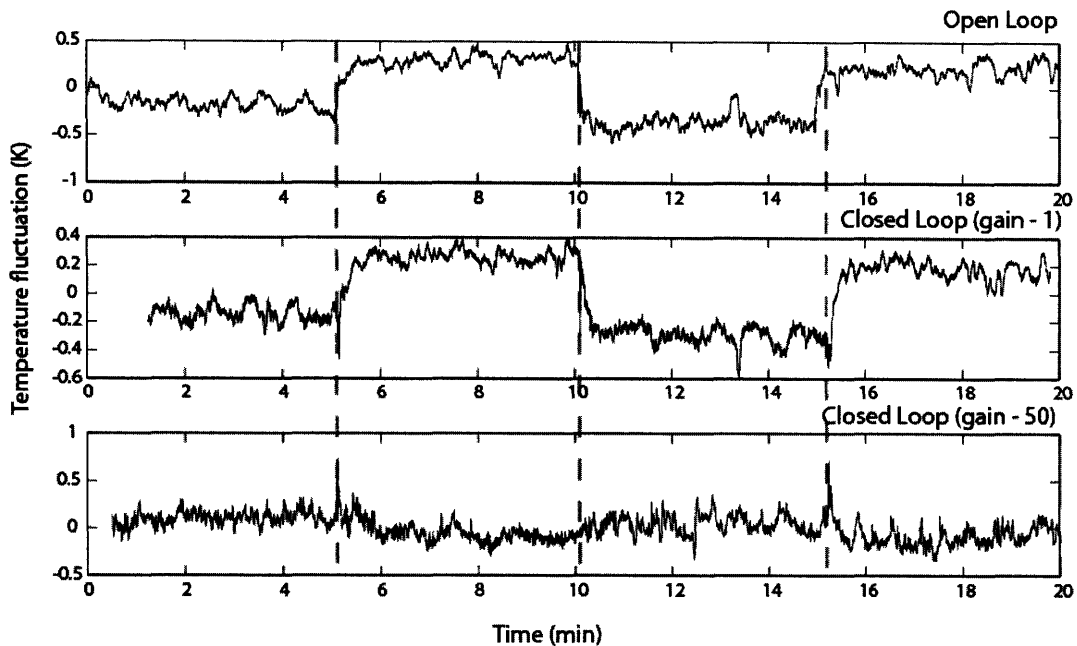
Figure 5-16: Temperature variation over time measured with the lock-in technique.

The temperature perturbation of 80 mK can be reduced by putting the device in a box or vacuum chamber such that the air convection around it is lowered. With the closed-loop feedback circuit, the external temperature perturbation can be reduced within the experimental limit set by the noise limit of the control circuit and the temperature variation due to air movement around the sample. With the various PID gain factors, we can compensate for any external temperature variation.

5.6   Summary :

Thus, with the PID temperature controller circuit, we show the stability of the microring resonator to 80 mK giving the resonant frequency stability of 280 MHz. Better temperature stability can be obtained by isolating the device in a more controlled environment such as a concealed box or in vacuum, the options which are available for packaging for an ADC.

References:

1. M. Malaeb, "Single-Chip Digitally Controlled Data Acquisition as Core of Reliable DWDM Communication Systems", Analog Dialogue 36-05 (2002).

2. "PID-1500: Thermoelectric and Resistive Heater Temperature Controller Instruction Manual", Wavelength Electronics, Inc., 2002-03.

3. B.E. Little, S. Chu, F. Johnson, V. Van, J. Hryniewicz, "A VLSI photonics platform for microwave photonic application", IEEE International Topical Meeting on Microwave Photonics, (2004).

4. P. Heimale, P. Katila, J. Aarnio, A. Heinamaki, "Thermally tunable Integrated Optical Ring Resonator with Poly-Si Thermistor", Journal of Lightwave Technology, Vol. 14, No.10, Oct, 1996.

5. S. Halas, A. Kaminski, T. Durakiewicz, "A bridge-based temperature controller with a resistor as temperature sensor and heater", Meas. Sci. Technol., Vol. 14, 1993 (1208-12).

6. V. A. Kulikov, "A Microthermostat with Combined Heater and Temperature Sensor", Instruments and Experimental Techniques, Vol.45, No.3, 2002 (416-17).

7. Z. Lu, J. Lach, M.R. Stan, K. Skadron, "Improved Thermal Management with Reliability Banking", IEEE Micro, pp. 40-49, Nov-Dec (2005).

8. K. Skadron, M.R. Stan, W. Huang, S. Velusamy, K. Sankaranarayanan, D. Tarjan, "Temperature – Aware Computer Systems: Opportunities and Challenges", IEEE Micro, pp. 52-61, Nov-Dec (2003).

9. Website: http://www.linear.com/designtools/software/

CHAPTER 6

CONCLUSION AND FUTURE WORK

6.1 Summary:

The electronic analog-to-digital converter (ADC) is facing a bottleneck in achieving a high sampling rate as well as a high effective number of bits. Various photonic devices can be used in an ADC to enhance its performance. Such a concept has been proposed for the electronic-photonic integrated circuit (EPIC) system where the signal sampling is done in the optical domain. With this system, 7 ENOBs can be obtained with 40 GSPS sampling rate. Microring resonators are used as tunable filters for wavelength division demultiplexing in this optical-electronic system. The small size of the ring (radius = 10 μm) enables a large free spectral range (1.6 THz) and also provides greater ability to integrate large number of devices in a small area chip. CMOS compatible materials are used for the optical device fabrication such that the current CMOS technologies can be utilized and both the optical and the electronic components can be fabricated in a single facility. The core of the waveguide is made of silicon-rich-silicon nitride and the over-cladding materials are silicon dioxide and HSQ. The high index contrast ratio of the materials allows the feature size of the waveguide to be in sub-micron range. The microrings are used as filters that allow signals of only specific wavelength to pass during the sampling process for an ADC.

The second-order filters are designed to get steeper drop response and to reduce the cross-talk between adjacent filters. The filter response for the resonator has the FWHM of 25 GHz and the channel spacing of 80 GHz. During the sampling process for an ADC, any error in the resonant wavelength of the filter results in the timing jitter which can produce erroneous results. Thus, the resonant wavelength of the ring filter has to be controlled within a certain value to reduce this timing jitter. Many phenomena within the device can cause the shift in the resonant wavelength, temperature change being one of them. Thermal tuning is utilized for controlling the resonant wavelength of the ring resonator. Thermal tuning is based on the thermo-optic effect of the waveguide according to which, the thermal changes in the device causes optical variations. As the

117

temperature of the ring is changed, the refractive index varies which causes shift in the resonant wavelength. Thermal tuning is mostly used for post-fabrication trimming and to compensate for any temperature variation in the environment. Si-rich-SiN rings have been tuned with the efficiency of 30 pm/K. This was experimentally verified using external heaters as described in Chapter 3. The slight discrepancy in the tuning efficiency from the theory can be explained by the temperature dependent thermo-optic coefficient of the waveguide.

The microring filters are tuned with on-chip heaters made of titanium metal. One of the system requirements for the EPIC was the total electrical power limitation for tuning the ring filter. For efficient thermal tuning, the heater designing is an important aspect. Finite element thermal simulations were used to study the temperature profile and heating of the rings with different heater designs. The final fabricated heater was able to tune the filter with the efficiency of 80 µW/GHz. According the thermal simulations, the heater design should have had the tuning efficiency of 60 µW/GHz. However, due to the fabrication misalignment of the heater, the efficiency decreased by nearly 25%. The 3-ω method and thermoreflectance were used to characterize the heaters.

Temperature stability is an important requirement for the filter in the EPIC system. An off-chip closed loop feedback circuit was designed to control the temperature of the heater within a certain fixed value. A feedback circuit was based on the Wheatstone bridge architecture. The titanium heater was the variable resistor of the bridge. The resistor at the opposite arm of the bridge to the heater is a set potentiometer. The voltage difference across the two resistors is the feedback error which is measured by a low noise instrumentation amplifier. The error passes through a PID controller and sets the voltage across the bridge. The absolute temperature of the heater can be controlled within 80 mK with an external heat source perturbing the rings. This temperature control of 80 mK assures the stability of the resonant frequency within 280 MHz, and this frequency variation can cause the timing jitter of 48 ps. The higher timing jitter will lead to lower ENOBs or lower sampling frequency. With 50 ps of jitter, the ENOBs is reduced to 6.5 as compared to 7 ENOBs. The limitation for the temperature control in the circuit, which increased the jitter, was set by the noise of the amplifier as described in Chapter 5. The total power consumed by the off-chip control circuit was 200 mW. Since the power consumption restriction was only for on-chip devices, the off-chip circuit was not included in the total power consumption for the ADC requirement. However, as one of the future directions for the research, the total

power consumption of such an ADC should be studied and possibly reduced to make it a more portable energy efficient device.

Thus, the goal of a temperature controlled microring filter for an ADC has been achieved and is described in this thesis. Some future works and reconsiderations for the research are discussed in the next section.

6.2   Future Work:

One of the key specifications that were not met during the experiments was the total power consumption for tuning the ring resonators. The rings were tuned with 80 μW/GHz power when the system requirement was 60 μW/GHz. As described in Chapter 4, the main reason for this discrepancy was the misalignment of the heater. When designing the heater for thermal tuning, the fabrication tolerance was not considered. The smallest feature size for the heater was 800 nm and in theory, the heaters were perfectly aligned on top of the rings. Due to misalignment during heater fabrication the tuning efficiency was decreased by nearly 25%. As a part of the development of the research, the heater design should be reconsidered to resist such fabrication mishaps. Increasing the width of the heater such that there is a larger overlap of the heater with the ring filter would give more tolerance to the heater design against fabrication misalignments. However, the width cannot be too big as the problems of cross-talk and higher power dissipation becomes prominent. The power dissipation for tuning can be reduced by exploring different waveguide materials as discussed later in the chapter. In future, the heater fabrication should be done more carefully with better alignment markers to make sure that the overlap between heater and ring is well matched.

Similarly, a single heater was fabricated on top of a second-order ring filter. Two rings of the filter could not be controlled independently. In the case of frequency mismatch between two rings, they have to be heated independently. The heater design has to be modified to ensure independent heating such that the frequency mismatch can be corrected. In Chapter 4, individual circular heaters on top of each ring were also considered which could have been controlled independently. Figure 6-1 shows such a heater which was used mostly to compensate for the frequency mismatch between the rings. The critical dimension of the heater was 1.2 μm as compared to 800 nm for the optimized heater described in Chapter 4, which made the overlap of

the heater on top of ring relatively easier. But this design is not very power efficient as it takes high power to tune a single filter.
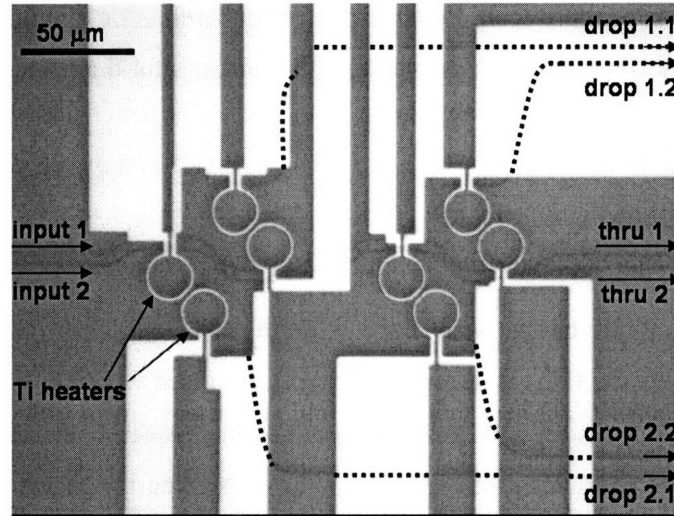
Figure 6-1: Separate heaters for two rings of a second-order filter.

A single heater, similar to the final design discussed in Chapter 4, on top of the second-order filter with an option of three contacts could give the alternative of heating a single ring or both the rings at any given time with a single temperature control circuit. One of the other problem of having two heaters for a single filter apart from large power consumption is the requirement of two control circuits which will increase the off-chip power dissipation. Even though, off-chip power dissipation is not currently restricted for the EPIC system, it is not hard to see that the power requirement for a portable ADC will be limited, which will limit both the on-chip and off-chip power consumption. As a part of the future research direction, the total power consumption of the entire ADC has to be constricted within certain limit.

The temperature control of the heater was limited to more than 60 mK due to the circuit noise which prevented the device from reaching the system specification of 30 mK. The noise of the operational amplifier was the limiting factor. A better circuit design with lower noise figure should be considered to lower the temperature measurement limit. Most of the noise in the circuit was from the amplifiers. There could be a creative way to imply the PID functions without using amplifiers or by reducing the number of amplifiers used in the present circuit. Also, the instrumentation amplifier measures the voltage difference across the heater and the set resistor to indicate any temperature change. Higher voltage difference will ensure better signal to noise

ratio. The heater material with a higher temperature coefficient can give a large resistance change and voltage difference. Titanium was chosen for this work due to fabrication ease. However, other metals with larger temperature coefficient such as platinum can be considered that will give better signal to noise ration and reduce the temperature measuring limit of the circuit. Metals such as nickel, titanium, cobalt, tungsten, aluminum etc. are CMOS compatible which can be used in the silicide form. They may have positive or negative temperature coefficient. Tungsten silicide has a negative temperature coefficient of 400 ppm/°C. Different metal compounds that are compatible with CMOS processing can also be tested to use as the heater. Their temperature coefficients have to be experimentally verified to be large enough before using them.

Using silicon waveguides instead of Si-rich-SiN would make the thermal tuning of the ring resonators very power efficient. Silicon's thermo-optic coefficient is an order of magnitude larger than that of SiN. Thus, a small change in temperature would cause larger variation in the resonant frequency. For SiN, 1 K change in temperature gives only 3.55 GHz shift in resonant frequency, where as for Si rings, the same temperature change will cause a shift of 13 GHz. Thus, the same heater design used for SiN rings can be more than 3 times power efficient when used for heating the silicon rings. Using silicon rings will definitely reduce the tuning power consumption. However, the downside is the stringency in the temperature control. Since the thermo-optic coefficient of silicon is large compared to SiN, a slight perturbation in temperature of the ring could cause the resonant frequency to shift by a large amount. Thus, the temperature control for the heater will be reduced to less than 10 mK, which is very hard to achieve. Thus, moving completely to the silicon platform would benefit in terms of controlling the total power dissipation of the system, however, temperature control becomes a bigger issue which has to be addressed carefully. One of the ways to reduce the temperature control requirement for silicon is by adding a polymer with negative thermo-optic coefficient as the cladding material for the silicon waveguide. The effective index of the guided mode in the waveguide can be made temperature insensitive by choosing the cladding material such that the positive variation in the index due to temperature change at the core is cancelled by the negative variation in the index at the cladding. As seen in Chapter 3, the thermo-optic coefficient of both the cladding and the core is required to calculate the dependence of the resonant wavelength to the temperature variation.

APPENDIX A:

SPICE NET File

```
%% SPICE file to simulate the control circuit %%

XU1 N006 N009 N010 N012 0 N007 N002 N003 LT1167
V1 N002 0 15
V2 N012 0 -15
V3 N013 0 PWL(0 0 0.1 0 0.1001 3 0.2 3) AC 1
R2 N001 N009 10
R3 N001 N010 10
R4 N010 0 3k
XU2 0 N004 N002 N012 N005 LTC1052
XU3 N014 N011 N002 N012 N001 LTC1052
R5 N004 P001 1k
R6 N008 N004 1k
R7 N011 N005 10k
R8 N001 N011 10k
R9 N014 N013 10k
R10 0 N014 10k
C1 N004 N007 5p
C2 N005 N008 10n
R12 N006 N003 100k
C3 N007 P001 10n
R1 N005 N004 10k
R11 N004 N007 2k
;dc V3 0 5 1
;tran 0 0.4 0 0.0001
XVH N009 0 N010 0 RES
.SUBCKT RES 1 2 4 5
ERES 1 3 Value = {I(Vsense)*(2.4k*(1+0.0012*((V(4,5))^2/2.4k)*8800))}
Vsense 3 2 DC 0

*XVH N009 0 RES
*.SUBCKT RES 1 2
*ERES 1 3 Value = {I(Vsense)*2.5k*(1+0.0012*(I(Vsense))^2*2.5k*8800)}
*Vsense 3 2 DC 0
.Ends
;ac dec 100 1 100MEG
.noise V(N007) V2 dec 100 1 10MEG
;tf V(N005) V3
.lib LTC.lib
.backanno
.end

*              RG1 IN- IN+ V- REF OUT V+ RG2
.SUBCKT LT1167  1   2   3  4  5   6   7  8
*
XIN1 2 1 7 4 10 LT1167_IN1
XIN2 3 8 7 4 11 LT1167_IN2
XOUT 13 12 7 4 6 LT1167_OUT
* input protection
DIP1 2 7 DX
DIP2 3 7 DX
DIP3 4 2 DX
DIP4 4 3 DX
* input capacity
CDIFF 2 3 1.6E-12
CCM1 2 4 1.6E-12
CCM2 3 4 1.6E-12
* feedback network
RF1 1 10 24700
CF1 1 10 2.5E-12
RF2 8 11 24700
```

```
CF2 8 11 2.5E-12
RCM1 10 12 10E3
RCM2 6 12 10E3
RCM3 11 13 10E3
RCM4 13 5 10E3
.MODEL DX D(IS=8.2592e-16 RS=0 XTI=0)
.ENDS LT1167
*
***
*
.SUBCKT LT1167_IN1 1 2 3 4 5
*
* input stage
M1 11 2 10 10 M1 L=100U W=100U
M2 12 1 10 10 M2 L=100U W=100U
RD1 3 11 12575 TC=-2.97e-6
RD2 3 12 12575 TC=2.97e-6
DI1 1 3 DI1
DI2 2 3 DI2
C1 11 12 1.0547e-13
IEE 10 4 DC 0.00015904
GA 60 99 11 12 7.952e-5
*
* noise sources
IR1 0 101 DC 1
IR2 0 102 DC 1
DR1 101 0 DRI
DR2 102 0 DRI
GRI1 99 1 101 102 0.002898
IR3 0 103 DC 1
IR4 0 104 DC 1
DR3 103 0 DRI
DR4 104 0 DRI
GRI2 99 2 103 104 0.002898
RRu 605 0 3.4435
VRu 605 0 DC 0
FRu 99 60 VRu 1
*
* frequency shaper
RR1 6 60 0.001
*
* output stage
R2 6 99 1000
C2 6 7 1.25e-10
GB 7 99 6 99 3560.5
R01 7 99 14.9
R02 7 50 0.1
R03 50 5 65
R04 5 99 5937900000
VC 53 50 DC 1.2
VE 54 50 DC -1.2
DC1 53 55 DX
DC2 55 56 DX
DE1 57 54 DX
DE2 58 57 DX
GVC1 3 56 3 56 1.0E-4
GVE1 4 58 4 58 1.0E-4
GVC2 3 55 3 55 1.0E-5
GVE2 4 57 4 57 1.0E-5
GVLP 99 60 56 3 1
GVLN 99 60 58 4 1
*
* supply characteristic
EGND 99 0 POLY(2) 3 0 4 0 0 0.5 0.5
IP 3 4 DC 0.00014096
*
.MODEL DX D(IS=8.2592e-16 RS=0 XTI=0)
.MODEL M1 NMOS(LEVEL=3 KP=0.56117 VTO=1.00001 KF=7.6298e-28)
.MODEL M2 NMOS(LEVEL=3 KP=0.56117 VTO=0.99999 KF=7.6298e-28)
.MODEL DI1 D(IS=9.55e-11 EG=0.21274 XTI=3)
.MODEL DI2 D(IS=9.45e-11 EG=0.2144 XTI=3)
```

```
.MODEL DRI D(IS=8.2592e-16 KF=6.4148e-18 RS=0 XTI=0)
.ENDS LT1167_IN1
*
***
*
.SUBCKT LT1167_IN2 1 2 3 4 5
*
* input stage
M1 11 2 10 10 M1 L=100U W=100U
M2 12 1 10 10 M2 L=100U W=100U
RD1 3 11 12576 TC=-2.9701e-6
RD2 3 12 12576 TC=2.9701e-6
DI1 1 3 DI1
DI2 2 3 DI2
C1 11 12 1.0547e-13
IEE 10 4 DC 0.00015904
GA 60 99 11 12 7.952e-5
*
* noise sources
IR1 0 101 DC 1
IR2 0 102 DC 1
DR1 101 0 DRI
DR2 102 0 DRI
GRI1 99 1 101 102 0.002898
IR3 0 103 DC 1
IR4 0 104 DC 1
DR3 103 0 DRI
DR4 104 0 DRI
GRI2 99 2 103 104 0.002898
RRu 605 0 3.4435
VRu 605 0 DC 0
FRu 99 60 VRu 1
*
* frequency shaper
RR1 6 60 0.001
*
* output stage
R2 6 99 1000
C2 6 7 1.25e-10
GB 7 99 6 99 3560.5
RO1 7 99 14.9
RO2 7 50 0.1
RO3 50 5 65
RO4 5 99 5937900000
VC 53 50 DC 1.2
VE 54 50 DC -1.2
DC1 53 55 DX
DC2 55 56 DX
DE1 57 54 DX
DE2 58 57 DX
GVC1 3 56 3 56 1.0E-4
GVE1 4 58 4 58 1.0E-4
GVC2 3 55 3 55 1.0E-5
GVE2 4 57 4 57 1.0E-5
GVLP 99 60 56 3 1
GVLN 99 60 58 4 1
*
* supply characteristic
EGND 99 0 POLY(2) 3 0 4 0 0 0.5 0.5
IP 3 4 DC 0.00014096
*
.MODEL DX D(IS=8.2592e-16 RS=0 XTI=0)
.MODEL M1 NMOS(LEVEL=3 KP=0.56117 VTO=1.00001 KF=7.6298e-28)
.MODEL M2 NMOS(LEVEL=3 KP=0.56117 VTO=0.99999 KF=7.6298e-28)
.MODEL DI1 D(IS=6.5805e-12 EG=0.7051 XTI=3)
.MODEL DI2 D(IS=5.3995e-12 EG=0.7452 XTI=3)
.MODEL DRI D(IS=8.2592e-16 KF=6.4148e-18 RS=0 XTI=0)
.ENDS LT1167_IN2
*
***
*
```

```
.SUBCKT LT1167_OUT 1 2 3 4 5
*
* input stage
M1 11 2 10 10 M1 L=100U W=100U
M2 12 111 10 10 M2 L=100U W=100U
RD1 3 11 12576 TC=-2.9703e-6
RD2 3 12 12576 TC=2.9703e-6
DI1 111 3 DI1
DI2 2 3 DI2
C1 11 12 1.0546e-13
IEE 10 4 DC 0.00015903
GA 60 99 11 12 7.9514e-5
*
* noise sources
IR1 0 101 DC 1
IR2 0 102 DC 1
DR1 101 0 DRI
DR2 102 0 DRI
GRI1 99 1 101 102 0.002898
IR3 0 103 DC 1
IR4 0 104 DC 1
DR3 103 0 DRI
DR4 104 0 DRI
GRI2 99 2 103 104 0.002898
RRu 605 0 3.4435
VRu 605 0 DC 0
FRu 99 60 VRu 1
*
* common mode rejection
GCM1 99 20 POLY(2) 1 99 2 99 0 0.0005 0.0005
RCM1 21 99 1000
RCM2 20 99 1000000
LCM 20 21 0.53052
*
*140 dB for gain=1000
*ECM 111 1 20 99 0.8E-7
*
* 125 dB for gain=100
ECM 111 1 20 99 5.6234e-7
*
*115 dB for gain=10
*ECM 111 1 20 99 1.778E-6
*
* frequency shaper
RR1 6 60 0.001
*
* output stage
R2 6 99 1000
C2 6 7 1.25e-10
GB 7 99 6 99 3560.5
R01 7 99 14.9
R02 7 50 0.1
R03 50 5 65
R04 5 99 5937900000
VC 53 50 DC 1.9
VE 54 50 DC -1.6
DC1 53 55 DX
DC2 55 56 DX
DE1 57 54 DX
DE2 58 57 DX
GVC1 3 56 3 56 1.0E-4
GVE1 4 58 4 58 1.0E-4
GVC2 3 55 3 55 1.0E-5
GVE2 4 57 4 57 1.0E-5
GVLP 99 60 56 3 1
GVLN 99 60 58 4 1
ECLP 91 0 7 50 370.37
ECLN 92 0 7 50 370.37
DCLP 91 90 DX
DCLN 90 92 DX
VLIM 90 0 DC 0
```

```
FB 7 99 VLIM 10.851
*
* supply characteristic
EGND 99 0 POLY(2) 3 0 4 0 0 0.5 0.5
DSUB 4 3 DX
IP 3 4 DC 0.00014097
*
GV 31 0 7 50 10
DP1 3 31 DX
DP2 33 4 DX
RGV 32 33 9.7531
EGV 31 32 POLY(1) 3 4 -0.8 1.0
*
.MODEL DX D(IS=8.2592e-16 RS=0 XTI=0)
.MODEL M1 NMOS(LEVEL=3 KP=0.56121 VTO=1.00001 KF=7.6303e-28)
.MODEL M2 NMOS(LEVEL=3 KP=0.56121 VTO=0.99999 KF=7.6303e-28)
.MODEL DI1 D(IS=9.55e-11 EG=0.20727 XTI=3)
.MODEL DI2 D(IS=9.45e-11 EG=0.20883 XTI=3)
.MODEL DRI D(IS=8.2592e-16 KF=6.4148e-18 RS=0 XTI=0)
.ENDS LT1167_OUT
*
*
.SUBCKT LTC1052 3 2 7 4 6 ;(+IN -IN V+ V- OUT)
* INPUT
IB1 2 7 -10P
IB2 3 7 10P
RD1 4 80 4421
RD2 4 90 4421
M1 80 2 12 12 PM1
M2 90 3 12 12 PM2
CIN 2 3 5e-12
DG1 2 7 DMG1
DG2 3 7 DMG2
C1 80 90 1.5e-11
ISS 7 12 0.00012
CS 12 0 7.5e-12
* INTERMEDIATE
GCM 0 8 12 0 2.2619E-11
GA 8 0 80 90 2.2619E-04
R2 8 0 100000
C2 1 8 3e-11
GB 1 0 8 0 7025.3
RO2 1 0 199
* OUTPUT
RSO 1 6 1
ECL 18 0 1 6 179.55
GCL 0 8 20 0 1
RCL 20 0 10
D1 18 19 DM1
VOD1 19 20 0
D2 20 21 DM1
VOD2 21 18 1.7955
*
D3A 131 70 DM3
D3B 13 131 DM3
GPL 0 8 70 7 1
VC 13 6 1.4332
RPLA 7 70 10
RPLB 7 131 1000
D4A 60 141 DM3
D4B 141 14 DM3
GNL 0 8 60 4 1
VE 6 14 1.4332
RNLA 60 4 10
RNLB 141 4 1000
*
IP 7 4 0.00158
DSUB 4 7 DM2
* MODELS
.MODEL PM1 PMOS(KP=4.2637E-04 VTO=-1.1)
.MODEL PM2 PMOS(KP=4.2637E-04 VTO=-1.1000005)
```

```
.MODEL DM1 D(IS=1e-20)
.MODEL DM2 D(IS=8e-16 BV=19.8)
.MODEL DM3 D(IS=1e-16)
.MODEL DMG1 D(IS=7E-12 N=2.31)
.MODEL DMG2 D(IS=6.3E-12 N=2.31)
.ENDS LTC1052
```

APPENDIX B:

MATLAB CODE

B.1   Design curves for different cladding

```
%%%%%% Computation for TE mode, buried guide %%%%%%
%%%%%% varying thermo-optic coeff (dclad/dT) for cladding %%%%%%

c = 3e17;                   %[nm/s] speed of light
lambda0 = 1550;             %[nm] operating wavelength for the system
w0 = c/lambda0*(1/1e9);     %[GHz] frequency corresponding to operating wavelength

%%% input power and overall avg. temperature change of waveguide: values from femlab

%%% thermal impedance for the final heater ~ 5200K/W
P = 0.0012;                 %[W] input power to the heater
T = 6.24;                   %[K] overall change in temp of the guide due to heater

ng = 2.293;                 %group refractive index

W0 = 2;                     %[GHz]repetition rate for mode locked laser
T0 = 1/(W0*1e-6);           %[fs]period for mode locked laser
width = 20;                 %[nm]pulse width for laser output
chirp = T0/width;           %[fs/nm] chirp due to dispersion

dndc = 0.87;                %change in effective refractive index wrt change in refractive
index of core
                            %dneff/dncore
dcdT = 4.5e-5;              %change in refractive index of core wrt temp
                            %dncore/dT  ---- core: Si-rich SiN
dndclad = 0.25;            %change in effective refractive index wrt change in refractive
                             index of clad
                            %dneff/dnclad
dwdc = 69.7/0.001;          %frequency dependence on index change
dwduc = 18.7/0.001;
dwdlc = 9.2/0.001;

i = 0;

for dcladdT = -1e-4:(2e-4+1e-4)/1000:3e-5
%[1/K]change in refractive index of clad wrt temp
    i = i + 1;
    x(i) = dcladdT;
    dlabmdadT(i) = - (lambda0/ng)*(dndc*dcdT + x(i)*dndclad);
%[nm/K]change in lambda wrt change in temp
    jitter1(i) = abs(chirp*dlabmdadT(i)/10);
%[fs]total jitter for 100mK temp change
    jitter2(i) = abs(chirp*dlabmdadT(i)/20);
%[fs]total jitter for 50mK temp change
    jitter3(i) = abs(chirp*dlabmdadT(i)*30e-3);
%[fs]total jitter for 50mK temp change
    dwdT1(i) = - (w0/ng)*(dndc*dcdT + dndclad*x(i));
%[GHz/K]change in w wrt change in temp
    dwdT(i) = dwdc*dcdT+dwdlc*dcladdT+dwduc*dcladdT;
    dPdw(i) = abs((P/T)*1e6/dwdT1(i));

end

[AX,H1,H2] = plotyy(x,dPdw,x,jitter3,'plot');
set(get(AX(1),'Ylabel'),'String','Power Dissipation [uW/GHz]')
set(get(AX(2),'Ylabel'),'String','Timing Jitter [fs]')
xlabel('dnclad/dT [1/K]')
title ('TE mode, buried guide')
```

```
%Harry's double axis plot code in my folder under matlab utils
plot(x,dPdw)
addaxis(x,jitter2,[0 44])
addaxisplot(x,jitter3,2)
```

B.2   Transmission curve for second-order filter

```
lambda = (1531.66e-9:(1532.46e-9-1531.66e-9)/500000:1532.46e-9);
neff = 1.460;            % effective index of the ring
c = 3e8;                 % speed of light
L = 2*pi*10e-6;          % circumference of the ring
w = (2*pi*c)./lambda;    % circular frequency
Tr = L*neff/c;           % round trip signal time


a_straight = 3;          %[dB/cm] total absorption loss at waveguide section
alpha = ((a_straight)/(-3/(log(0.5))))*100);   %[1/m] static absorption coefficient (SiN)


%%%% For Silicon Nitride (SiN) waveguide


uo = 4*pi*1e-7;          %[H/m]
e0 = 8.85e-12;           %[F/m]


t = 500e-9;              % distance between bus and ring
t1 = 900e-9;             % distance between rings


wb = 600e-9/2;           %[m] width of bus waveguide/2
wr = 800e-9/2;           %[m] width of ring waveguide/2


so = t+wr+wb;            %[m] distance between bus and ring from the center
so1 = t1+wr+wr;          %[m] distance between two rings from the center


ncore = 2.2;             % SiN refractive index
nclad = 1.44;            % SiO2 refractive index
neff = 1.46;             % effective index of SiN/SiO2 waveguide
l = 1535e-9;             % wavelength of interest for transfer function
w1 = c/l;
ko = 2*pi/l;             % wave vector
B1 = ko*neff;            % propagation constant in the waveguide
B2 = B1;                 % both ring and bus made of same core/cladding


%%%% Bus
a1 = sqrt(B1^2-ko^2*nclad^2);      % decay constant in cladding
Pb = (B1/(2*w1*uo))*(wb+1/a1);     % mode power
k1 = sqrt(ko^2*ncore^2-B1^2);      % transverse propagation constant in core


%%%% Ring1
a2 = sqrt(B2^2-ko^2*nclad^2);      % decay constant in cladding
Pr = (B2/(2*w1*uo))*(wr+1/a2);     % mode power
k2 = sqrt(ko^2*ncore^2-B2^2);      % transverse propagation constant in core


R = 1;                             % effective radius of curvature of the ring (bus
radius ~ inf.)

x = ((w1*(cos(k2*wr))*e0*(ncore^2-nclad^2))/((sqrt(Pb*Pr))*(k1^2+a2^2)*2));
y = ((sqrt((pi*R)/a2))*(exp(a2*(wr-so))));
z = (a2*(cos(k1*wb))*(sinh(a2*wb))+k1*(sin(k1*wb))*(cosh(a2*wb)));
ka = 0.087;

%%%% Ring2
a3 = sqrt(B2^2-ko^2*nclad^2);      % decay constant in cladding
Pr = (B2/(2*w1*uo))*(wr+1/a3);     % mode power
k3 = sqrt(ko^2*ncore^2-B2^2);      % transverse propagation constant in core


R1 = 10e-6;                        % radius of the ring
R2 = 10e-6;
R = (R1*R2)/(R1+R2);               % effective radius of curvature of the ring
```

```
x1 = ((w1*(cos(k3*wr))*e0*(ncore^2-nclad^2))/((sqrt(Pr*Pr))*(k2^2+a3^2)*2));
y1 = ((sqrt((pi*R)/a3)*(exp(a3*(wr-sol))))));
z1 = ((a3*cos(k2*wr)*(sinh(a3*wr))+k2*sin(k2*wr)*cosh(a3*wr)));
kb = 0.7;

ta = (1-ka^2)^(0.5);% transmission coefficient (bus-ring)
tb = (1-kb^2)^(0.5);% transmission coefficient (ring-ring)

Ta = ka^2+ta^2;
Tb = kb^2+tb^2;

A = exp(j*w.*Tr-((alpha*L)/2));
Aa = exp(alpha*L);
Aq = exp(2*j*w.*Tr-alpha*L);

T = (abs(((1+Aq).*ta-A.*tb*(ka^2+ta^2*2))./(Aq.*ta^2-2*A.*ta*tb+1))).^2;
T1 = log10(T)*10;

D = (abs((j*A.*ka^2*kb)./(Aq.*ta^2-2*A.*ta*tb+1))).^2;
D1 = log10(D).*10;

plot(lambda*1e9,D1,'r')
plot(lambda*1e9+0.1,D1,'r')
xlabel ('wavelength (nm)')
ylabel ('power (dB)')
```

B.3   3-ω method (diffused silicon resistor)

```
% three omega measurements on 6.152J boron-doped resistor
alpha = 0.0018;   % Boron doped tempco, 410.43 ohm resistor

% vs. frequency, at ~ 27.43 mA amplitude bias
% 22.51 Vpk-pk across DUT, last stage gain of 10
% [frequency, V_3w(mV - rms), V_3w(mV - rms) ]
data_f = [      1       21.65       22.07
                3       21.64       22.06
                7       20.82       21.24
               10       20.45       20.83
               26       19.40       19.80
               57       18.27       18.68
               63       18.07       18.48
               81       17.54       17.95
               98       17.07       17.63
              107       16.80       17.28
              172       15.71       16.25
              301       14.73       14.73
              420       14.09       14.19
              613       13.21       13.25
              827       12.94       12.94
              915       12.32       12.38
             1172       12.03       11.78
             1610       11.12       11.23
             1981        9.85       10.36 ];
x = size(data_f);

freq = data_f(:,1);
V_3w = (data_f(:,2)+ data_f(:,3))./2;
V_3w_error = abs(V_3w - data_f(:,2));

V_3w_f = V_3w*sqrt(2)*2/10*1e-3;               %[V] pk-pk voltage at input of final stage
V_3w_f_error = ((V_3w_error./V_3w)).*V_3w_f;
V_3w_f_e = (V_3w_f_error./V_3w_f)*100;         % temp error percentage
V_3w_e_avg = sum(V_3w_f_e)/x(:,1);

V_1w_f = 22.51;                                %[V] pk-pk voltage at input of final stage

temp_f = V_3w_f./V_1w_f/alpha*4;
temp_error = ((V_3w_f_error./V_3w)).*temp_f;
T_e = (temp_error./temp_f)*100;                % temp error percentage
T_e_avg = sum(T_e)/x(:,1);
```

131

```
figure
h1 = errorbar(log10(freq),temp_f,temp_error);
set(h1,'LineWidth',2);
set(gca,'FontSize',14);
hold on;
h1 = plot(log10(freq),temp_f,'ko');
title('change in temp of diffused resistor (6.152J) measured by 3w method');
xlabel('log (freq) - operating frequency');
ylabel('change in temp [K]');

% vs. current, at 10 Hz;
% [Vin[mV]  V_3w(rms)[mV]  V_1w(pp)[V]], last stage gain of 10,
 data_c=[400   0.246  2.132
         500   0.398  2.618
         600   0.604  3.146
         700   0.798  3.665
         800   1.196  4.16
         900   1.594  4.63
         1000  2.14   5.40
         1200  3.3    6.35
         1600  7.1    8.35
         1800  9.7    9.37
         1900  11.2   9.88
         2000  12.9   10.39];

V_3w_c = data_c(:,2)*sqrt(2)*2/10*1e-3;  % 3w pp voltage at input of final stage
V_1w_c = data_c(:,3);                     % 1w pp voltage across sample
R_DUT = 410.43;
I = (data_c(:,1)*1e-3/100)/2;             % amplitude of current [A]
P_heat = I.^2*R_DUT;                      % amplitude of peak heating [W]
temp_c = V_3w_c./V_1w_c/alpha*4;          % pk-pk temperature change [K]
temp = temp_c*1000;                       % pk-pk temperature change [mK]
I = I*1000;                               % amplitude of current [mA]

temp_c/2*1000;

figure
h1 = plot(P_heat*1000,temp_c/2,'k.');
xlabel('total power for heating the resistor [mW]');
ylabel('(amplitude) change in temp. [K]');
set(h1,'LineWidth',2);
set(gca,'FontSize',14);

% thermal conductivity calculation from freq data
l=560e-4;                                 % approximate length of resistor (40 microns wide)
RMS_power=0.01*0.01*410.43/2;
f_lin=log(data_f((end-4):end,1));
temp_lin=temp_f((end-4):end);
p=polyfit(-temp_lin,f_lin,1);
kappa=RMS_power/l/pi*p(1) % from Cahill
```